SANDIA REPORT
SAND2015-2095
Unlimited Release
Printed March 2015

Experimental Evaluation of the Free Piston Engine – Linear Alternator (FPLA)

Terry A. Johnson and Michael T. Leick
Energy Innovation Department 8366

Ronald W. Moses
Contractor

Prepared by
Sandia National Laboratories
Albuquerque, New Mexico 87185 and Livermore, California 94550

Sandia National Laboratories is a multi-program laboratory managed and operated by Sandia Corporation, a wholly owned subsidiary of Lockheed Martin Corporation, for the U.S. Department of Energy's National Nuclear Security Administration under contract DE-AC04-94AL85000.

Sandia National Laboratories

Issued by Sandia National Laboratories, operated for the United States Department of Energy by Sandia Corporation.

Available to DOE and DOE contractors from
U.S. Department of Energy
Office of Scientific and Technical Information
P.O. Box 62
Oak Ridge, TN 37831

Telephone:	(865) 576-8401
Facsimile:	(865) 576-5728
E-Mail:	reports@adonis.osti.gov
Online ordering:	http://www.osti.gov/bridge

Available to the public from
U.S. Department of Commerce
National Technical Information Service
5285 Port Royal Rd.
Springfield, VA 22161

Telephone:	(800) 553-6847
Facsimile:	(703) 605-6900
E-Mail:	orders@ntis.fedworld.gov
Online order:	http://www.ntis.gov/help/ordermethods.asp?loc=7-4-0#online

SAND2015-2095
Unlimited Release
Printed March 2015

Experimental Evaluation of the Free Piston Engine – Linear Alternator (FPLA)

T. A. Johnson and M. T. Leick
Energy Innovation
Sandia National Laboratories
P.O. Box 969
Livermore, California 94550

R. W. Moses
Contractor

Abstract

This report describes the experimental evaluation of a prototype free piston engine – linear alternator (FPLA) system developed at Sandia National Laboratories. The opposed piston design wa developed to investigate its potential for use in hybrid electric vehicles (HEVs). The system is mechanically simple with two-stroke uniflow scavenging for gas exchange and timed port fuel injection for fuel delivery, i.e. no complex valving. Electrical power is extracted from piston motion through linear alternators which also provide a means for passive piston synchronization through electromagnetic coupling. In an HEV application, this electrical power would be used to charge the batteries.

The engine-alternator system was designed, assembled and operated over a 2-year period at Sandia National Laboratories in Livermore, CA. This report primarily contains a description of the as-built system, modifications to the system to enable better performance, and experimental results from start-up, motoring, and hydrogen combustion tests.

ACKNOWLEDGMENTS

The authors wish to acknowledge Peter Van Blarigan for more than a decade of work leading the development of the free piston engine at Sandia National Laboratories. Peter worked with several collaborators over the years to develop the prototype concept. Nick Paradiso helped design and run the rapid compression-expansion machine experiments. Scott Goldsborough helped develop the design through system level modeling as well as detailed CFD modeling of the scavenging system. Hans Aichlmayr helped model and experimentally characterize the linear alternator. Jerry Fuschetto performed Flux-2D analysis of the linear alternator, developed a dynamic model of the FPLA, and helped assemble the prototype system. Yon Perras, under Peter's direction, performed the bulk of the FPLA mechanical design and assembly.

The authors also wish to thank several colleagues who contributed directly to the experiments described in this report. Gary Hubbard developed the control software and graphical user interface used to operate the prototype system. Kent Smith helped with several of the component redesigns including the pistons and bounce chamber heads. Radislov Bozinoski performed compressible flow calculations to help redesign the bounce chamber vent manifolds.

CONTENTS

FIGURES

TABLES

NOMENCLATURE

DOE	Department of Energy
SNL	Sandia National Laboratories
HCCI	homogeneous charge compression ignition
FPLA	free piston linear alternator
TDC	top dead center
BDC	bottom dead center
CFD	computational fluid dynamics
ID	inner diameter
OD	outer diameter
PRV	pressure relief valve
MAWP	maximum allowable working pressure
LVDT	linear variable differential transformer
PID	proportional, integral, derivative
DAQ	data acquisition
ES&H	environment safety and health

EXECUTUVE SUMMARY

This report describes the experimental evaluation of a prototype free piston engine – linear alternator (FPLA) system developed at Sandia National Laboratories. The opposed piston design, shown in Figure 1, was developed to investigate its potential for use in hybrid electric vehicles (HEVs). The twin, dual-ended pistons are driven from a central combustion chamber while bounce chambers are used as a means of energy storage to provide compression work for the next cycle. The opposed piston configuration eliminates the problem of momentum balance and vibration that a single piston design would cause in a vehicle application. The system is mechanically simple with two-stroke uniflow scavenging for gas exchange and timed port fuel injection for fuel delivery, i.e. no complex valving. Electrical power is extracted from piston motion through linear alternators which also provide a means for passive piston synchronization through electromagnetic coupling. In an HEV application, this electrical power would be used to charge the batteries.

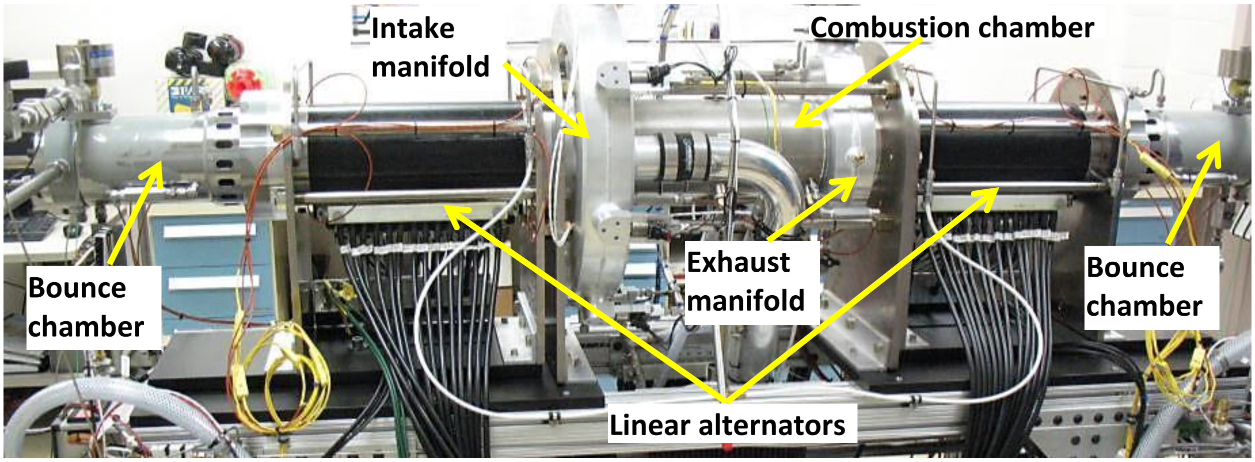

Figure 1: Sandia's Free Piston Engine – Linear Alternator Prototype

The FPLA was designed for high efficiency and low emissions. High efficiency is accomplished through a combination of high compression ratio (~30:1) and low equivalence ratio (~0.35) homogeneous charge compression ignition (HCCI) combustion of gaseous fuel. Low emissions are achieved by using lean mixtures of hydrogen. Based on the ideal Otto cycle, pushing compression ratios well beyond those of conventional engines allows for much higher thermal efficiency. Achieving these high compression ratios is easier in the free piston engine compared to crankshaft driven engines. The FPLA also allows for variable compression ratio which is not possible with mechanical linkages. Low equivalence ratio fuel mixtures improve thermal efficiency through better specific heat ratios than richer mixtures. In addition, lean fuel mixtures minimize nitrogen oxide (NOx) emissions, but are difficult to spark ignite. With hydrogen, hydrocarbon and CO emissions are eliminated. Thus, the goal of this project was to demonstrate the operation of a high compression ratio free piston engine operating with HCCI combustion of lean hydrogen mixtures.

The engine-alternator system shown in Figure 1 was designed, assembled and operated over a 2-year period at Sandia National Laboratories in Livermore, CA. This report primarily contains a description of the as-built system, modifications to the system to enable better performance, and experimental results from start-up, motoring, and hydrogen combustion tests.

Figure 2 shows one of the twin, three-piece pistons. The 29.4” long pistons have a mass of about 4.9kg with a diameter of 3.189” on the combustion end (left) and 2.892” on the bounce end (right). The combustion end includes two bronze impregnated Teflon compression rings while the bounce end has only one. The two piston ends are made of anodized 7075-T6 aluminum alloy, while the magnet array backiron (middle) is constructed of 1018 steel to enhance the magnetic circuit. The array of permanent magnets or “mover” consists of two, 10 mm wide and four, 20 mm wide Daido ND-39R radially-magnetized neodymium-iron-boron permanent magnets. The magnets are 81mm outer diameter by 73mm inner diameter and are arranged in alternating polarity and generate five toroidal magnetic fields. Consequently voltages are induced in five coils of the alternator simultaneously when the mover is in motion.

Figure 2: Photo of one of the piston assemblies

On either side of the combustion chamber are the Magnequench linear alternators. A schematic of one of the alternators is shown in Figure 3. The maximum mover stroke is 200mm and the mover-stator air gap is 1 mm. The stator body is comprised of an array of 14 coil-and-bonded-iron-core units and the pole pitch is 22 mm. Each coil consists of 14 turns of 4.064 x 0.762mm square magnet wire. The coil resistances and inductances are approximately 0.0245Ω, and 165µH, respectively. The mirror image coil pairs of the alternator stators, one on the left side and one on the right side, are connected in parallel and the electricity generated is dissipated directly through a bank of 14 water cooled load resistors. Connecting the mirror image coils in parallel provides a means of synchronizing the left and right side pistons through the electromagnetic forces. As one mover takes a lead over the other, the inductive coupling of their circuits places a greater electro-mechanical load on the leading mover, compared to the lagging one. Hence, the movers are drawn together in relative position.

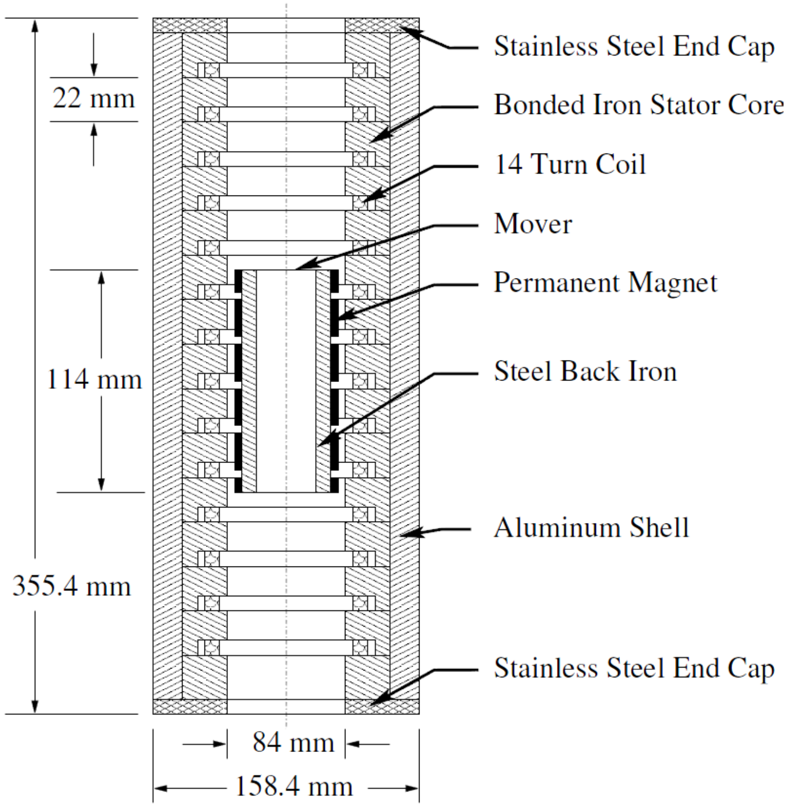

Figure 3: Schematic of a Magnequench linear alternator

To start the piston motion and motor the pistons without combustion, a pneumatic system was devised to inject compressed gas into the bounce chambers when the pistons approach BDC and vent it to a controlled pressure near TDC. To get sufficient kinetic energy into the pistons on the first cycle, the bounce chamber cylinders must pressurize quickly so helium was used as the working fluid. The He start system consists of a small vessel at high pressure upstream of a solenoid valve attached to each bounce chamber. In this way a controllable and repeatable energy input is enabled, requiring only that the two solenoid valves open simultaneously. This system was used standalone during initial tests, then later supplemented with combustion for improved repeatability. Note that helium is only used in the starting system. Thereafter, mechanically actuated valves allow compressed nitrogen into the bounce chambers through the heads on either end. Figure 4 shows both the N_2 supply to the bounce chamber heads and the He start system.

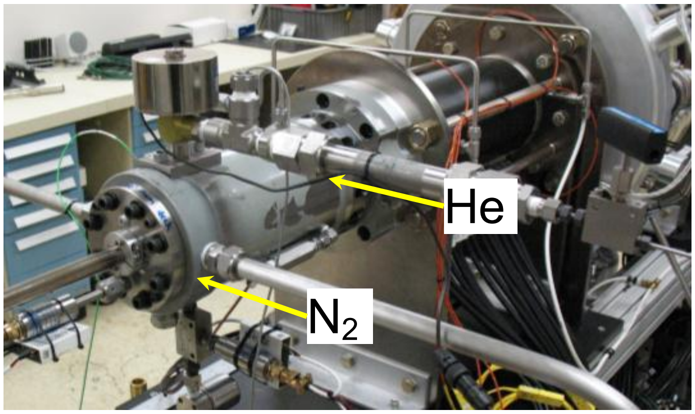

Figure 4: Photo of the gas supply to one of the bounce chambers

A schematic of the bounce chamber pneumatic drive system is shown in Figure 5. As the piston nears BDC, the air injection valve is actuated by a set of 12 pins threaded into the piston top. The valve uses an annular valve plate that seals on thin rings against a mating nose at the ID and outer head at the OD. A set of 16 compression springs is used to close the valve when there is minimal pressure differential across it, though the pressure differential provides the main seating force. The annular volume behind the valve plate is fed from the N_2 supply system at pressures up to 1200 psi. The momentum of the piston provides the force to open the valve. Pressurized N_2 then enters the bounce chamber while the piston slows to BDC and then accelerates in the opposite direction closing the valve again. The P-V work of the gas drives the pistons back to TDC to achieve a desired compression ratio. As the pistons approach TDC the bounce chamber vent ports open and the gas vents to atmosphere through a vent manifold with a computer controlled butterfly valve to set the vent pressure. This way, the compression ratio of the combustion chamber is set by controlling the air injection pressure in the bounce chambers. Similarly, the extent of piston travel into the bounce chambers is adjusted by controlling the vent pressure.

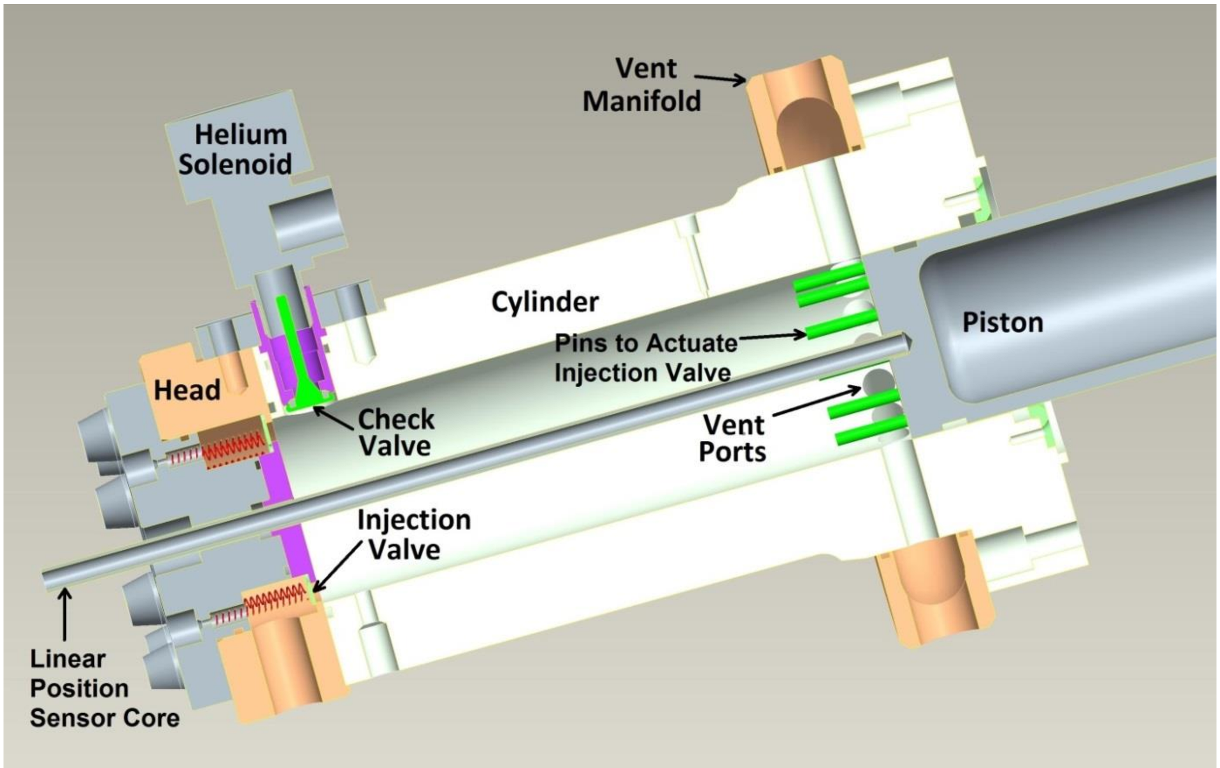

Figure 5: Cross-section of a bounce chamber showing the pneumatic drive system

The combustion system consists of fuel and air delivery subsystems, intake and exhaust manifolds, and a water-cooled combustion cylinder. The combustion chamber bore is 3.195" with exhaust port opening/closing at 7.482" from the center plane, giving a trapped volume of 1.97L assuming ideal piston synchronization. The intake ports open later at 7.875" from the center plane, allowing time for residual cylinder pressure to blow down through the exhaust. The cylinder was made from AISI 4340 steel hardened to Rockwell C 38-40. In addition to the gas flow ports, the cylinder has four instrumentation ports spaced at 90 degrees around the chamber circumference at the midpoint. Two of these ports are used for pressure transducers while the other two are unused. Finally the chamber has six lubrication ports, three on each side of the midpoint.

Hydrogen is supplied to the fuel injection system through a regulator which drops the pressure to 50 psig just upstream of the hydrogen flow meter which is calibrated to an accuracy of 1% of full scale. Downstream of the flow meter, the hydrogen supply line runs to a buffer volume to dampen any pressure fluctuations due to the opening and closing of fuel injectors. A solenoid control valve is used to allow hydrogen to the fuel injector manifold and is connected to the FPLA safety system. A pressure gage is attached to the manifold to monitor the pressure just upstream of the five commercially available gaseous port fuel injectors used to obtain the required fueling rate. The hydrogen fuel injectors are fired once per cycle, triggered by piston position. A combination of pulsewidths and number of fuel injectors was used to control the amount of hydrogen injected per cycle. The hydrogen is injected into the intake manifold which surrounds the combustion chamber intake ports. Air flow to this manifold is provided by a two-stage regenerative blower at rates between 125 and 150 cfm depending on the FPLA operating frequency.

CFD modeling had been performed to determine the intake port and manifold geometry needed to obtain plug flow for optimal scavenging and charge mixing. This modeling effort was described in [1]. Based on the results, the intake manifold was designed to provide stratified, uniflow scavenging. The modeling results suggested that this approach could achieve high scavenging efficiency with minimal short circuiting as well as adequate mixing for high combustion efficiency.

To analyze the performance of the FPLA, a large number of diagnostics were used. The key measurements used for energy balance and efficiency calculations include piston positions, combustion and bounce chamber pressures, air and hydrogen flow rates, and electrical currents to the load resistors. Piston position measurements were made with variable inductor displacement sensors. Care was taken to properly analyze the piston position readings and convert them to cylinder volumes. Combustion chamber pressure was measured by two redundant Kistler piezoelectric transducers with 300 bar measuring range. Bounce chamber pressures were measured with Kistler piezoelectric transducers with 250 bar measuring range. Intake air flow was measured using a turbine flowmeter with a 250 cfm range. Fuel flow rate was measured using a Sierra Instruments thermal mass flow meter with 0.695 g/s hydrogen range. Electrical current output from the linear alternators was measured at each load resistor using an instantaneous output Hall effect current transducer with ±300 A measuring range.

The FPLA was intended to be motored with the pneumatic drive system to reach a desired compression ratio before fuel was introduced. Thus, initial testing was carried out to assess the motoring system and overall system operation prior to combustion experiments. Bounce chamber pressure-volume data for a typical motoring test are shown in Figure 6. During this test the pneumatic drive system was set to a pressure of approximately 1,000 psig (6.9×10^3 kPa). As the figure shows, the bounce chambers are compressed to the point at which the air injection valves are actuated and the cylinders fill with high pressure gas as the pistons continue to move outward until their kinetic energy has been absorbed. As the pistons move back inward, the air injection valves close, and the injected gas is expanded. Near the end of the inward stroke, vent ports in the bounce chamber cylinders open, allowing the cylinders to vent to near atmospheric pressure before starting the next cycle. Early in the test, pressure in the vent system plumbing has not yet stabilized, leading to higher net energy addition for the first 10 to 15 cycles. Typically, pressure-volume work from the pneumatic drive system was input at a rate of 33 to 41 kW, and an electrical output of 16 to 20 kW was obtained.

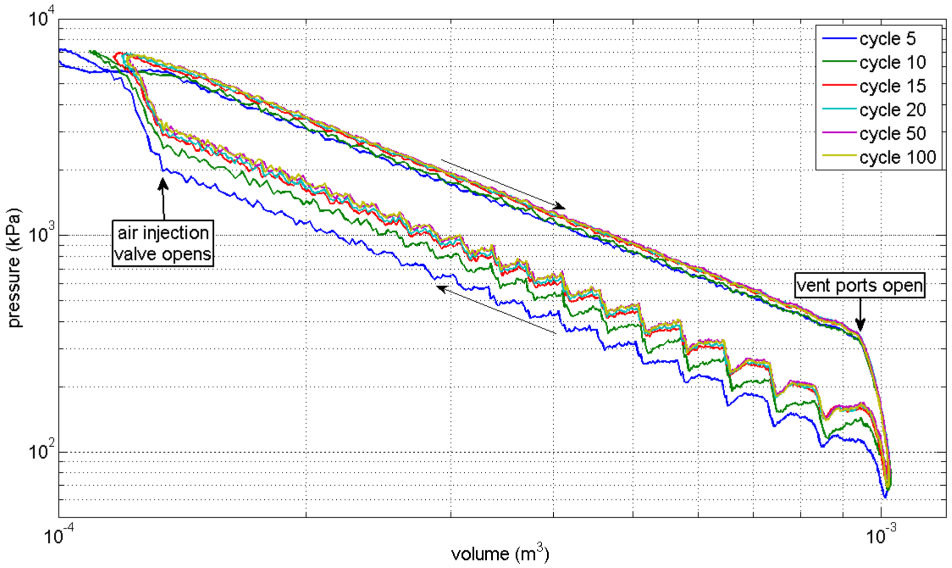

Figure 6: Bounce chamber logP-logV data from a typical motoring test

A time history of the pneumatic drive system pressure is shown in Figure 7. The supply pressure droops by about 20 psi initially due to the regulator, but the pressure is then maintained within 10 psi by the controller throughout the test. The bounce chamber vent system begins evacuated, but quickly rises in pressure and stabilizes at 3 to 4 psi above atmospheric.

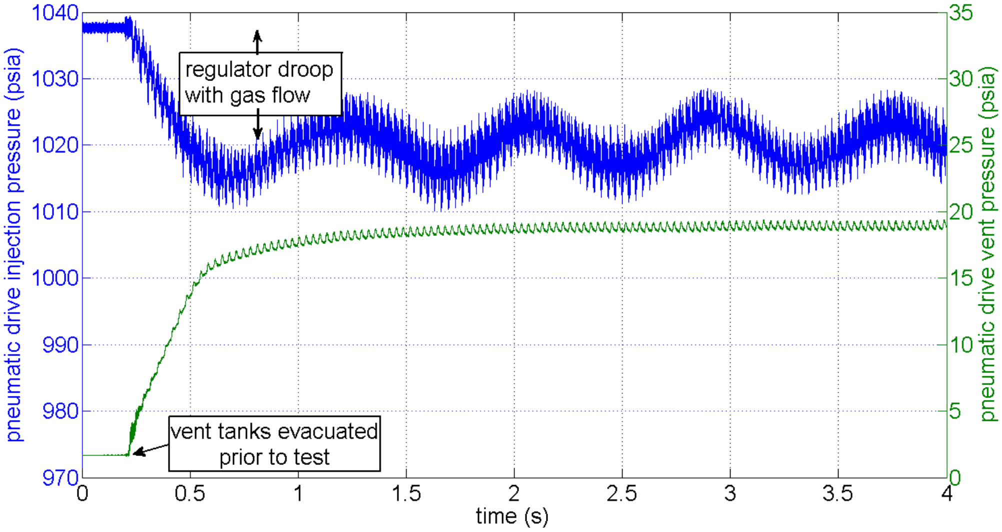

Figure 7: Example of supply and vent pressure of the pneumatic drive system

With no combustion energy input, compression ratios of 40:1 or higher were typically required for sustained operation. Engine operating frequency under these conditions was about 32 Hz. Operating frequency and compression ratio for individual motoring cycles are plotted in Figure 8, showing the range of values seen in typical tests.

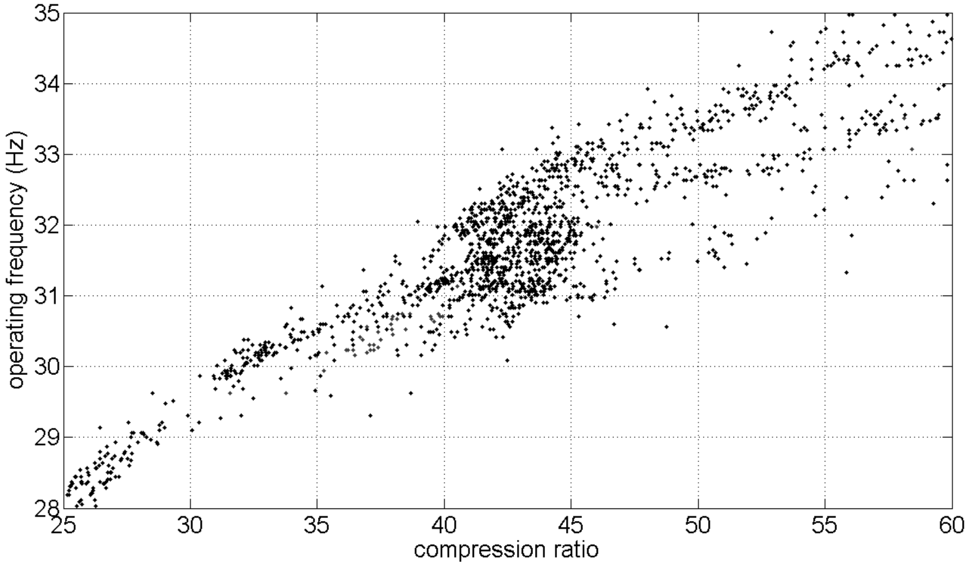

Figure 8: Range of motoring compression ratios and operating frequencies

A typical combustion chamber pressure-volume diagram for motoring operation is shown in Figure 9. In the ideal case, this would be isentropic compression and expansion and the lines would be perfectly straight and directly on top of one another. In reality, the combustion chamber expands on a line slightly below the compression line due to heat and gas losses near TDC.

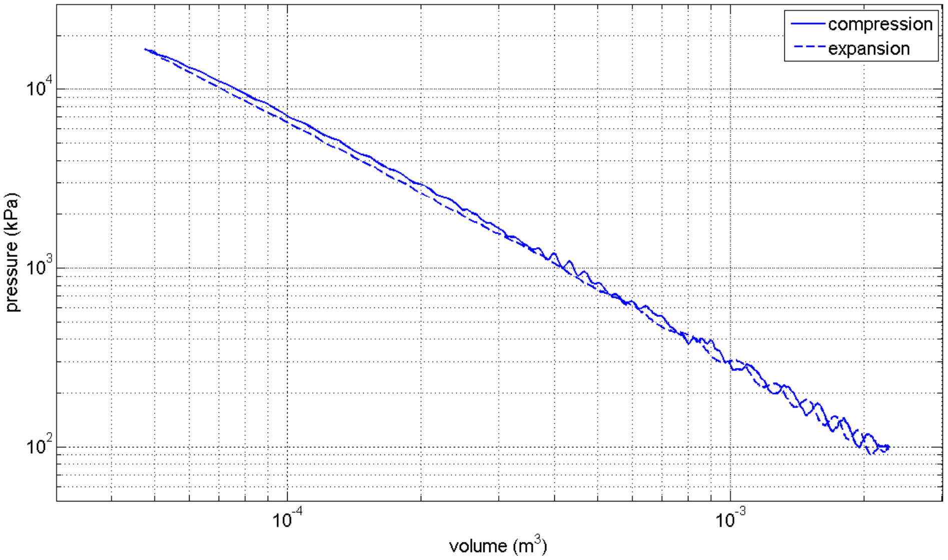

Figure 9: Typical combustion chamber logP-logV diagram during motoring

A typical motoring energy balance is shown in Figure 10. The bounce chamber and combustion chamber energy inputs are calculated on a cycle-by-cycle basis from the pressure-volume data. The electrical energy output is calculated from current measurements made at each load resistor, along with the known resistance value. Losses to coil internal resistance are calculated in a similar manner. In this particular test, electrical output to the load was 49% of the work input, coil internal resistance losses were 4%, losses to piston friction and alternator eddy currents were 33% (predominantly piston friction), and combustion chamber heat and gas losses were 14%.

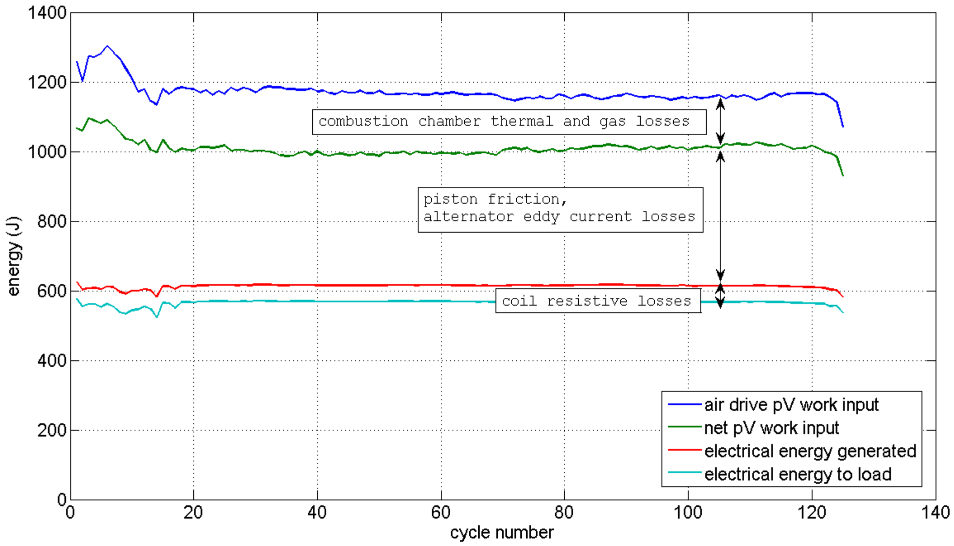

Figure 10: Energy balance for a typical motoring test

In preparation for combustion experiments, longer duration motoring tests were attempted. Although the longest was limited to about 30 seconds, these tests also demonstrated passive piston synchronization through the linear alternators. The graph in Figure 11 shows piston synchronization error for five tests. This error is the relative difference in the piston positions with respect to the engine centerline. For many tests this error is just a few mm, compared to the 220 mm travel of each piston. Based on simulation results, asynchronous motion is initiated by a difference in friction between the two pistons. However, as the separation grows, the electromagnetic drag on the pistons works to restore synchronous motion. Importantly, this data shows that it is possible to operate the FPLA system without complex active controls to keep piston motion in sync, at least within the limited duration of these tests.

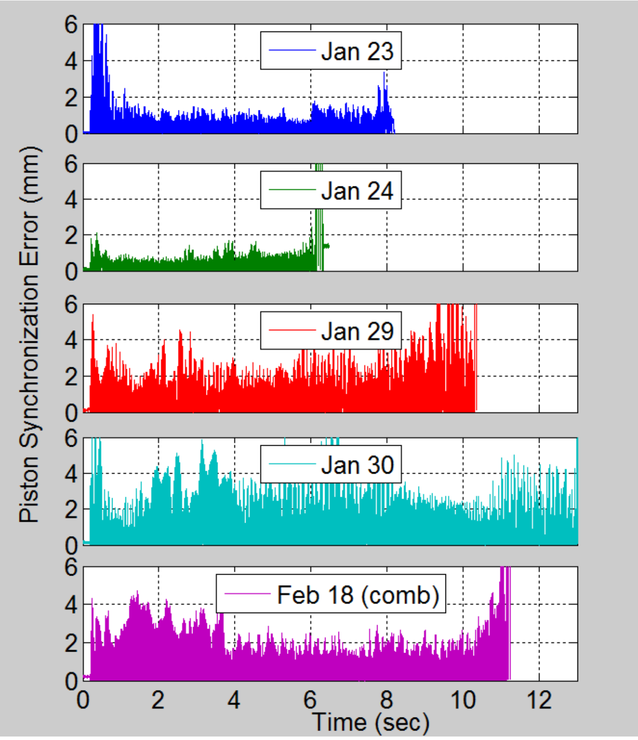

Figure 11: Piston synchronization error for several motoring tests

Another important observation from the motoring tests was that piston synchronization has a significant effect on the electrical output. As piston synchronization error increases, electrical output drops. Instantaneous electrical current measurements from an example data set are shown in Figure 12, along with piston positions. The plot on the left shows a cycle from the well-synchronized period around cycle 50, while the plot on the right shows a cycle from a poorly synchronized period around cycle 20. With the two pistons in good synchronization, the instantaneous coil currents for each side of the engine are nearly identical, summing to produce the maximum useful output, shown by the load resistor current. Meanwhile, on the right, piston 1 leads piston 2, causing coils in stator 1 to generate well over half of the overall output. In fact, with the first pulse of current generated, a portion of the current from stator 1 feeds backward through stator 2, resulting in a load current less than what had been generated by stator 1.

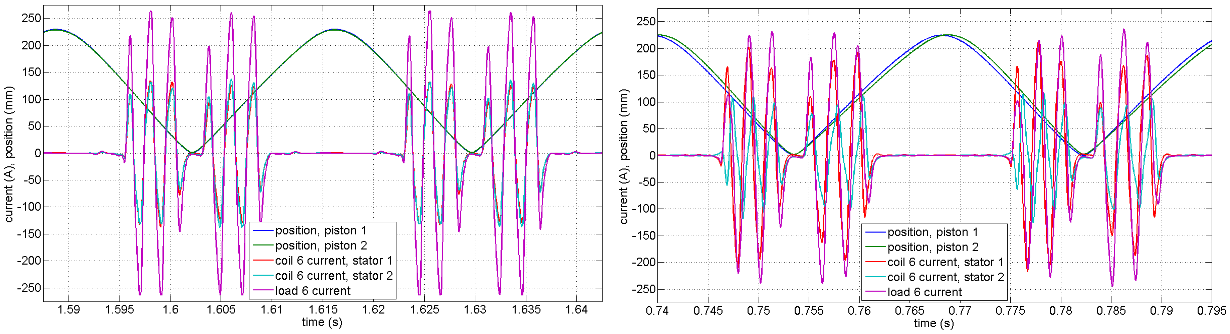

Figure 12: Comparison of electrical current output between well-synchronized and poorly-synchronized operation

Hydrogen combustion tests were carried out using both manual control of fuel load and automatic control. An example set of data obtained by manually increasing the fueling rate is shown in Figure 13 and Figure 14. A pneumatic drive pressure of 925 psia was used to maintain the compression ratio. The bounce chamber vent system was controlled at about 31 psia to allow higher combustion chamber fueling without the pistons over-traveling .

The compression ratio, equivalence ratio, and indicated thermal efficiency are shown in Figure 13. The equivalence ratio is calculated from the fuel mass flow rate and air flow rate.The indicated thermal efficiency shown is calculated as the combustion chamber pressure-volume integral over each cycle divided by the fuel chemical energy delivered, based on fuel mass flow rate and lower heating value. The jumps in indicated thermal efficiency around cycles 35, 65, and 130 are artifacts of step changes in fueling rate. For the stable period between cycles 250 and 350, an indicated efficiency approaching 54% is seen. During this time, the compression ratio at autoignition was approximately 29:1, and the equivalence ratio was around 0.15. Fuel-air cycle analysis using a hydrogen-air mixture at these conditions gives the ideal Otto cycle efficiency as 67%. At such a low equivalence ratio, the motoring losses discussed above are a significant fraction of the fuel energy input and account for much of the discrepancy between the measured and ideal efficiencies.

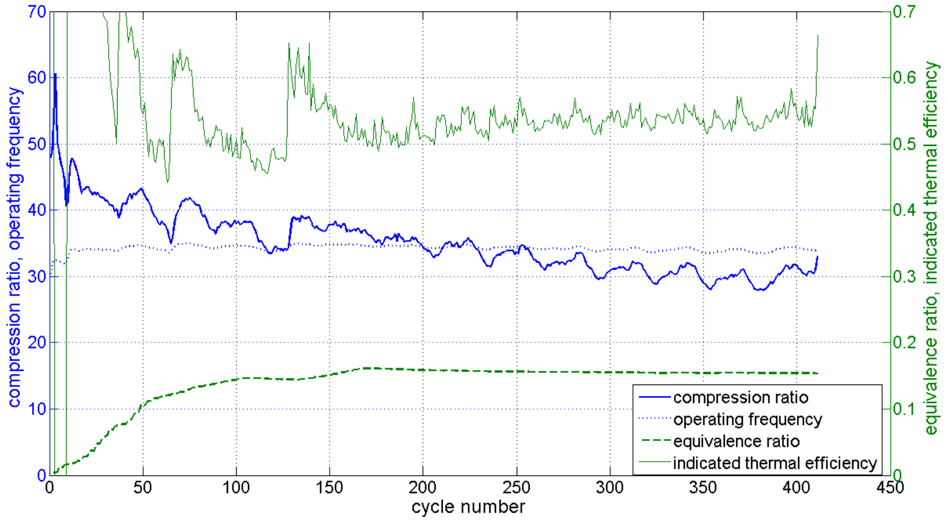

Figure 13: Compression ratio, operating frequency and indicated thermal efficiency for an example combustion test with manual fuel control

The pressure-volume curves for a few cycles are plotted along with the ideal cycle calculation in Figure 14. The compression strokes follow reasonably well along the isentropic compression line, while the pressure rise at combustion falls short of the ideal cycle. At these conditions, the combustion event takes about 150 μs to complete, occurring with minimal change in cylinder volume.

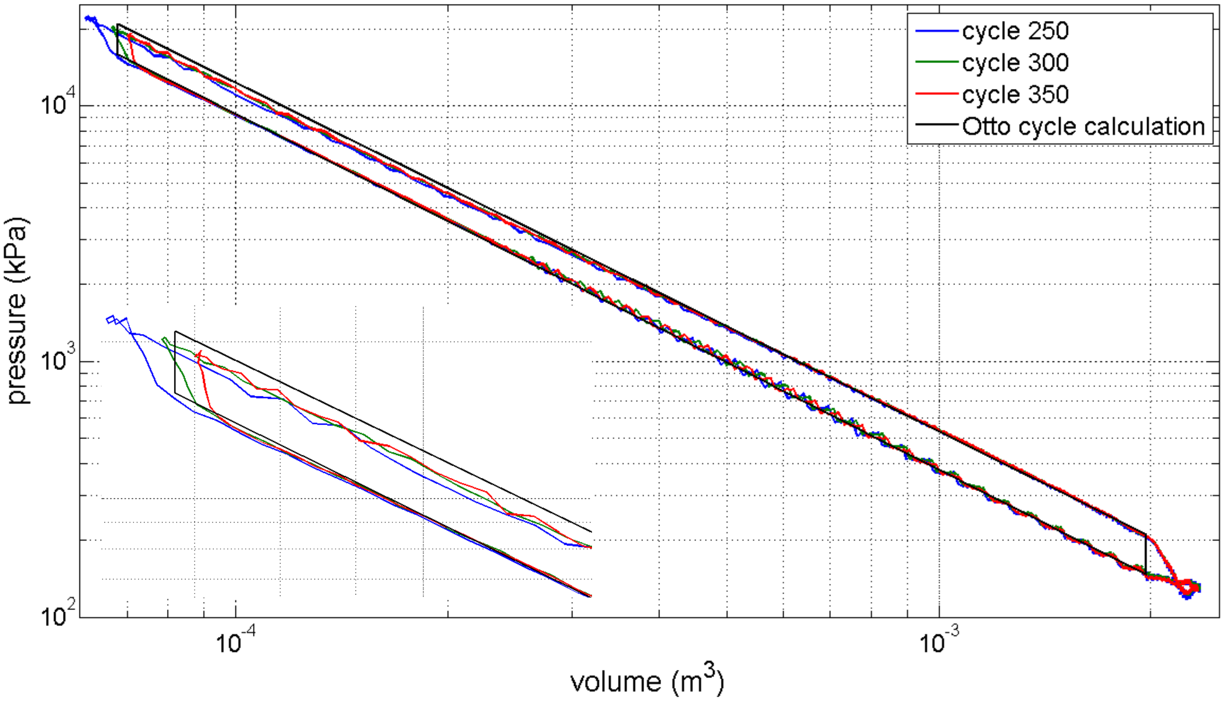

Figure 14: Combustion chamber logP-logV compared to ideal Otto cycle calculation

Over the course of combustion testing, a range of conditions and parameters were explored including fueling rate, compression ratio, and net input energy. Figure 15 shows a plot that examines the data sets as a whole. The plot shows how indicated fuel conversion efficiency (ratio of net combustion chamber energy to H_2 chemical energy) varies with fuel load. As more hydrogen is injected per cycle, the thermal and pressure losses become a smaller fraction of the combustion energy which results in a higher indicated efficiency. Note that these results do not necessarily correspond to full thermal equilibrium conditions. As the cylinder wall and piston tops warm up during each test, heat losses are expected to decrease, which could account for some of the spread in the data. Compression ratio is another factor, and is discussed below. Indicated thermal efficiency greater than 60% was measured for some cycles although this was not typical. Many tests, however, consistently reached efficiencies between 50% and 55%. Recent gasoline HCCI research has shown 47-48% gross indicated thermal efficiency for boosted intake conditions, and 42-43% for naturally aspirated conditions with 14:1 compression ratio [2]. Others have shown 56-59% gross indicated thermal efficiency at 18.7:1 compression ratio using reactivity controlled compression ignition [3]. Brake efficiencies for several modern turbocharged diesel engines compiled in [4] are in the 40-45% range, implying indicated efficiencies approaching 50%. Despite failing to reach the intended equivalence ratio of around 0.3, the indicated efficiency measurements of this study are comparable to, or slightly above, modern turbocharged diesel and boosted gasoline HCCI technology.

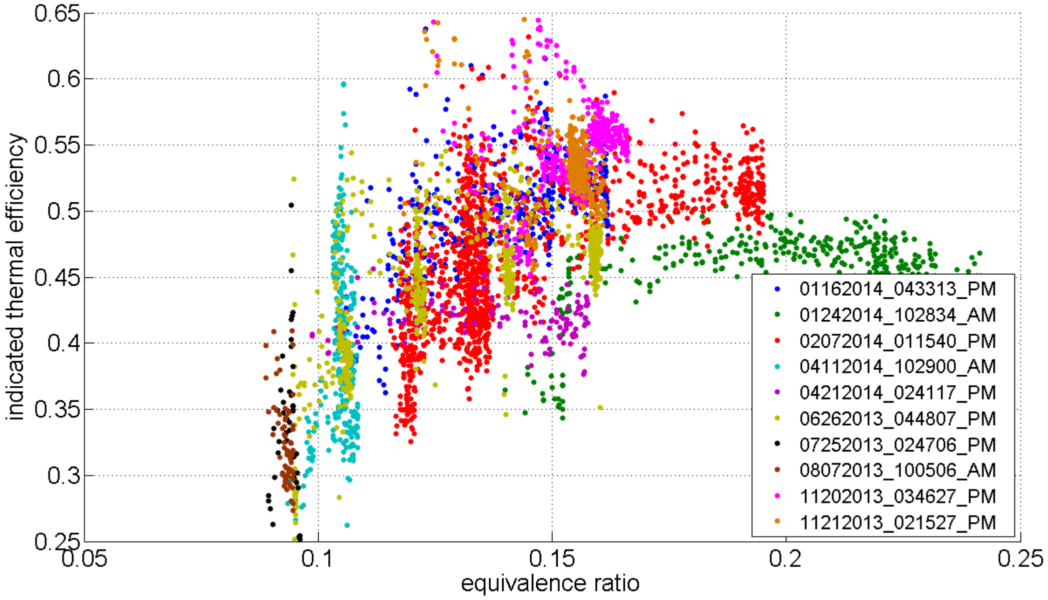

Figure 15: Indicated thermal efficiency as a function of equivalence ratio for a number of combustion tests

Figure 16 shows indicated thermal efficiency versus compression ratio. Overall, efficiency drops with increasing compression ratios. While this would not be expected based on an Otto cycle analysis, in a real engine crevice effects become more significant at higher compression ratios and thermal losses increase when compressing past the point of autoignition which was the case for many of the higher compression ratio points.

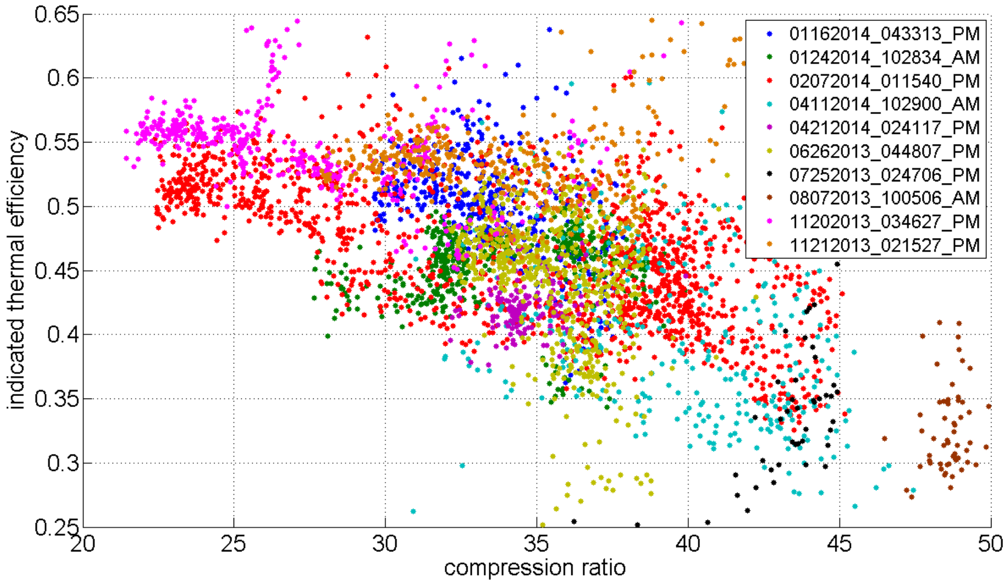

Figure 16: Indicated thermal efficiency as a function of compression ratio for a number of combustion tests

Based on the trends shown in Figure 15 and Figure 16, it would seem that even higher indicated thermal efficiency could be achieved if autoignition at TDC was coupled with higher equivalence ratio. For example, an equivalence ratio near 0.2 with a compression ratio near 20:1 might achieve an efficiency of 0.6 or greater. This was the goal of a number of the final experiments with the FPLA, however it proved difficult in practice to reach this operating point before the test would end due to piston synchronization, ring failure, or some other issue.

In addition to thermal efficiency, combustion experiments provided electrical output efficiency results. It was found that two effects had direct bearing on the maximum electrical energy output of the linear alternators. Firstly, it was shown through modeling and experiments that electrical energy output reached a plateau with piston speed. A Flux 2D model of the magnet/alternator coil coupling predicted that electrical current would plateau above an average piston speed of 15 m/s. This was confirmed through a number of experimental results. Secondly, data showed that piston speed reached a plateau with input energy. An average piston velocity of 15 m/s could be reached with a net input energy of less than 1000 J/cycle. Increasing this energy input to over 1200 J/cycle, a 20% increase, resulted in less than 7% increase in speed. This is likely due to a rapid increase in friction with the higher bounce chamber and combustion chamber pressures that result from the increased input energy.

The combination of these two effects is reflected in Figure 17 which shows electrical output efficiency as a function of the net input energy for several tests. Work-to-electrical efficiency is the ratio of the alternator energy to the net input energy. For the test data shown, the highest efficiency shown occurs at the lowest input energy (55% at 950 J/cycle). Energy input above 950 J/cycle is primarily dissipated as friction and produces very little increase in piston speed or electrical energy.

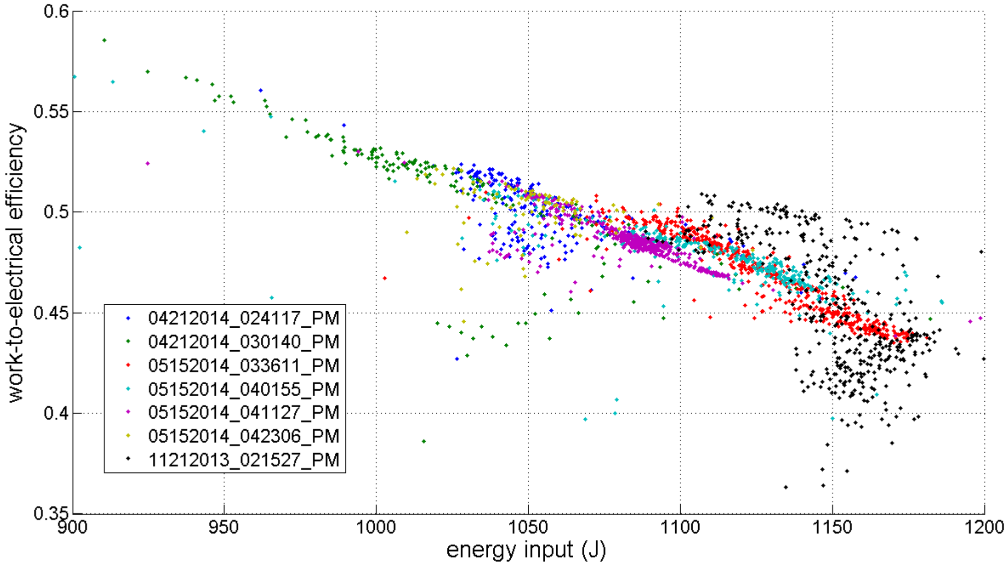

Figure 17: Electrical output efficiency as a function of net input energy for several tests

Thus, for highest efficiency, the FPLA should be operated with input energy below 950 J/cycle. However, as with equivalence ratio and compression ratio, this was difficult to achieve in practice. Enough input energy was needed to provide both a high enough compression ratio for combustion and actuation of the annular valves for the pneumatic drive. It was difficult if not impossible to get the FPLA to achieve the piston travel required to satisfy these two constraints with less than 950 J/cycle of input energy. The system ran more consistently and for longer duration when the input energy was higher. Design modifications would be required to consistently run at lower input energy. For example, using longer actuation pins such that the annular valves were actuated earlier in the piston stroke.

When combined, the indicated thermal efficiency and the work-to-electrical efficiency give the overall efficiency of the FPLA which is the electrical energy output divided by the input fuel energy. However, the FPLA was never operated with 100% of the input energy from combustion, so this value cannot be precisely stated without some assumptions. First, let’s assume that the highest thermal efficiency seen in the data (60%) could be achieved with all of the input energy from combustion. If it is then assumed that the maximum electrical output efficiency seen in the data (~56%) is achieved simultaneously, then the overall efficiency would be 33.6%. Typical values achieved with the FPLA were lower, around 20-25%, due to difficulty in controlling operation at the ideal conditions.

1. INTRODUCTION

As fuel efficiency of the typical American automobile becomes more important due to hydrocarbon fuel cost and availability issues, powertrain improvements will require smaller output engines combined with hybrid technologies to improve efficiency. In particular, hybrid electric vehicles (HEVs) will require an electrical generator of approximately 30 kW output. Unfortunately, current crankshaft spark-ignition internal combustion engines with optimized power outputs of 30 kW have thermal efficiencies of less than 32%.

Electrical generators with high efficiency and low exhaust emissions are needed for advanced HEV designs. Fuel cells are being developed for this purpose and PEM fuel cells in particular have achieved very high efficiency electrical generation with only water vapor as an exhaust stream. However, fuel cells are still currently quite expensive. In addition, the extensive development of the internal combustion engine (ICE) and the existence of a huge repair and maintenance infrastructure for piston engines are incentives to continue to develop combustion engine-based electrical generators.

For high efficiency, the ideal Otto cycle can be used as an upper bound for an ICE. In the Otto cycle, fuel energy is converted to heat at constant volume at the peak compression point. This produces the highest possible peak temperatures and thus the highest possible thermal efficiencies. In fact, thermal efficiencies of over 80% can be calculated for extremely high compression ratios. In practice, however, a number of technical challenges must be addressed to approach ideal Otto cycle performance at high compression ratio in a real system. These challenges include finite combustion durations, thermal losses, high pressures, and high friction.

Low or zero emissions presents a separate, but related challenge for the ICE electrical generator. For example, to minimize or eliminate nitrogen oxide (NO_x) formation, lean, homogeneous fuel/air mixtures are required [5, 6]. This precludes diesel combustion and spark ignition combustion is difficult with lean mixtures and suffers knock (uncontrolled autoignition) at high compression ratios.

Homogeneous charge compression ignition combustion could be used to solve the problems of burn duration and allow ideal Otto cycle operation to be more closely approached. In this combustion process, a homogeneous charge of fuel and air is compression heated to the point of autoignition. Numerous ignition points throughout the mixture can ensure very rapid combustion [7]. Very low equivalence ratios (ø ~0.3) can be used since no flame propagation is required. Further, the useful compression ratio can be increased as high temperatures are required to autoignite weak mixtures [8]. In general, HCCI combustion has been shown to be faster than spark ignition or compression ignition compression. Much leaner operation is possible than in SI engines, so lower NOx emissions results. In order to maximize the efficiency potential of HCCI operation much higher compression ratios must be used and a very rapid combustion event must be achieved. Recent work with higher compression ratios (~ 21:1) has demonstrated the high efficiency potential of the HCCI process [9, 10].

To achieve high compression ratio HCCI combustion, a free piston geometry is better suited than a convention crankshaft engine. Several advantages have been noted for free piston IC engines.

First, the compression ratio of the engine is variable; this is dependent mainly on the engine's operating conditions (e.g., fuel type, equivalence ratio, temperature, etc.). As a result, the desired compression ratio can be achieved through modification of the operating parameters, as opposed to changes in the engine's hardware. An additional benefit is that the mechanical friction can be reduced relative to crankshaft driven geometries since there is only one moving engine part and no piston side loads. Also, combustion seems to be faster than in conventional slider-crank configurations. Further, the unique piston dynamics (characteristically non-sinusoidal) seems to improving the engine's fuel economy and NOx emissions by limiting the time that the combustion gases spend at top dead center (TDC) (thereby reducing engine heat transfer and limiting the NO_x kinetics). Finally, one research [11] reports that the cylinder/piston/ring wear characteristics are superior to slider/crank configuration by a factor of 4. Thus the combination of the HCCI combustion process and the free piston geometry is expected to result in significant improvements in the engine's thermal efficiency and its exhaust emissions.

For electricity generation from the free piston engine, a linear alternator is integrated into the free piston geometry. The linear generator is designed such that electricity is generated directly from the piston's oscillating motion, as rare earth permanent magnets fixed to the piston are driven back and forth through the alternator's coils. In this arrangement, mechanical losses in the system are dramatically reduced since there is essentially one moving part, and this allows engine operation at a more or less constant piston speed. These points aid in the generator design and further improve the fuel-to-electricity generation efficiency of the device.

In recent years there has been a resurgence of interest and activity around free piston engines, in particular as electrical generators for HEVs. Mikalsen and Roskilly [12] have summarized a number of academic efforts related to free piston technology and more recently Hanipah, Mikalsen and Roskilly [13] have given an overview of free piston engine development in the automotive industry. Their summary draws primarily from published patent information, since vehicle OEMs are less likely to publish journal articles. Work on free piston electrical generators for HEVs is discussed from General Motors, Toyota, Volvo, Ford, Honda, and Mazda. Major challenges to free piston engine development identified include piston motion control, thermal management, and start-up. Much of the information presented, however, has not been verified through testing of actual hardware.

Two recent efforts that have included testing of free piston prototypes have been carried out by Toyota Central R&D Labs and the German Aerospace Center (DLR). The Toyota group has developed a two-stroke free piston engine linear generator (FPEG) that consists of a single piston with a combustion chamber on one end, a gas spring chamber on the other end and an integrated linear generator [14, 15]. Key distinguishing features of the Toyota design include a stepped piston shape termed a "W-shape" and the inclusion of active cooling. The W-shape piston has a smaller diameter combustion end and a larger diameter, annular gas spring end. There are three purported advantages of this design. The first is that the large diameter gas spring requires lower pressure and thus lower temperature that results in lower heat loss. The second is that the shape allows for an oil cooling passage to cool the combustion end. The third is that the permanent magnets of the linear generator are attached to the larger diameter annulus which provides a sufficient heat transfer barrier that the magnets are unaffected by combustion heat.

A one-dimensional numerical model of the system was used to understand and assess the performance of the Toyota device. Both spark ignition (SI) and premixed charge compression ignition (PCCI) combustion were simulated and the desired 10 kW power generation was achieved in both cases. For the PCCI case, the FPEG was simulated at 40 Hz with a compression ratio of 19:1 and an equivalence ratio of 0.4 and achieved an indicated thermal efficiency of 52.7% and an overall efficiency of 42%. However, stability for the PCCI case was tenuous and only found within a tight operating region. For the SI case, the range of ignition timing for stable operation was found to be limited and much narrower than conventional engines. A lower compression ratio was simulated for the SI case, 14.5:1, and indicated thermal efficiency and overall efficiency were lower at 45.4% and 36.2% respectively.

Based on the simulation results, a prototype device was developed and tested. Stable operation was demonstrated over a period of more than 4 hours, although at a reduced cycle frequency and compression ratio (23 Hz and 7:1). SI combustion of gasoline was used in the prototype experiments and the sensitivity to ignition timing predicted by the simulation was validated. A fairly complex feedback control system was developed for the FPEG prototype that used the three-phase linear generator as a linear motor to correct piston motion relative to an ideal reference cycle. A quantitative analysis of efficiency was not performed in this feasibility study.

The work performed at the German Aerospace Center has been published in a series of articles over the last several years [16 - 18]. The DLR group has focused on homogeneous charge compression ignition (HCCI) combustion in a free piston linear generator designed for hybrid electric vehicles. In the most recent publication [16], this team considers concepts for integration of the FPLG system in vehicles. They focus on a design with two opposing pistons for mass balance and a central combustion chamber, much like the system that will be described in this report.

A proof-of-concept system was built by the DLR group, called a functional demonstrator. As such, the system used a single piston rather than two opposed pistons. As with the Toyota R&D system, the DLR system used the linear generator as a motor for start-up. The system was successfully operated and provides up to 10 kW at a piston frequency of about 20 Hz. The combustion system uses a two-stroke SI process and gas exchange occurs by head loop scavenging with two inlet and one outlet electromagnetic valves. Direct injection of gasoline was the fuel source. The system achieved 32% indicated thermal efficiency and 18% total efficiency (chemical to electrical conversion).

At Sandia National Laboratories, a free piston engine – linear alternator (FPLA) has been developed for over a decade. Van Blarigan and coworkers have published a number of articles describing various aspects of the development effort over the years. In a 1998 study, Van Blarigan et. al. [19] discuss the design of a single piston FPLA with combustion chambers on either end and a central linear alternator. The design was based on using high compression ratio HCCI combustion with low equivalence ratio fuel mixtures. The paper describes experiments with a rapid compression-expansion machine (RCEM) to determine achievable efficiencies and emissions with this combustion scheme. Fuel/air mixtures with eight different fuels were tested: propane, natural gas, hydrogen, methanol, n-pentane, hexane, n-heptane, and isooctane. Fuel/air equivalence ratios varied from 0.32 to 0.37 depending on the fuel. Initial charge temperatures of 25 C, 50 C, and 70 C were used and a range of compression ratios were tested. The premixed charges were compressed to the point of autoignition and then expanded. The cycle thermal efficiency was calculated from measurements of pressure and piston displacement and the NOx, hydrocarbon, and CO emissions were measured for the combustion gases using exhaust gas analyzers. Indicated thermal efficiencies up to 56% were measured for propane, natural gas and hydrogen. HC and CO emissions varied from 100 ppm to several thousand ppm for the fuels, except hydrogen where none would be expected. NOx emissions were generally low for all fuels except hydrogen which experienced higher levels (up to 550 ppm) with higher initial charge temperature and compression ratio.

In 1999 [20], Sandia reported on a numerical study of HCCI combustion with hydrogen in a free piston architecture. The steady-state operation of a FPLA was analyzed using a zero-dimensional thermodynamic model with detailed chemical kinetics and empirical scavenging, heat transfer, and friction component models. The study results showed that the variable compression ratio could be controlled with input parameters and would need to be tightly controlled to prevent under- or over-compression, that HCCI combustion was nearly constant volume, significantly reduced NOx emissions could be achieved, and scavenging could be very important to engine efficiency. Indicated thermal efficiency of near 65% was predicted for compression ratios of about 30:1.

Following up on the idea that the scavenging system would be critical to achieving high efficiency in the FPLA, Goldsborough and Van Blarigan carried out a computational fluid dynamics (CFD) analysis of various scavenging approaches for the engine including loop, hybrid loop, and uniflow scavenging [21]. KIVA-3V was used to model the options. The results of the analysis showed that a scavenging system could be designed that allowed for minimal losses and high efficiency using the uniflow method.

While these publications focused on the combustion system, Sandia also worked to understand and design a linear alternator system. In [22], Aichlmayr and Van Blarigan report on modeling and experimental characterization of a linear alternator for the FPLA application. In collaboration with Sandia, a prototype linear alternator was designed and fabricated by Magnequench Technology Center. A model of this alternator was developed and performance predictions were compared with experimental results obtained by running the linear alternator using one cylinder from a four-cylinder diesel engine. The comparison between model and experiment was quite good and validated the model development method.

Based on this work, the DOE Vehicle Technologies Office funded Sandia to design and build a proof-of-concept FPLA design with the goal of approaching ideal Otto cycle performance through HCCI operation at high compression ratios. To minimize emissions, lean hydrogen/air mixtures would be used for the fuel. The configuration for the engine is an opposed-piston design with a central combustion chamber and gas spring chambers at either end. This configuration was chosen to minimize vibration due to piston motion as well as for high potential efficiency. Magnequench linear alternators are employed with the engine to complete the FPLA system.

The overall objectives of the project were the following:

- Study the effects of continuous operation (i.e. gas exchange) on indicated thermal efficiency and emissions of an opposed free-piston linear alternator engine utilizing homogeneous charge compression ignition (HCCI) combustion at high compression ratios (~20-40:1).
- Concept validation of passively synchronizing the opposed free pistons via the linear alternators, providing a low cost and durable design.
- Proof of principle of electronic variable compression ratio control, allowing optimized combustion timing and fuel flexibility, by means of mechanical control of bounce chamber air pressure.
- Provide a research tool to explore the free-piston engine operating envelope across multiple inputs: boost level, equivalence ratio, alternative fuels.

This report describes the FPLA system developed under this program and the results of an experimental evaluation of the system. The FPLA subsystems will be described in detail along with the experimental facility used for testing. FPLA subsystems include the pistons, combustion system, linear alternators, gas spring or bounce chambers, and start system. The facility description will include the data acquisition (DAQ) and controls system, a pneumatic drive system, the fuel delivery system and the exhaust analysis system.

The FPLA demonstration has been carried out in stages. First, synchronous starting of the opposed pistons will be described followed by synchronous motoring. Design modifications and the development of experimental procedures leading to combustion will be described. Finally, combustion results will be discussed and analyzed and energy efficiency and linear alternator performance will be described and compared to model predictions.

2. FREE PISTON ENGINE GEOMETRY

2.1. Overall Engine Configuration

The Sandia free piston linear alternator (FPLA), shown in cross-section in Figure 18, uses an opposed piston design with two-stroke uniflow scavenging for gas exchange and timed port fuel injection for fuel delivery. Linear alternators are used for power extraction and piston synchronization, while bounce chambers are used as a means of energy storage to provide compression work for the next cycle. The central combustion chamber, intake and exhaust manifolds, and left and right linear alternators and bounce chambers are called out in the figure. The three-piece pistons (combustion end: brown, magnet array: green, bounce end: light grey) are shown at bottom dead center (BDC) in the figure so that the intake and exhaust ports in the combustion chamber are uncovered. A picture of the FPLA is shown in Figure 19 and key engine parameters are listed in Table 1. The following sections will describe the key features of the FPLA in more detail.

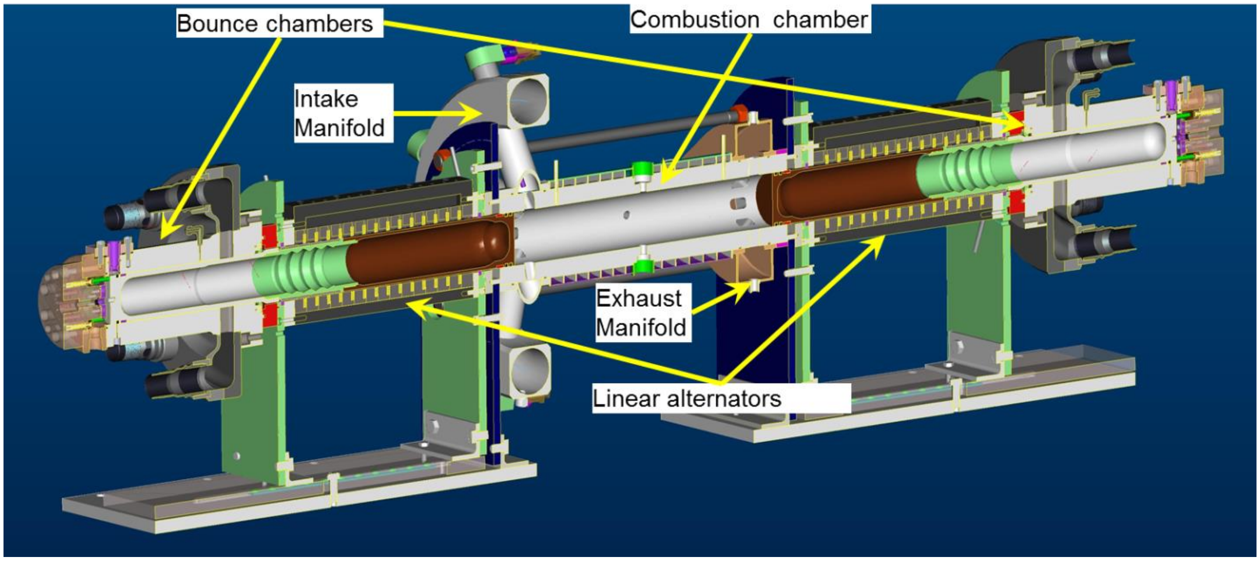

Figure 18: Cross-section of the FPLA prototype

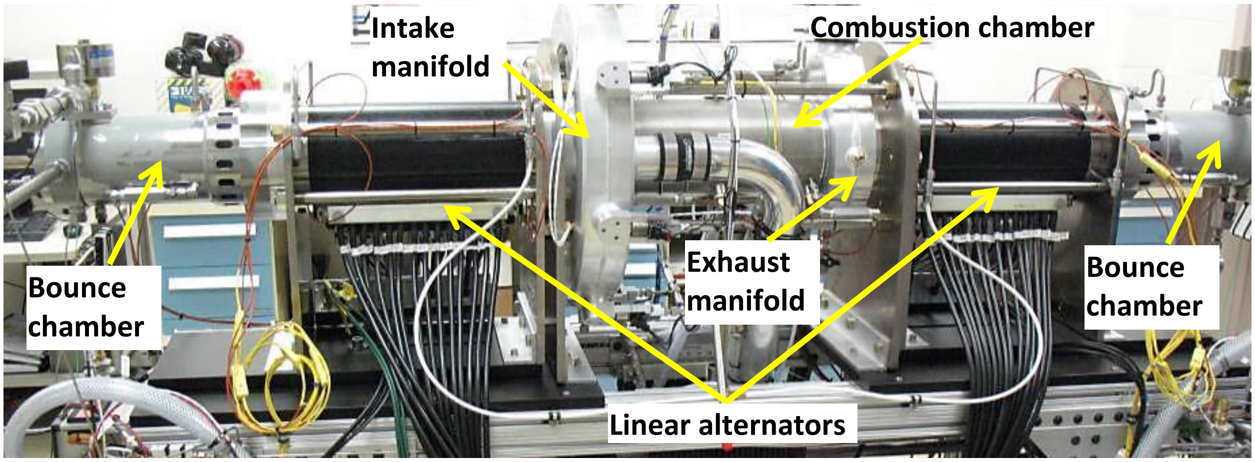

Figure 19: Photo of the FPLA prototype

Table 1: Main parameters of the FPLA system

Trapped Volume	Combustion Bore	Stroke per piston (nominal)	Overall Length	Operating Frequency	Electrical Power Output
Liters (in^3)	mm (in)	mm (in)	mm (in)	Hz	kW
1.97 (120.2)	81.15 (3.195)	220 (8.66)	2286 (90)	30-35	15-19

2.2. Pistons and rings

One of the FPLA piston assemblies is shown in Figure 20. Each piston is composed of three segments, namely the combustion piston end, the bounce piston end, and the magnet-backiron assembly. The two piston ends are made of anodized 7075-T6 aluminum alloy, while the backiron is constructed of 1018 steel to enhance the magnetic circuit. The array of permanent magnets will be described in section 2.4. As seen in Figure 20, the combustion and bounce ends have several differences. Firstly, the combustion end has a slightly larger diameter at 3.189" compared to the bounce end at 2.892". Also, the combustion end includes two compression rings while the bounce end has only one. This is due to the much higher pressure created in the combustion cylinder than the bounce cylinder. The left and right-hand pistons are essentially identical and each piston assembly is 29.4" long and has a mass of around 4.9kg. The two piston assemblies were balanced to within 5g of one another by adding a mass to the inner diameter of the lighter piston.

The one piece, gapless piston rings, designed and fabricated by Cook Compression, are made of bronze impregnated Teflon with the trade name Tru Tech 3210. This material was chosen for sealing performance and tolerance to poor lubrication. For durability reasons these rings are not practical for a commercial device, but they were adequate for initial testing of this research engine. These rings seal by the cylinder gas pressure forcing the ring against the cylinder wall and ring groove. Thus, the higher the gas pressure the larger the force and the friction between the piston and cylinder.

Figure 20: Photo of one of the piston assemblies

Early tests of the pistons indicated that the friction force was higher than expected. A series of friction tests were carried out to understand the issue. First, the pistons were tested with the second combustion chamber ring removed, but no difference was found indicating that the first ring accounted for all of the friction. Next, new compression rings with ½ of the original interference between ring and cylinder were tested. No difference in friction was found with these tests either, indicating that the pressure load on the ring dominates the friction rather than the ring interference. Finally, friction tests were performed with the rings removed. These tests showed that friction force was reduced by ~50%, indicating that half of the constant friction term is from rings, half from piston-to-cylinder friction plus other seals.

High friction requires high air drive pressures and flow rates to keep the pistons motoring. In addition, high frictional energy dissipation directly reduces the overall efficiency of the FPLA. So, an effort was undertaken to reduce piston friction. The result was a redesign of the pistons to include modified compression rings and rider rings. It was found through experiment and modeling that sliding friction between the compression rings and the cylinder was the dominant factor. This force is proportional to the contact area. Thus, by cutting the ring width in half, friction could be reduced. This was confirmed through tests of the current pistons with the compression rings cut in half as shown in Figure 21.

Figure 21: Photo of piston ends with cut rings

Redesigned piston ends are shown in Figure 22. The compression ring widths were cut in half and a rider ring was added to each end to keep the piston concentric with the cylinders. Piston diameter was also modified to increase the clearance primarily to the combustion cylinder. This was due to a concern that thermal expansion would lead to seizure of the combustion end with the original design.

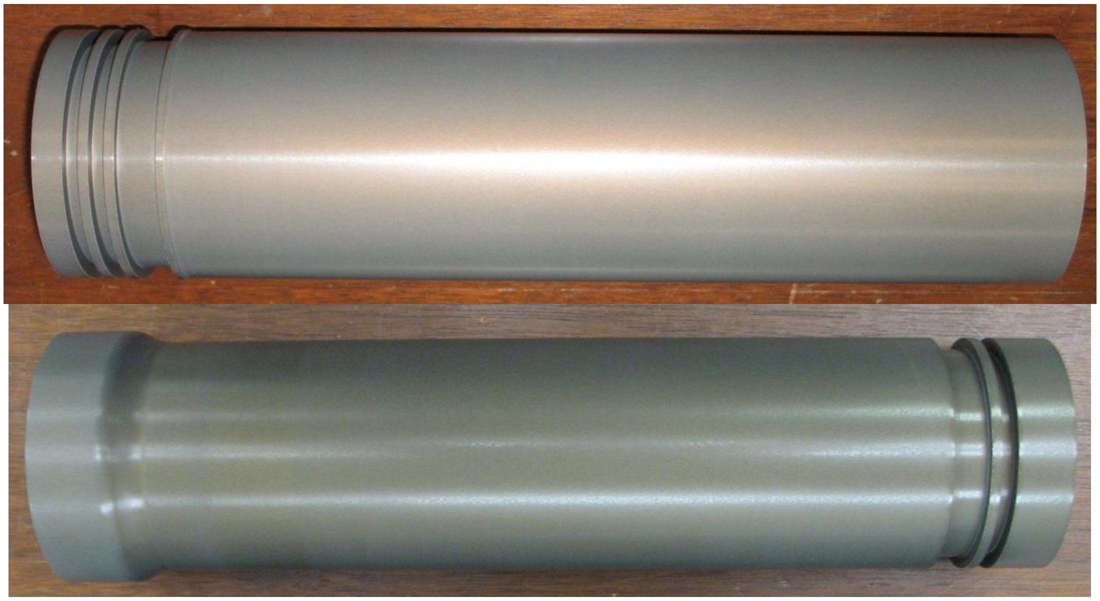

Figure 22: Photo of redesigned piston ends

Table 2 shows calculated values of friction force from the original pistons, the half ring tests, and the new pistons with and without the rider rings. Friction force is shown for several velocities, both inward and outward. The calculated friction force was lower with the new pistons compared to the original pistons, but not as low as was seen with the cut rings. There seems to be some effect by removing the rider rings, but not enough to explain the discrepancy.

Table 2: Friction force comparison between different ring configurations

	Full rings		Half Rings		New Rings		New Rings no Rider	
He Pressure bar	Velocity m/sec	Force N	Velocity m/sec	Force N	Velocity m/sec	Force N	Velocity m/sec	Force N
75	13.0	-710	13.0	-342	13.1	-565	13.4	-516
	-12.1	812	-12.2	560	-12.1	754*	-12.7	666
	8.6	-640	9.2	-317	8.8	-381		
56	10.3	-728			10.6	-556	10.8	-515
	-9.0	749			-9.4	689*	-10.0	639
	5.6	-588			6.4	-372	7.1	-317

* Bounce chamber pressure was higher than other cases, so higher friction is expected

The new pistons were used for most of the combustion tests that will be described later in this report. Gapless bronze impregnated Teflon rings were used for the majority of these tests. However, a second ring material was investigated. Because the Teflon rings were failing rapidly and labor intensive to replace, gapped PEEK rings were investigated. The gapped design made them much easier to install and the PEEK seemed more robust than Teflon. However, the system was never successfully operated with these rings. Higher He pressure was required to get the piston motion started, piston synchronization often went unstable, and the longest duration tests were ~3 seconds. The reasons for poorer performance with the gapped PEEK rings are not completely clear. These rings seemed to produce higher friction, thus requiring higher starting pressure. Also, the rings seemed to be damaged as easily as the Teflon rings with small craters forming typically near the interlocking feature at the gap. These craters would quickly grow and create a leak path that could affect synchronization when leaks were worse for one piston compared to the other.

2.3. Combustion system

The combustion system for the FPLA was designed for homogenous charge compression ignition (HCCI) of a gaseous fuel, specifically hydrogen. Hydrogen was chosen as the initial fuel for this research system for several reasons: 1) Very short combustion time resulting in nearly constant volume heat addition, 2) Low emissions with only NOx a concern, and 3) interest by our DOE sponsors in hydrogen as a transportation fuel. The combustion system consists of fuel and air delivery subsystems, intake and exhaust manifolds, a water-cooled combustion cylinder, and the combustion ends of the pistons described in the previous section.

Lubricating oil was metered to the combustion chamber and each bounce chamber through small ports in the cylinder walls using a fixed volume delivery system. Figure 23: Lubrication oil distribution system shows the lubricant distribution system which is a Master Pneumatic SERV-OIL Automation Pac consisting of an oil reservoir, a controller, and 12 Servo-Meters. Each bounce chamber and each side of the combustion chamber have three oil ports. The pulse frequency is adjustable and oil volume supplied per pulse can be individually adjusted for each Servo-Meter for lubrication control. Oil supply to the combustion chamber was adjusted through a series of experiments so that combustion of lubricating oil would not produce falsely high thermal efficiency measurements. This included limiting the oil flow to two of the six combustion chamber ports.

Figure 23: Lubrication oil distribution system

Figure 24 shows the hydrogen supply system to the combustion chamber. Pressurized hydrogen is supplied to the lab from a standard DOT 1A cylinder that resides outside of the building. A manifold connects the cylinder to the lab supply line with a series of manual valves and solenoid control valve along with a regulator that drops the pressure to 500 psi. The solenoid valve is operated from inside the lab with a control switch. The solenoid is also connected to the lab safety system which closes the valve if a hydrogen leak is detected. The hydrogen line inside the lab runs to the regulator shown in Figure 24 which drops the pressure to 50 psig just upstream of the hydrogen flow meter. The flow meter, also shown in the figure, is a Sierra Smart-Trak 2 M100H. The flow meter was purchased with a primary standard NIST traceable calibration to an accuracy of 1% of full scale.

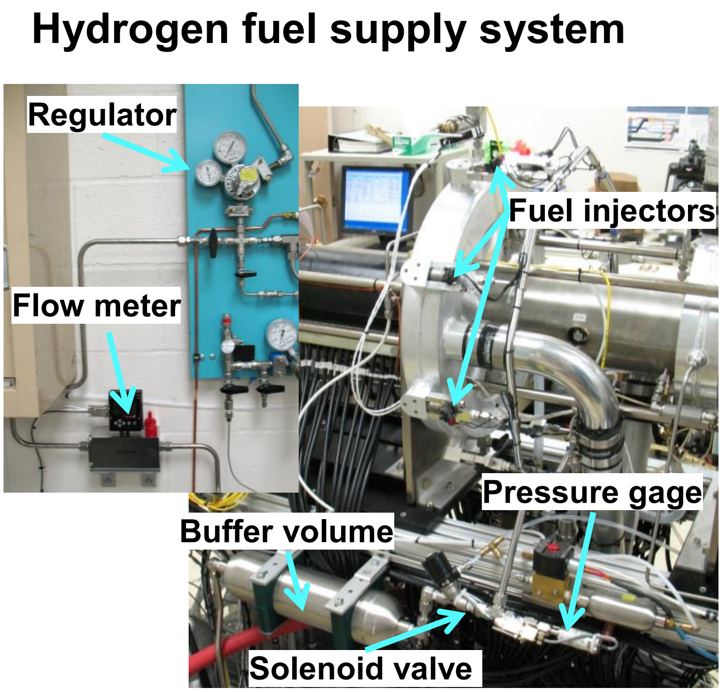
Hydrogen fuel supply system

Figure 24: Hydrogen supply system to the combustion chamber

Downstream of the flow meter, the hydrogen supply line runs to a buffer volume which is used to dampen any pressure fluctuations due to the opening and closing of fuel injectors. As the figure shows, next in line is a solenoid control valve. This valve is used to allow hydrogen to the fuel injector manifold and is connected to the FPLA safety system as will be discussed in a later section. A pressure gage is attached to the manifold to monitor the pressure just upstream of the fuel injectors.

A set of five commercially available gaseous port fuel injectors (Quantum Technologies PQ2-3200) are used to obtained the required fueling rate. Hydrogen is supplied to the injectors at 50psig. Testing of the fuel injectors was performed to determine the mass of fuel injected per pulse as a function of pulse width at this pressure, which guided controller development. This testing was described in a separate report [23]. Figure 25 shows the test apparatus used to test the fuel injectors which used the hydrogen flow meter along with a calibrated volume for pressure accumulation flow measurements. The two measurement methods generally agreed to within 2.5%. A close-up view of a fuel injector and a sample of the data produced are also shown in the figure.

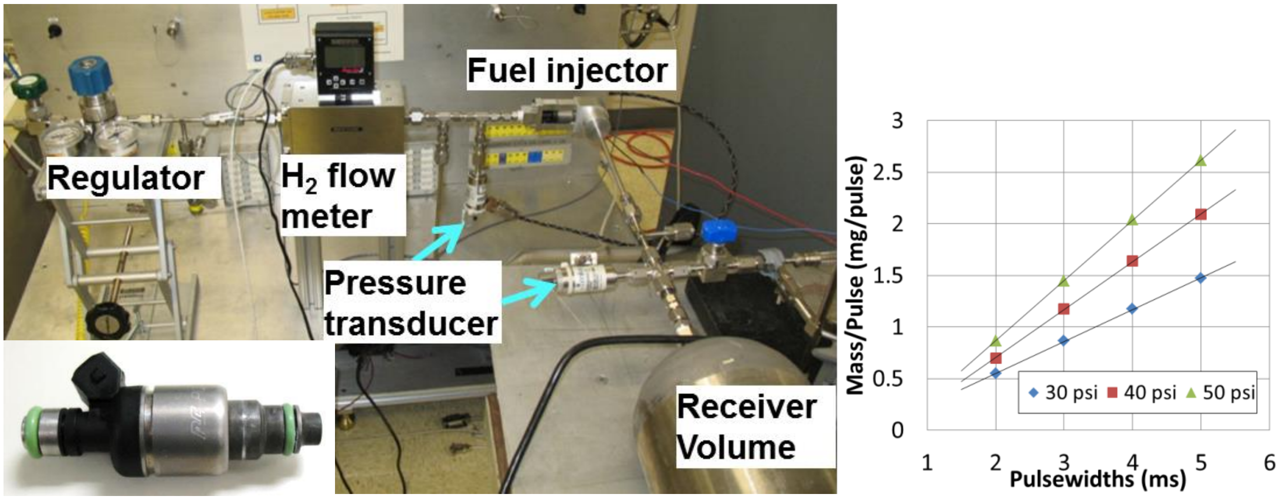

Figure 25: Fuel injector test apparatus (left) and example data (right)

The hydrogen fuel injectors were fired once per cycle, triggered by piston position. A combination of pulsewidths and number of fuel injectors was used to control the amount of hydrogen injected per cycle. The hydrogen was injected into the intake manifold which surrounds the combustion chamber intake ports. Air flow to this manifold was provided by a Republic HRB-1202 two-stage regenerative blower. A 2½" schedule 40 pipe coming from the blower was split into two 2½" OD tubes and connected to two 2¼" ID tube stems welded on the manifold. During typical operation the manifold pressure rose to approximately 24 psia while the intake ports were closed, and the air flow rate was between 125 and 150 cfm depending on the FPLA operating frequency.

CFD modeling had been performed to determine the intake port and manifold geometry needed to obtain plug flow for optimal scavenging and charge mixing. This modeling effort was described in [21]. Based on the results, the intake manifold was designed to provide stratified, uniflow scavenging. The modeling results suggested that this approach could achieve high scavenging efficiency with minimal short circuiting as well as adequate mixing for high combustion efficiency.

The water cooled combustion chamber is shown in Figure 26. The combustion chamber bore is 3.195" with exhaust port opening/closing at 7.482" from the center plane, giving a trapped volume of 1.97L assuming ideal piston synchronization. The intake ports open later at 7.875" from the center plane, allowing time for residual cylinder pressure to blow down through the exhaust. The cylinder was made from AISI 4340 steel hardened to Rockwell C 38-40. In addition to the gas flow ports, the cylinder has four instrumentation ports spaced at 90 degrees around the chamber circumference at the midpoint. Two of these ports are used for pressure transducers while the other two are unused. Finally, as previously mentioned, the chamber has six lubrication ports, three on each side of the midpoint.

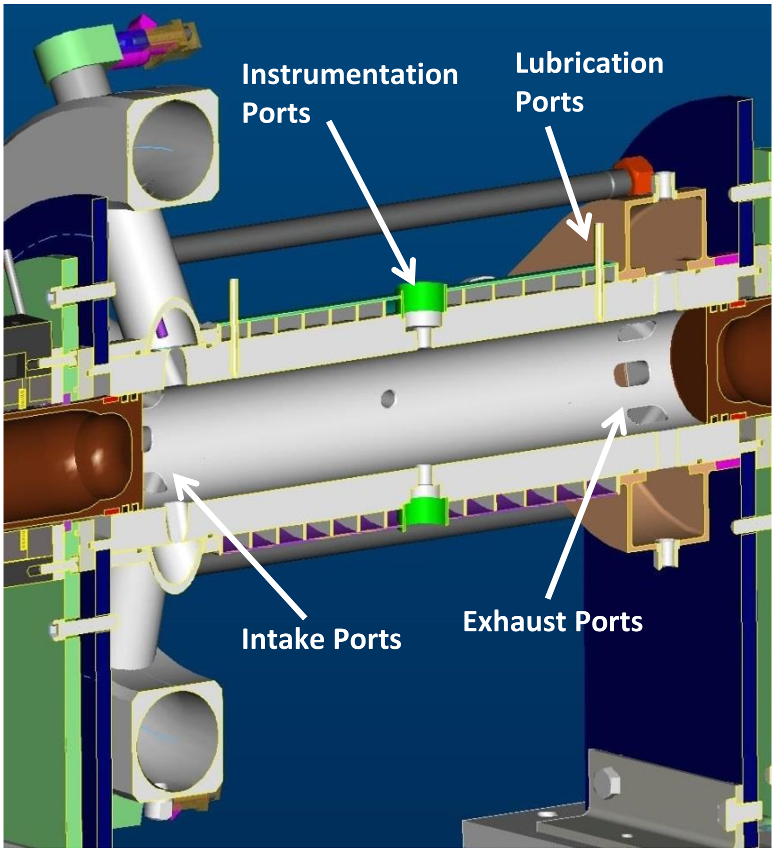

Figure 26: Cross-section of the combustion chamber

2.4. Linear alternator

One either side of the combustion chamber are the linear alternators. These units were designed and fabricated by Magnequench Technology Center of Research Triangle Park, North Carolina. A schematic of one of the alternators is shown in Figure 27. The maximum mover stroke is 200mm and the mover-stator air gap is 1 mm. The stator body is comprised of an array of 14 coil-and-bonded-iron-core units and the pole pitch is 22 mm. Each coil consists of 14 turns of 4.064 x 0.762mm square magnet wire. The coil resistances and inductances are approximately 0.0245Ω, and 165μH, respectively.

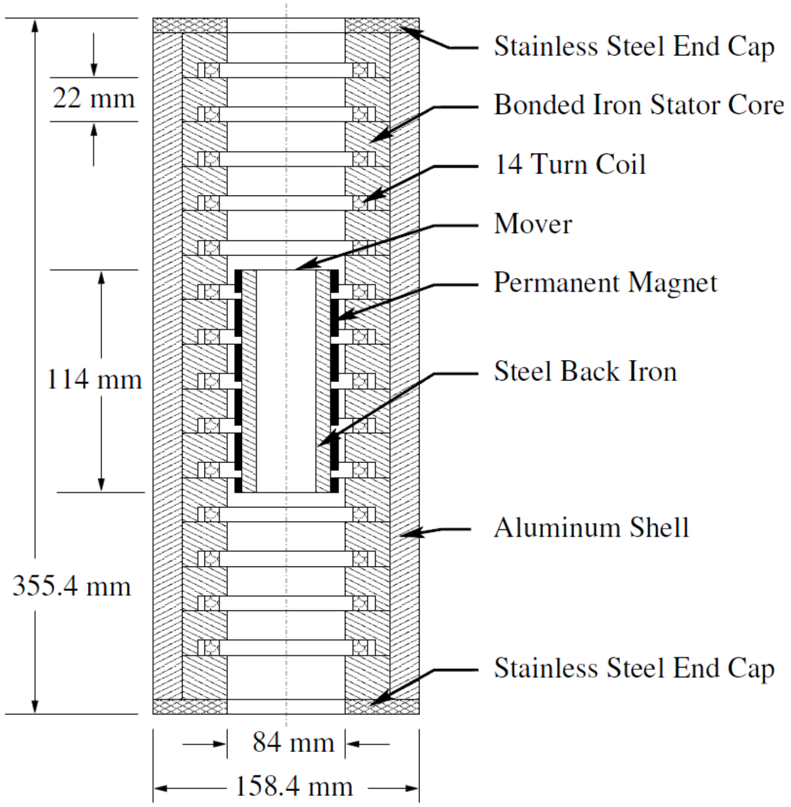

Figure 27: Schematic of the Magnequench linear alternator

Each mover consists of two, 10 mm wide and four, 20 mm wide Daido ND-39R radially-magnetized neodymium-iron-boron permanent magnets, five 2 mm wide aluminum spacer rings, and an annular backiron made of low carbon steel. The magnets are 81mm outer diameter by 73mm inner diameter and are arranged in alternating polarity and generate five toroidal magnetic fields. Consequently voltages are induced in five coils simultaneously when the mover is in motion. As shown in Figure 20, the mover is attached between the two piston ends by threaded ends. Figure 28 shows one of the backirons before the magnets are attached.

Figure 28: Backiron for the permanent magnets. Threaded ends attach to the piston ends.

Figure 29 shows the system used to bond the magnets and aluminum spacers to the backirons. Prior to assembly, the epoxy coating was removed from the inner diameter of the magnets, and all parts were cleaned with acetone. Loctite 7649 primer was applied to all mating surfaces. The magnets and spacers were then assembled onto the backiron using a tapered aluminum part to guide the magnets safely onto the steel. An adhesive delivery manifold was then installed onto the aluminum guide and clamped in place. Small vessels filled with Loctite 640 adhesive were installed on the delivery manifold, and compressed air at 100 psig was applied at the top.

As Figure 30 shows, adhesive is ported to a groove around the inner circumference of the manifold allowing it to spread around the full diameter. O-ring seals block all flow paths except the gap between the magnets and backiron. Slits on the bottom face of the lowest magnet spacer allow gas to escape as the adhesive is extruded through the gap. Once adhesive was seen flowing from all slits, the compressed air was removed and the slits were plugged to retain the adhesive. The complete assembly was cured in an oven for 24 hours at 50°C, this temperature being low enough to avoid permanent flux loss in the magnets. A mockup assembly bonded in this manner showed good adhesive coverage and shear strength upon dissection.

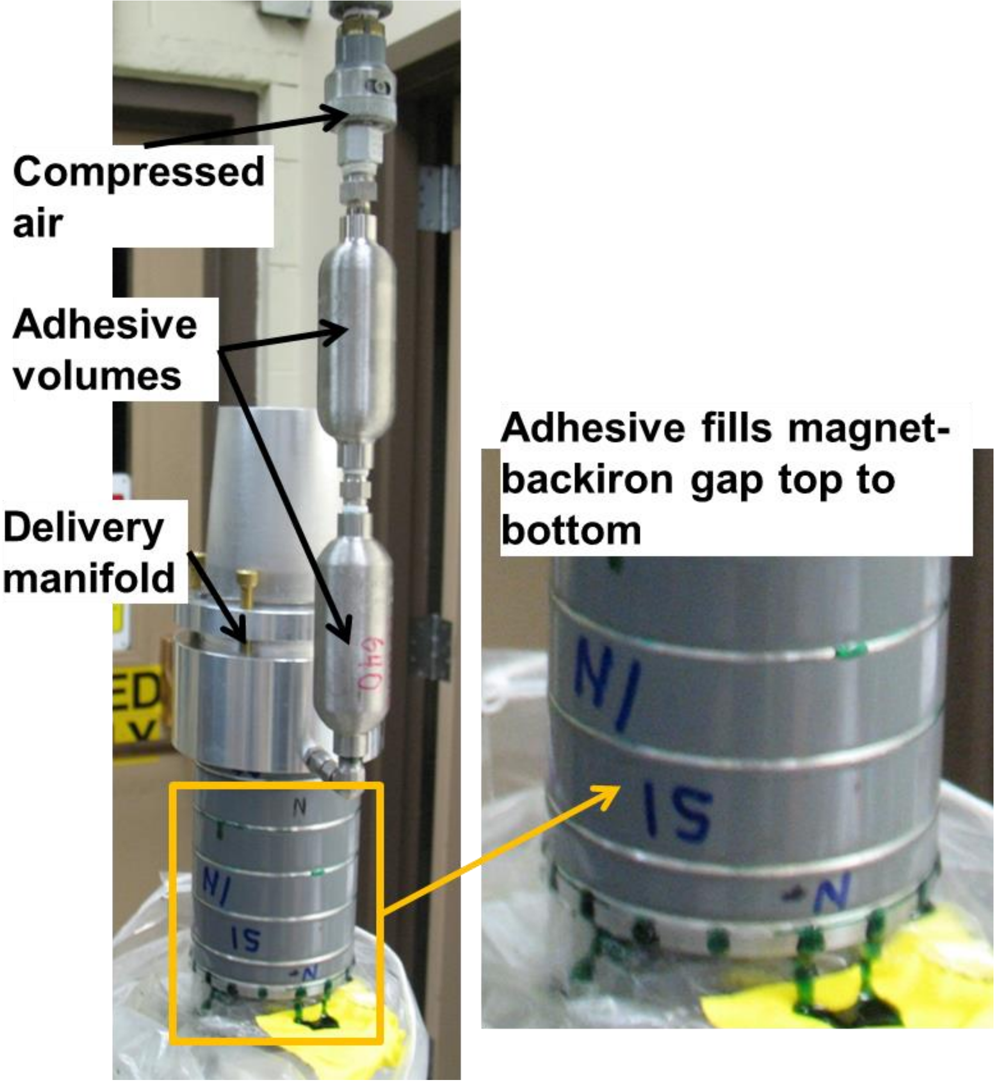

Figure 29: System used to attach magnets to the backirons

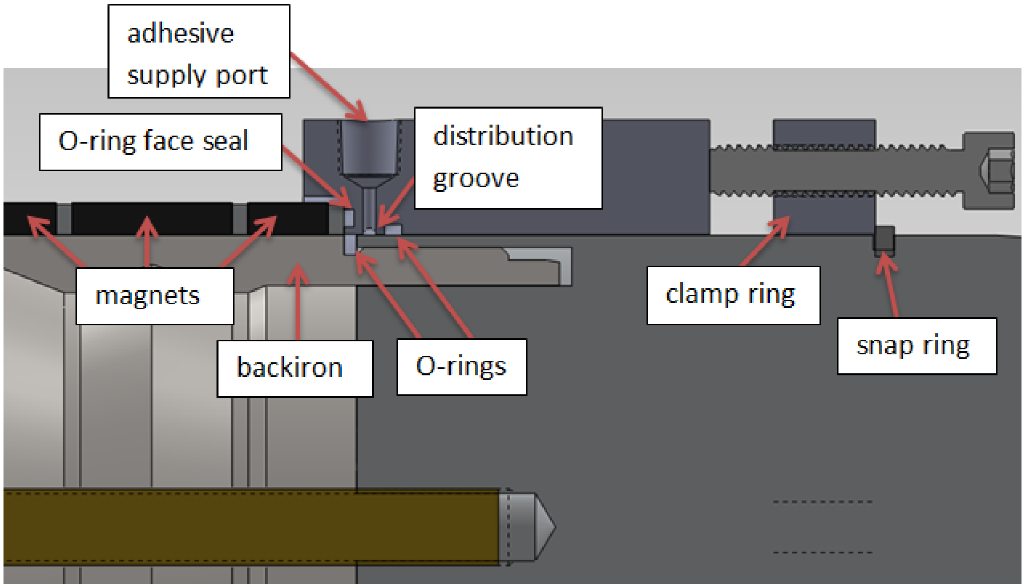

Figure 30: Adhesive distribution manifold

The mirror image coil pairs of the alternator stators, one on the left side and one on the right side, are connected in parallel and the electricity generated is dissipated directly through a bank of 14 water cooled load resistors. Riedon FHR2P-0R182F1 precision power shunt resistors were used, having a resistance of 0.182Ω with 1% tolerance. Modeling of the alternators indicated that electrical power generation peaked near this resistance value. Each resistor is rated for 2kW continuous dissipation with proper heat sinks. The resistors were stacked between 15 Aavid Thermalloy 416601U00000G liquid cold plates with thermally conductive pads ensuring good contact. However, several resistors failed during the course of testing. The center coils can get fairly close to the resistor power limit, but the failures could also be related to the high instantaneous power seen with this intermittent waveform. For simplicity, they were replaced with identical units, though a higher power rating would be required for better longevity.

Connecting the mirror image coils in parallel provides a means of synchronizing the left and right side pistons through the electromagnetic forces. As one mover takes a lead over the other, the inductive coupling of their circuits places a greater electro-mechanical load on the leading mover, compared to the lagging one. Hence, the movers are drawn together in relative position. This passive synchronization was a key performance characteristic that was to be demonstrated during the FPLA project and will be discussed in more detail later.

2.5. Bounce chambers

As shown in Figure 18, at each end of the FPLA are the bounce chamber cylinders. These cylinders house the bounce ends of the pistons and are made of hardened 4340 steel with a bore of 2.900”. A set of vent ports are machined into one end of the chambers and are activated when the pistons near TDC. An instrumentation port is used to measure the bounce chamber pressure and each cylinder has three lubrication ports. At the opposite end of the bounce cylinders, the He start system and air drive system are attached. Each of these systems will be described in more detail in later sections.

2.6. Cylinder alignment

The engine was designed with locating features to ensure concentricity of the cylinders upon assembly, but with such a long assembly, alignment was still a concern. A procedure was developed using bore targets and an alignment telescope to align the bounce chamber cylinders to the combustion chamber cylinder during assembly. Close fitting target holders were machined to match the cylinder bores and mounted to a hollow shaft for ease of installation, removal, and clocking of targets (Figure 31). As shown in Figure 32, two targets were first installed in the combustion chamber bore, and the alignment telescope, rigidly mounted to the frame of the experiment, was adjusted to be on axis. The combustion chamber targets were then removed, and the piston was installed through the stator into the combustion chamber cylinder. The piston was pushed to near the center plane, so that once the bounce chamber cylinder was installed, there would be room for targets in the bore. At this point, the bounce chamber was adjusted as needed to position its axis in line with the telescope. The procedure was repeated for the opposite bounce chamber, and engine assembly was finished.

Figure 31: Optical alignment fixtures

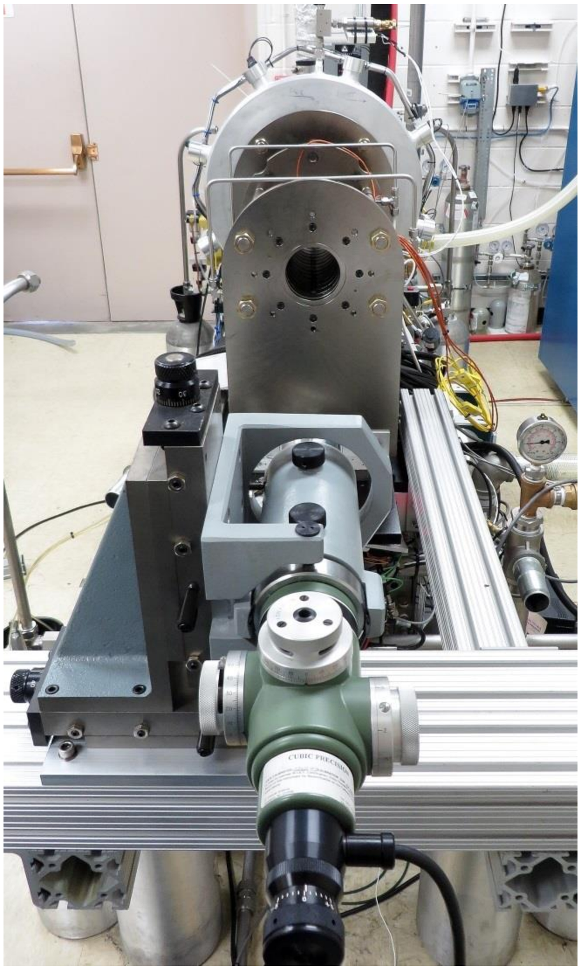

Figure 32: Alignment telescope used to align the combustion and bounce chamber cylinders

2.7. Pneumatic dynamometer

In principle, electrical energy generated during the expansion stroke could be stored and utilized to power the following compression stroke. This approach would require a large linear alternator relative to the net electrical output, particularly for the desired high compression ratios. In the chosen configuration, the linear alternators are designed based on the desired net electrical output and augmented with bounce chambers as a means of energy storage. Thus, the linear alternators alone cannot provide sufficient power to reach the range of desired compression ratios in a single stroke. Note that starting could still be accomplished using the linear alternators, though it would take multiple cycles to build up enough energy in the bounce chambers to reach an ignitable compression ratio. For operation as a research engine, it was desired to be able to motor the engine at a chosen operating condition prior to introduction of fuel. Rather than relying on the linear alternators, a pneumatic system was devised to inject compressed air into the bounce chambers when the pistons near BDC and vent it to a controlled pressure near TDC. In this configuration, the compression ratio of the combustion chamber is set by controlling the air injection pressure in the bounce chambers. Similarly, the extent of piston travel into the bounce chambers is adjusted by controlling the vent pressure.

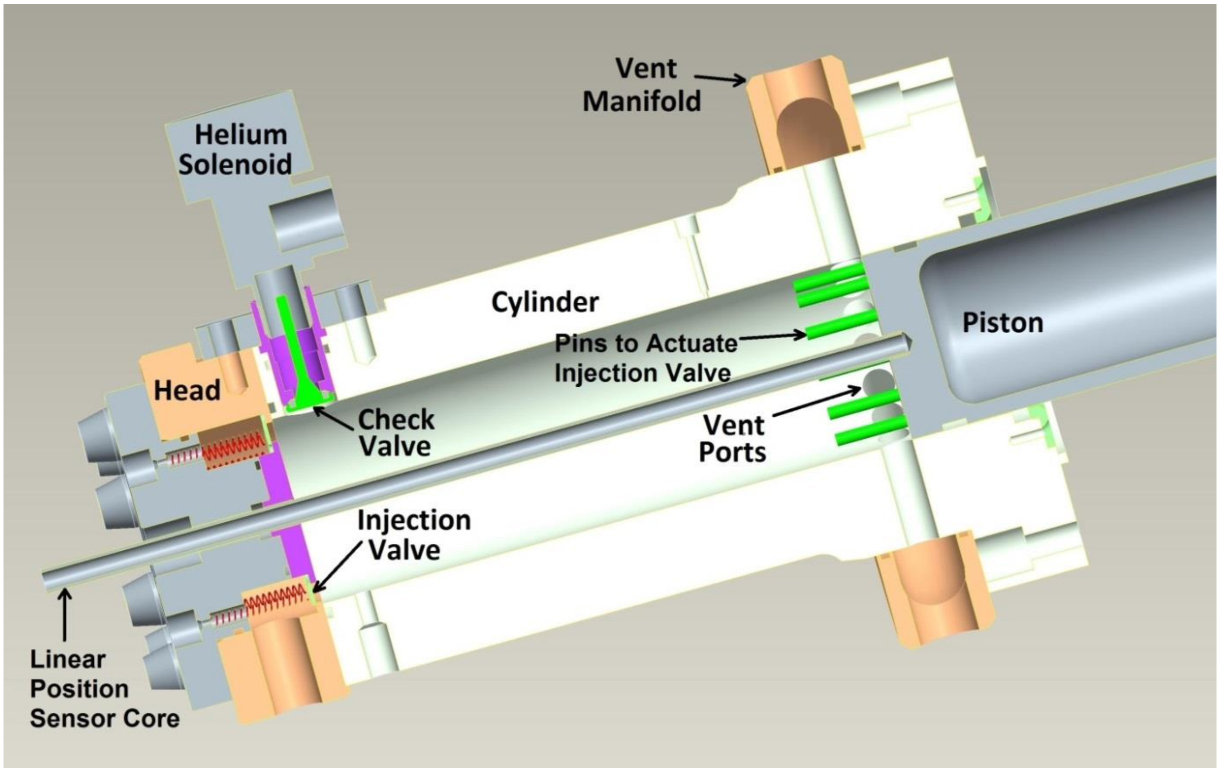

Figure 33: Cross-section of a bounce chamber cylinder showing the pneumatic drive system

A schematic of the bounce chamber pneumatic drive system is shown in Figure 33. As the piston nears BDC, the air injection valve is actuated by a set of 12 pins threaded into the piston top. The valve uses an annular valve plate that seals on thin rings against a mating nose at the ID and outer head at the OD. A set of 16 compression springs is used to close the valve when there is minimal pressure differential across it, though the pressure differential provides the main seating force. The annular volume behind the valve plate is fed from the air drive supply system with air or N_2 at pressures up to 1200 psi. The momentum of the piston provides the force to open the valve. Pressurized air or N2 then enters the bounce chamber while the piston slows to BDC and then accelerates in the opposite direction closing the valve again. The P-V work of the gas drives the pistons back to TDC to achieve a desired compression ratio. As the pistons approach TDC the bounce chamber vent ports open and the gas vents to atmosphere through a vent manifold with a computer controlled butterfly valve to set the vent pressure. A picture of the inner and outer head assemblies is shown in Figure 34.

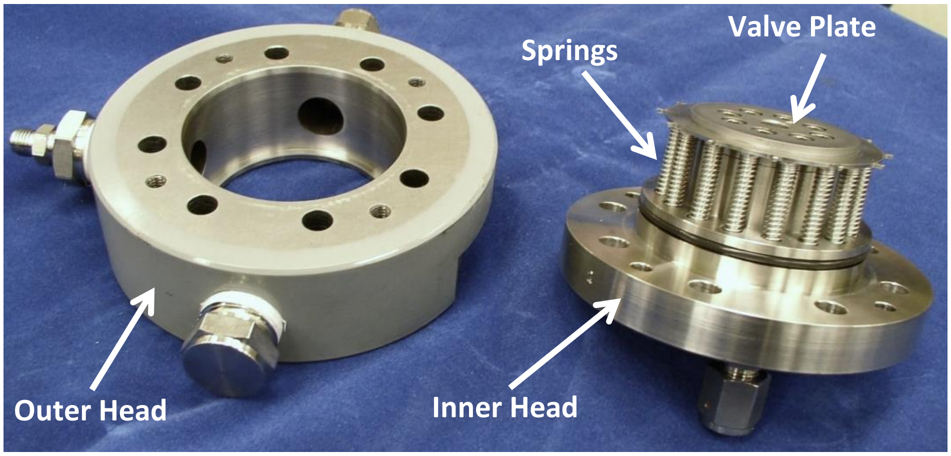

Figure 34: Photo of the inner and outer bounce chamber head assemblies

To fill the bounce chambers in the small amount of time near BDC requires valves with large flow area capable of operating under a significant pressure differential with quick actuation. Total time available to open, fill the cylinder, and close is on the order of 5ms. An annular valve mechanically actuated by the piston was designed to meet these constraints. The valve uses an annular valve plate that seals on thin rings against a mating nose at the ID and outer head at the OD. Teeth on both the ID and OD keep the plate concentric on the mating parts, and the space between teeth provides the path for gas flow. Shimming between the outer head and inner head provides a means of making the outer and inner sealing surfaces coplanar. Flatness of the valve plate then ensures a good seal.

The original valve actuation pins were 3/16” diameter and would indent the piston surface and loosen due to the high force and impact associated with opening the valve plate. Moving to ¼” diameter was sufficient to resolve the indentation issue, though they were still prone to loosening. Use of Loctite 262 permanent strength threadlocker was sufficient to keep them in place for the purposes of these experiments.

Prior to implementation with air motoring experiments, it was recognized that the valve closing springs would not remain in place under repeated actuation and the high air flow rate moving past them. Due to the long unsupported length, the springs were prone to buckling and being blown around as the valve was actuated. To remedy the problem without major design changes, spring retaining parts were designed. To maintain the full length of valve travel, a new inner head was made with increased depth, as seen in Figure 35. Base parts were pressed into the inner head, reamed for a sliding fit over the shaft of the caps. This approach worked well enough to obtain initial data. However, it became clear that the springs were being pushed beyond their limit. Springs were often found broken after longer tests.

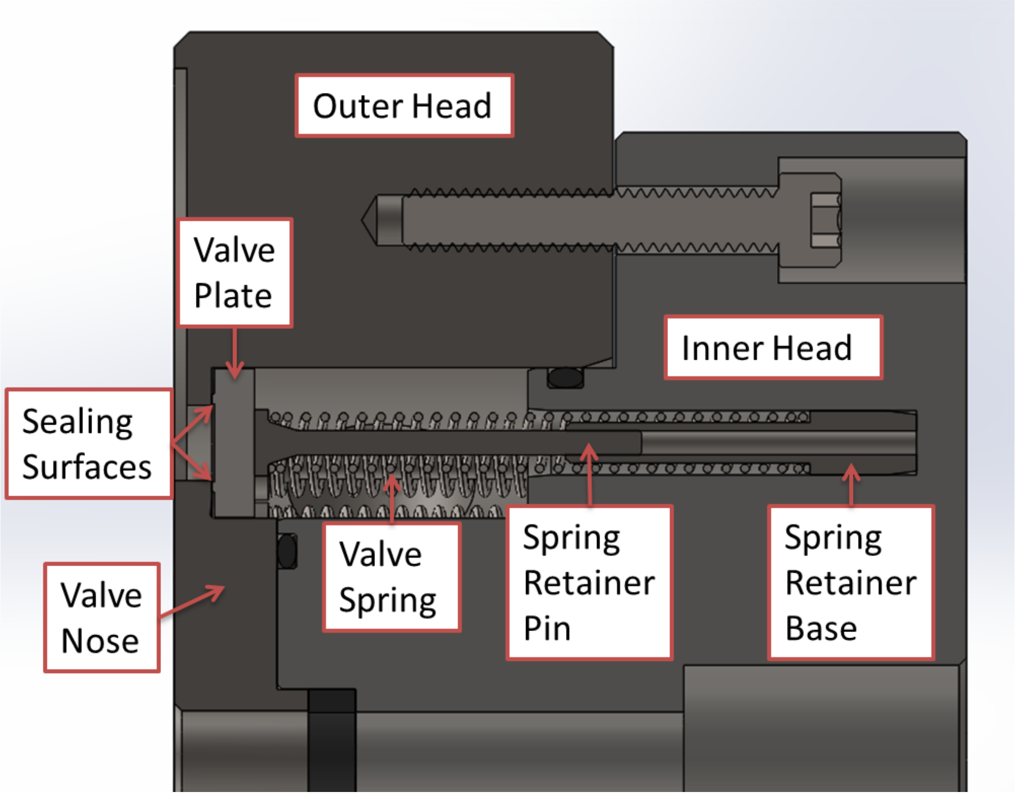

Figure 35: First bounce chamber head redesign

Longer springs were needed in order to handle the nearly 1-inch travel of the valve. To keep the spring rate up, larger diameter springs were needed. Chrome silicon steel die springs were chosen for their resiliency in applications with high cyclic loading. To install longer springs, the spring bores were machined through the back of the head, and a cap was installed to seal the head pressure and hold the springs in place, as seen in Figure 36. This configuration allowed easy access to the springs for installation, inspection, and replacement.

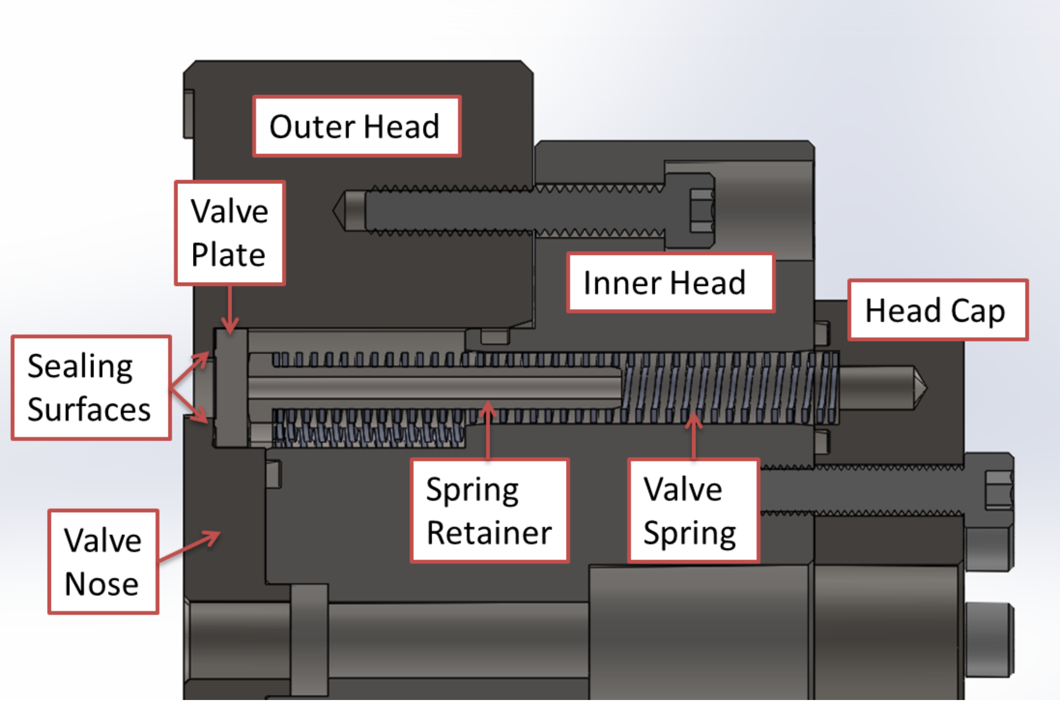

Figure 36: Second bounce chamber head redesign

The method of spring retention was also modified in this design. The small diameter pin used in the previous design was prone to fatigue failure under the impact of opening the valve. Additionally, in cases of piston overtravel, gas compression in the sliding mechanism was sufficient to overcome the press fit and push the base parts up from their seat. In the new design, a close fitting pin and bore are used to keep the spring in place. With the valve closed, there is sufficient engagement of the pin and bore such that the spring can hold itself on axis with the bore. The spring pins were made of hollow Ti-6Al-4V titanium alloy for strength and low mass. Being significantly larger than with the previous configuration, if these parts were made of solid steel, valve response would have been slower despite the higher spring rate. Through the use of hollow titanium alloy, the natural frequency of the spring-retainer-plate system was increased compared with the previous design. This not only ensured quick valve response, but reduced the likelihood of resonance in the springs.

Proper sealing of the valves required several design modifications which are summarized in Table 3 and Figure 37: Valve plate design parameters. The initial valve plate design was 0.050" thick made of grade 304 stainless steel. This design plastically deformed under the force and impact of the pistons. Subsequent designs included changing materials and thicknesses to achieve a lighter, stiffer and more impact resistant design. In addition, radial tolerances between teeth and mating surfaces were tightened to reduce slop and a tight flatness tolerance was added. To improve sealing by producing uniform contact stress on the sealing surfaces, raised sealing surfaces were added and surface finish was improved. In all, it took 6 revisions before the valve plates were robust enough to seal over many long duration tests with hundreds of cycles each. The final design, shown in Figure 38: Final valve plate design, was 0.170" thick 6-4 titanium with raised sealing surfaces, a flatness tolerance of 0.0002" and a surface finish of 8 micro-inches.

Table 3: Valve plate design modifications

Summary of valve plate revisions (all dimesions in inches)

rev.	a: tooth OD	b: tooth ID	c: annulus OD	d: annulus ID	e: thick	f: flatness	g: finish	material
A	3.115 +- 0.005	1.935 +- 0.005	2.875 +- 0.010	2.175 +- 0.010	0.050	0.0020	32	304 stainless steel
B	3.115 +- 0.005	1.935 +- 0.005	2.875 +- 0.010	2.175 +- 0.010	0.100	0.0020	32	annealed 4340 steel
C	3.119 +- 0.001	1.931 +- 0.001	2.915 +- 0.002	2.135 +- 0.002	0.100	0.0002	8	annealed 4340 steel
D	3.119 +- 0.001	1.931 +- 0.001	2.915 +- 0.002	2.135 +- 0.002	0.120	0.0002*	8*	annealed 4340 steel
E	3.119 +- 0.001	1.931 +- 0.001	2.915 +- 0.002	2.135 +- 0.002	0.170	0.0002*	8*	QC-10 aluminum
F	3.119 +- 0.001	1.931 +- 0.001	2.915 +- 0.002	2.135 +- 0.002	0.170	0.0002*	8*	Ti-6Al-4V titanium

* raised sealing surfaces added; dimension applies only to sealing surfaces

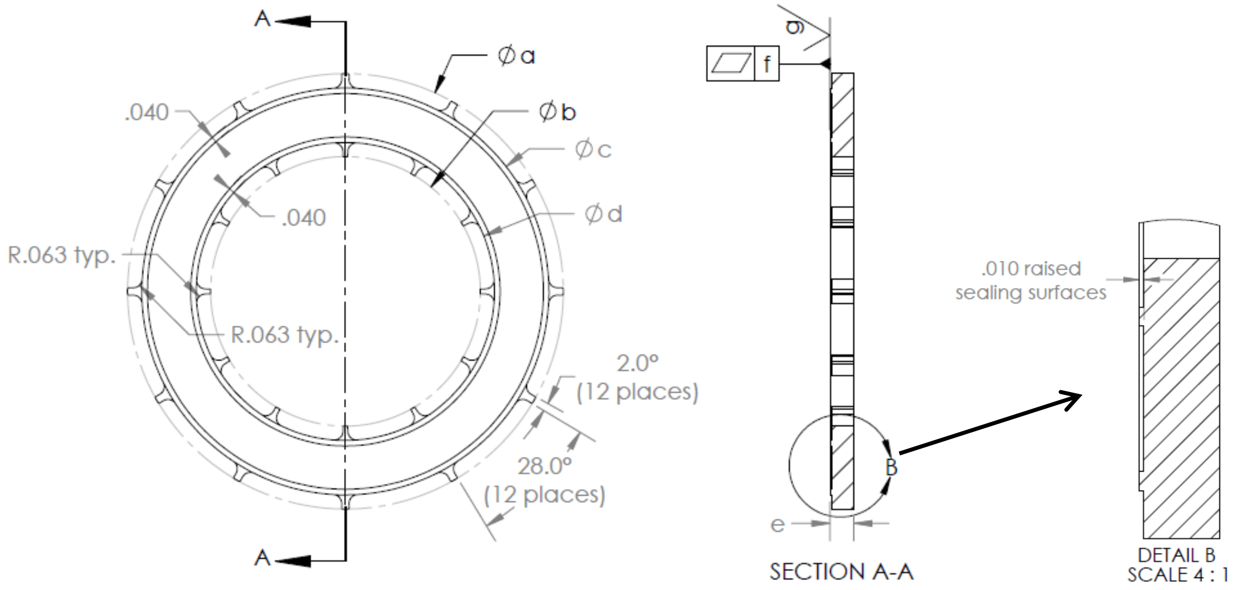

Figure 37: Valve plate design parameters

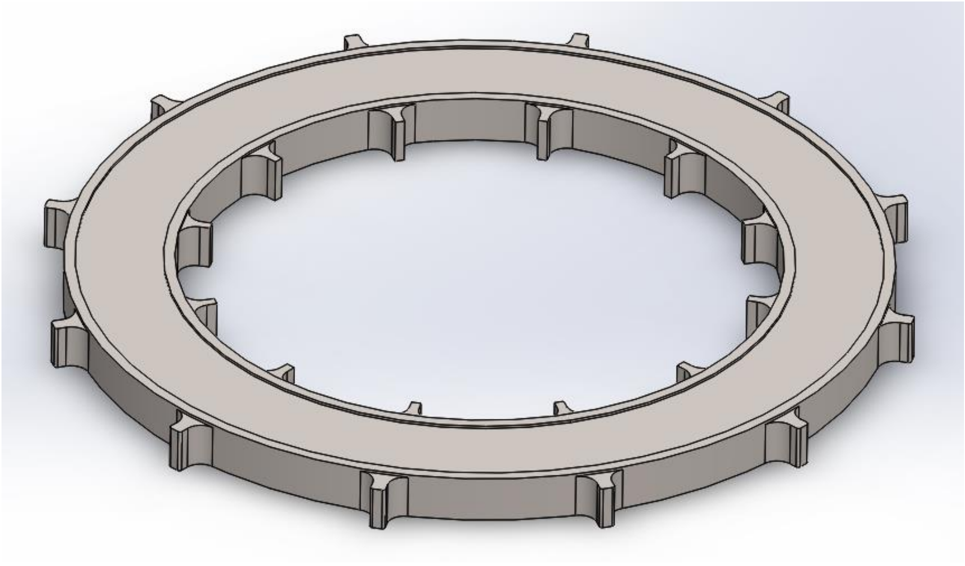

Figure 38: Final valve plate design

These final valve plates proved robust enough for the scope of our experiments, though the metal seats and valve plates were still susceptible to localized damage if debris found its way into the system. The head parts were re-lapped a few times as a result of debris including broken off bits of valve spring and particles of broken magnets. Lapping of the plate was a much more common occurrence. Due to the raised sealing edges, manual lapping against an optic flat using 400 to 1200 grit lapping compound produced good results in little time.

2.8. Bounce Chamber Vent System

To provide load control with the pneumatic system, the bounce chamber gas is vented to a controlled pressure, which determines the compression work absorbed on the outward stroke. Pressure control is accomplished by venting through manifolds and reinforced rubber tubing into buffer tanks, whose pressure is controlled using an electrically actuated butterfly valve operated with the computer interface.

Several modifications were made to the vent system to enable motoring, all aimed at getting more gas out of the bounce chambers to enable greater net energy input. Testing of the helium start system with the vent manifolds removed showed inadequate sizing of the bounce chamber vent ports, as atmospheric pressure could not be reached in the time the vent ports were open, even with all downstream plumbing removed. A thermodynamic model of the engine was adapted to determine the required port sizing for proper operation. It was determined that slotting the original ½” holes by ½” toward the outer end of the bounce chamber would provide adequate flow area. The modified vent ports are shown in Figure 39: Vent port modification to improve gas flow. Subsequent helium start tests showed good agreement with the model prediction.

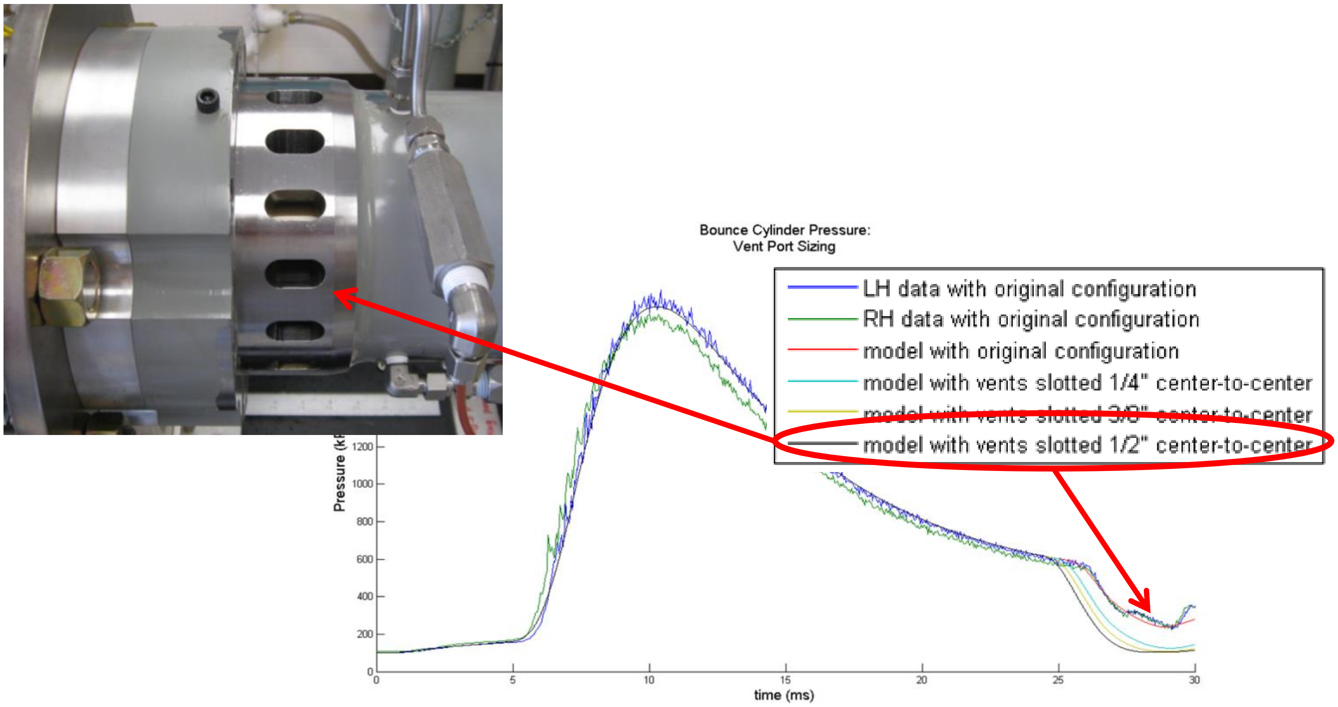

Figure 39: Vent port modification to improve gas flow

The next restriction evident was in the original vent manifolds, which contained too little volume and were restricted by four 3/4" NPT outlets. Modeling of the gas dynamics at bounce chamber venting indicated that a 2L manifold with four 1½" NPT fittings would bring the bounce chamber cylinder to near atmospheric pressure in the time available. New vent manifolds were designed and constructed to meet these specifications (Figure 40). Much of the downstream plumbing was also replaced to obtain a larger flow area and reduce the pressure drop as much as possible. The modified bounce chamber pneumatic drive system is shown in Figure 41.

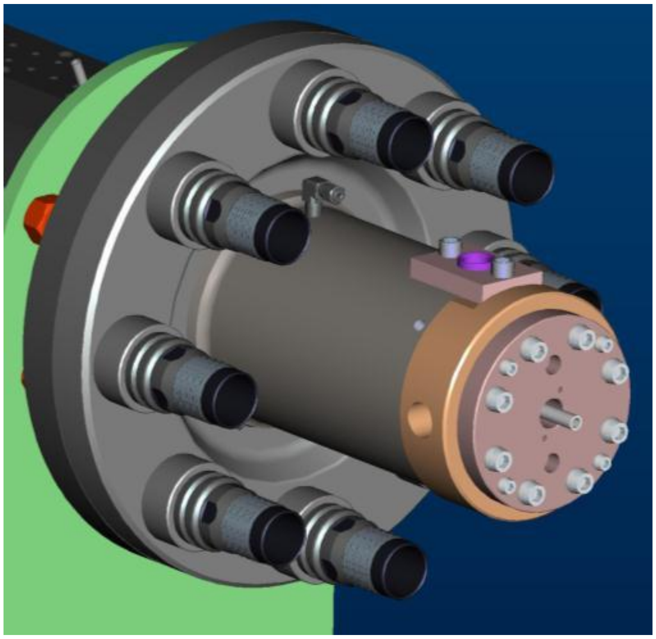

Figure 40: New vent manifold design

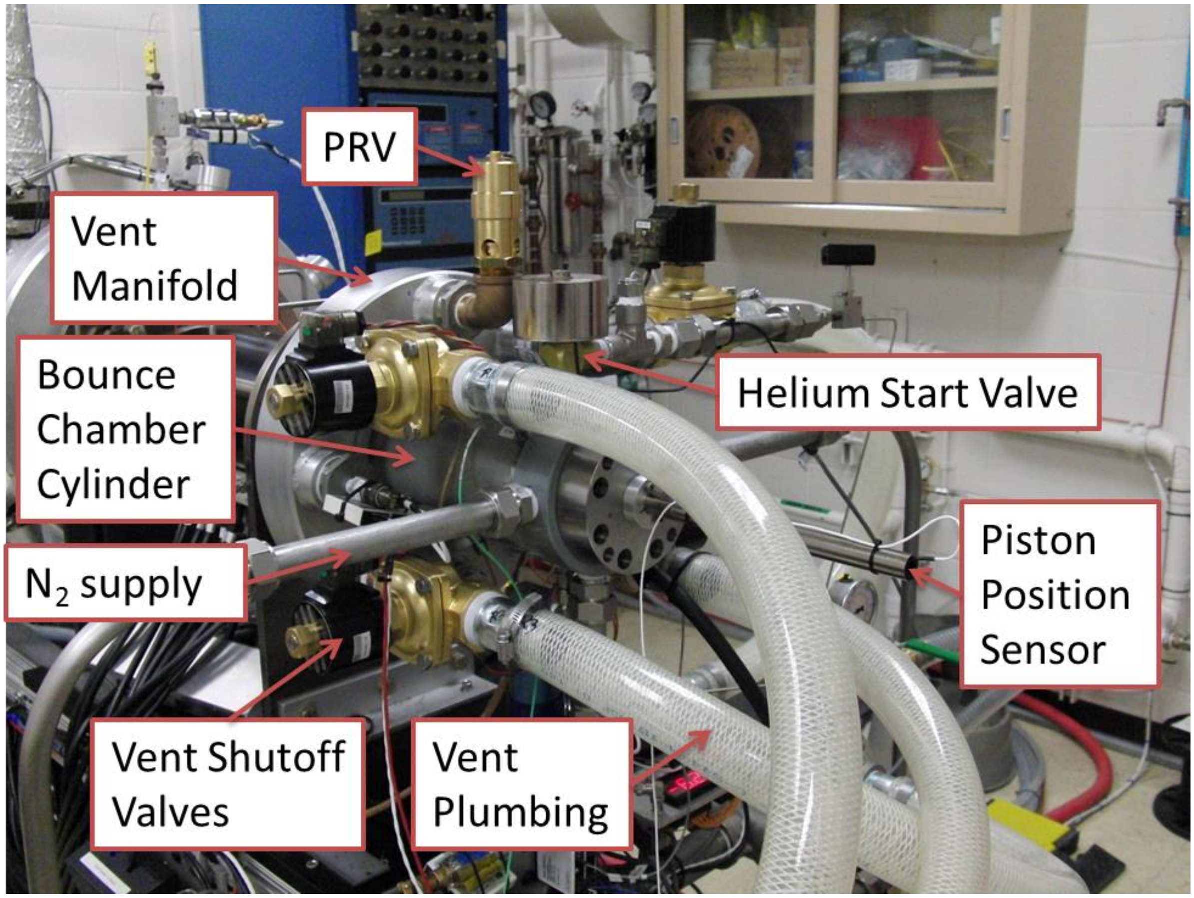

Figure 41: Modified bounce chamber venting system

2.9. Gas Supply System

Gas supply for the pneumatic dynamometer was originally intended to come from one or more air compressors operating at 1,000psig (Figure 42). The compressor outlet would feed into a 0-1000psig electronically controlled pressure regulator whose outlet fed into four 13.3L buffer tanks connected to the bounce chamber heads. Subsequent system modeling indicated that 1,000psig was barely adequate to motor the pistons, and that the flow rate required was three to four times that available from the existing compressor.

To meet this challenge, a gas supply system based on a 16-pack of size 1L nitrogen cylinders at 2,640psig (Figure 42) was assembled to meet the flow requirement, and the regulator was replaced with one rated for 0-1500psig. The compressor was left inline, but isolated from the nitrogen with a check valve and separate relief valve, allowing the buffer tanks to be filled with the compressor prior to beginning a test. An excess flow valve on the nitrogen supply allowed the large flow rate needed, but provided a reasonable upper limit to prevent overpressure of downstream components in the event of a regulator or component failure.

Figure 42: Pneumatic drive gas supply system. Air compressor (left) and N2 16-pack (right).

The N_2 system was able to supply enough gas to run the system for 10 minutes continuously at the highest expected flow rate. Since the experiments were mostly short duration (~1 min), 10 or more experiments could be run with each 16-pack of 1A cylinders. The 16-packs were easily changed with a fork lift and an extra one was always kept ready.

2.10. Helium Start System

In addition to the air drive system, a means of starting the piston motion was required that would enable the pistons to actuate the air injection valve plates. Therefore, a system was designed to start the pistons by injecting high pressure gas through solenoid valves in each bounce chamber. To get sufficient kinetic energy into the pistons, the bounce chamber cylinders must pressurize quickly, and to accomplish that with commercially available solenoid valves that would fit in the space available, helium was used as the working fluid. Note that helium is only used in the starting system. Thereafter, the mechanically actuated valves utilize compressed air or nitrogen. Figure 43 shows both the air drive supply to the bounce chamber heads and the He start system.

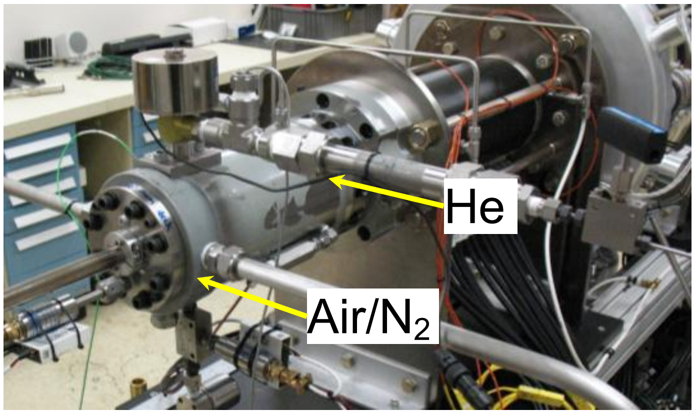

Figure 43: Photo of the gas supply to one of the bounce chambers

The He start system consists of a small vessel at high pressure upstream of each solenoid valve. In this way a controllable and repeatable energy input is enabled, requiring only that the two solenoid valves open simultaneously. The vessel blows down to near ambient as the cylinder vents, so the solenoid valve need not be capable of closing within the ~15ms half-cycle of the engine. The solenoid valves chosen were Circle Seal VR4177-ZHH, rated to 3600psig with valve coefficient of 2.7 and 24VDC continuous rated coils. The valves were operated at a nominal 60VDC to reduce the time required to ramp up current and minimize the effect of differences in coil inductance. Since they are only pulsed open for a short duration, the 24VDC thermal dissipation limit is not a concern. Additionally, two separate power supplies allowed adjustment of the voltage supplied to each valve, providing a means of compensating for any remaining differences.

Tests were conducted with one valve dumping to each side of a differential pressure transducer to initially set these voltages and confirm simultaneous opening. These voltages were adjusted as needed whenever differences in valve opening were noticed in the bounce chamber pressure record. Closing times, particularly when operating at the higher voltage, were too long for the valves to close within the half-cycle, so they are pulsed open for an arbitrary 40ms.

To accommodate leakage from the buffer tanks past the annular valve without pressurizing the cylinder and moving the pistons, a Circle Seal SV series valve is installed on each bounce chamber cylinder. These bleed valves are kept open whenever the engine is stopped, so that any leakage past the annular valves vents into the room. Just prior to opening the helium start solenoids, these valves are closed and kept closed while the engine is running.

A check valve is situated between the solenoid valve and the cylinder to prevent backflow of gas into the solenoid valve and upstream vessel as the cylinder compresses. The internal geometry was based on Circle Seal 2332R-4PP check valves, and the poppet assemblies were removed from stock valves for use in this application. The closing springs were prone to being blown out through the open valve due to the high flow rate, and a progression of stiffer springs was used until the problem was resolved. Century Spring S-271 was unaffected by the flow, and lasted hundreds of starts without any problems.

Figure 44 shows an example He start test with an initial He pressure of 138 bar. With this pressure the pistons are driven hard enough to achieve a significant compression ratio (47:1) and bounce back far enough to actuate the air drive valves by 0.3”. However, in these initial tests the pins attached to the pistons to contact and actuate the valve plate were removed. With no further energy input, the piston motion decays due to friction and electromagnetic drag forces. These initial He start tests showed that the bounce chamber vent system was inadequate to handle the pressure and flow rate required from the air drive system to motor the pistons. Thus, the vent manifolds and downstream plumbing were redesigned and replaced.

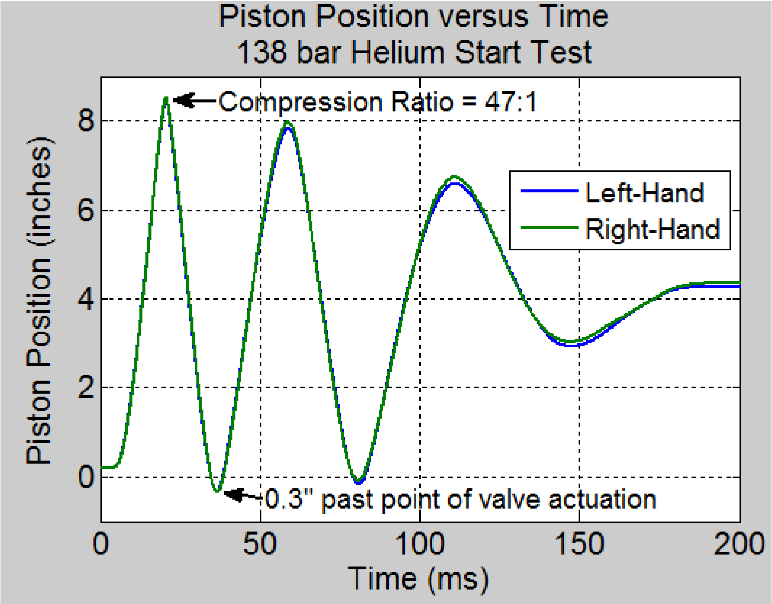

Figure 44: Example He start test

The use of helium presented some challenges for compression of the bounce chambers on the first several cycles. This is because the higher specific heat ratio of helium requires more energy for compression to a given volumetric compression ratio. This effect is demonstrated in Figure 45. The figure shows a log p - log V diagram for one of the bounce chambers for a He injection cycle along with one for air/N2 for comparison. The blue curve shows the helium injection, expansion, vent, and subsequent compression. Note that the helium compression curve is nonlinear at the start of compression. The starting reservoir cannot blow down completely within the short (~15 ms) expansion stroke, so gas from the reservoir is still flowing into the bounce chamber cylinder during the compression stroke until the cylinder compresses to a pressure above that of the reservoir. Also note that the slope of the He compression curve is much steeper than the green (air/N2) curve. This is the compressibility effect. With available compression energy limited by the kinetic energy in the pistons, the extra gas, combined with the higher compression work for helium, causes the pistons to turn around prior to actuating the annular valve. Then, without energy addition, piston motion decays rapidly due to electromagnetic and friction forces.

To mitigate this effect, the bounce chamber vent system was evacuated using a scroll pump (Figure 46) prior to each test. To isolate the vent system from atmosphere, a 2” pneumatically actuated ball valve situated downstream of the butterfly valve is closed prior to each test. As the engine is started, and the vent tanks begin to fill, this valve is opened to allow flow out of the vent tanks. With the vent system at vacuum, more of the helium can be removed from the cylinder while the ports are open, reducing the pressure at the start of the compression stroke and thus reducing the compression work required. This method was found to be sufficient to start the engine, but high helium injection pressure and first cycle compression ratio were required.

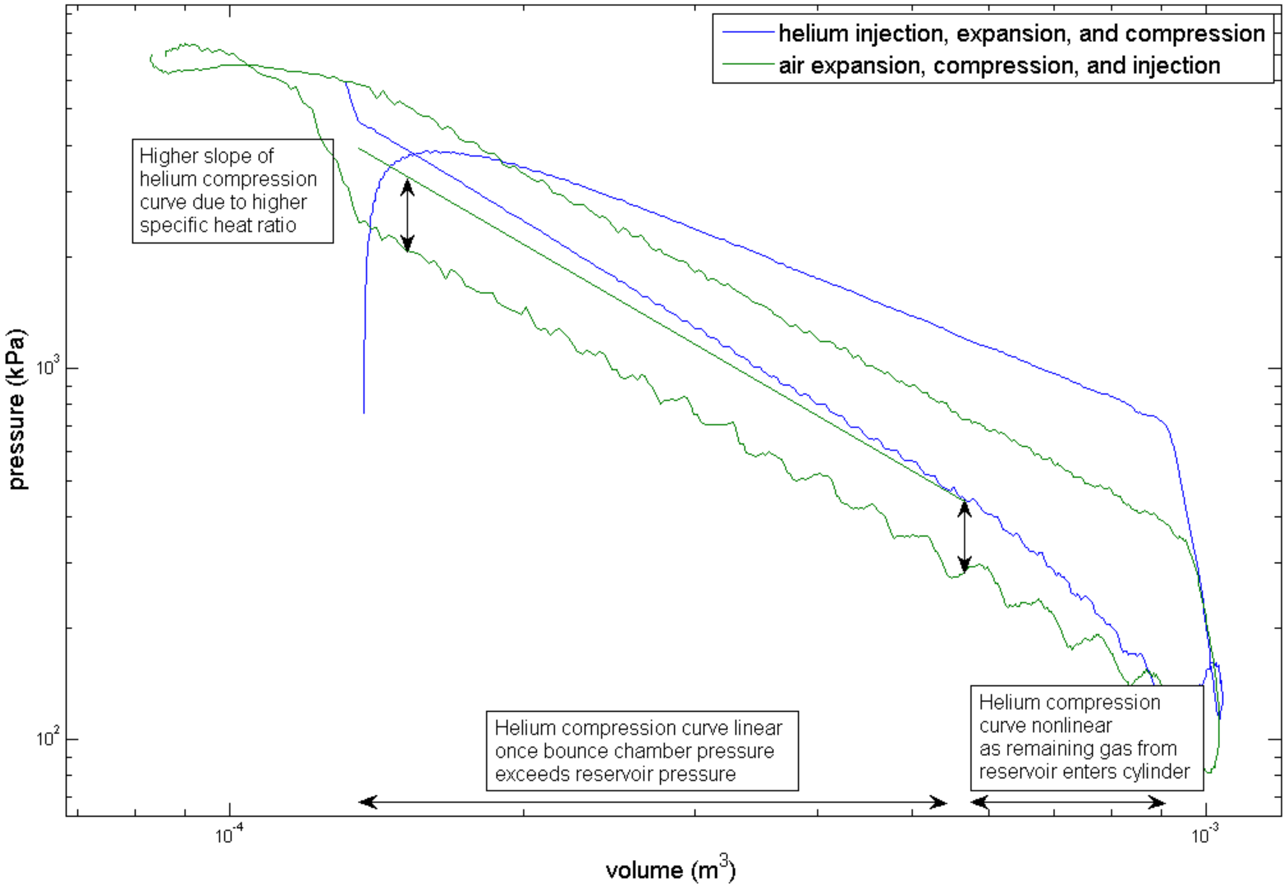

Figure 45: Effect of He on bounce chamber logP-logV

Figure 46: Scroll pump used to evacuate bounce chamber vent manifold prior to tests

2.11. Combustion-assisted Start System

To give more consistent starting and use less He at lower pressure, a system was devised to inject and burn fuel on the first cycle. Here, the helium injection pressure was much lower, adjusted only as high as needed to produce a compression ratio at which the H_2 would ignite. Figure 47 shows an example of this starting method. Firstly, a mixture of hydrogen and air is flowed through the cylinder just prior to the start of piston motion. The air blower is manually enabled at the beginning of every test, providing ~130 cfm of air flow through the combustion chamber. A pulse generator provides command signals to the fuel injector driver to achieve the desired fuel/air mixture. These pulses, shown in red in the figure, are enabled as the start switch is thrown, so fuel is only injected for roughly 200 ms prior to piston motion. As soon as piston motion is detected, the dummy injection pulses are switched off, leaving an appropriate fuel/air mixture in the combustion chamber as the piston motion closes the inlet and exhaust ports. The mixture is compressed and auto-ignited providing enough energy to drive the pistons far enough to actuate the pneumatic drive system while compressing the He remaining in the bounce chambers.

Subsequent cycles are then driven only by the pneumatic drive system as the He is exchanged for air/N2 while the vent manifold pressure transitions from vacuum to a steady-state value. If a combustion experiment is run, the injection pulses based on piston position are enabled. In the test data shown in Figure 47, piston-triggered fuel injection occurs after a 6-cycle delay. This delay is intentionally programmed into the control logic and will be described in a later section.

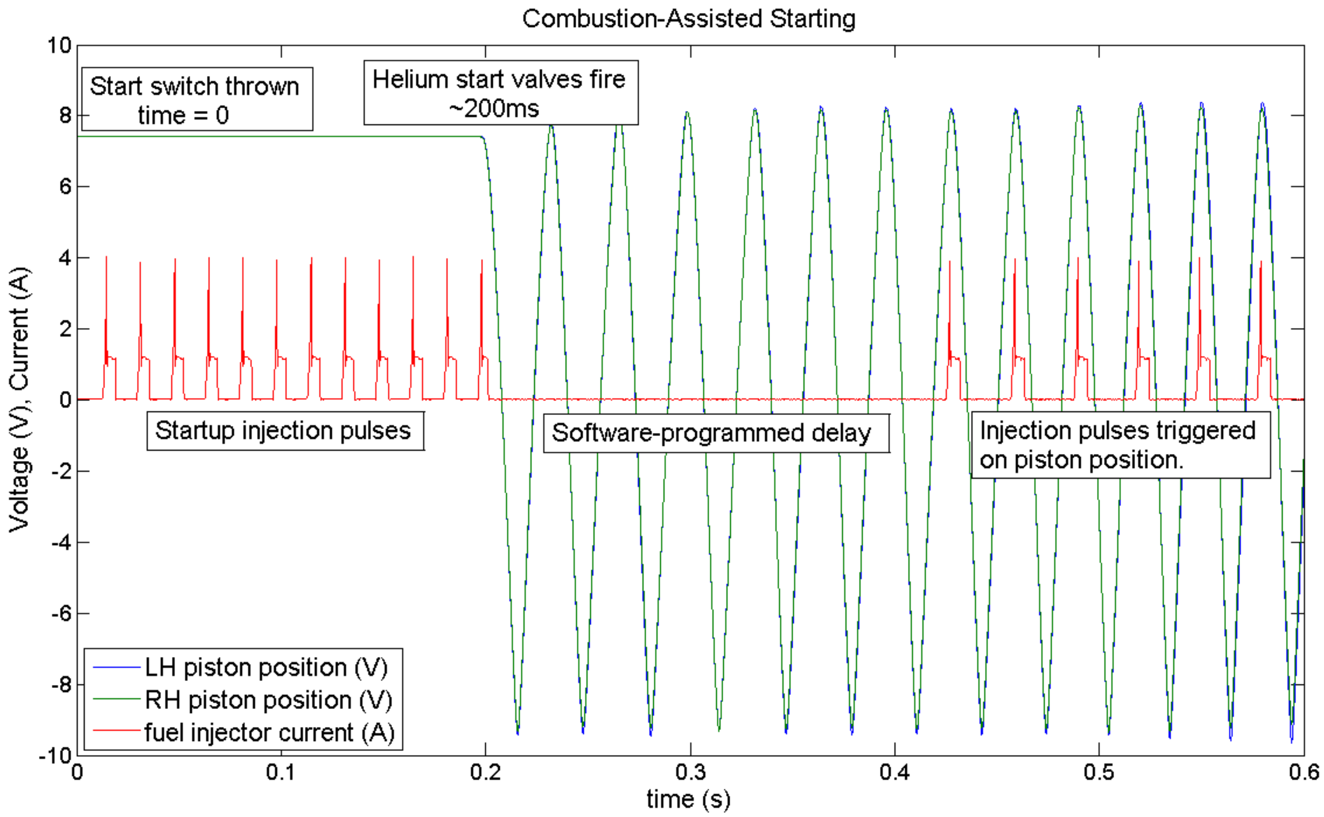

Figure 47: Example of the combustion-assisted start system

3. DATA ACQUISITION AND ANALYSIS

3.1. Piston Position Measurements and Corrections

Several types of diagnostic measurements were made to evaluate system performance and troubleshoot problems. Piston position measurements were made using Fastar FS5000HP variable inductor displacement sensors (Figure 48) and SP200A signal processors. The sensors were calibrated for a sensitivity of 2.00 V/in and the zero point set such that TDC corresponded to -9.50 V. As Figure 48 shows, the sensor bodies were mounted on the ends of the bounce chamber heads. The sensor cores were threaded into the end of each piston. It was found during initial testing that asynchronous piston motion where one piston traveled past the centerline of the engine would cause the sensor core to travel out of the sensor body. When the piston then reversed direction, if the core was not perfectly aligned with the body it would impact the bounce chamber head and be bent. Figure 49 shows an example of one such occurrence. To solve this issue, guide rods were fabricated that threaded into the sensor cores and were long enough that they could never travel out of the sensor body. These guide rods were made of G-10 Garolite, a tough glass epoxy composite which could handle the inertial force of accelerating and decelerating and would also not affect the sensor readings.

Figure 48: Piston position sensor

Figure 49: Damaged position sensor core due to piston over-travel

Care was taken to properly analyze the piston position readings and convert them to cylinder volumes. Due to the substantial acceleration near TDC, deflection of the position sensor core and the piston itself are non-negligible. Simulations were run in SolidWorks to calculate these deflections as a function of combustion chamber pressure. For the hollow position sensor rod accelerating its own mass in addition to the guide rod, the deflection was calculated as 0.21 mm at 300 bar combustion chamber pressure. This is equivalent to a 3.6 mm^3 difference in combustion chamber volume per bar of combustion chamber pressure.

Deflection of the piston assembly along its axis was simulated to account for deflection of the combustion piston top relative to the bounce piston top, where the position sensor core is attached. Deflection of the combustion piston top itself, becoming slightly concave with pressure, was also included in this calculation, though a smaller effect. The results showed that actual combustion chamber volume is higher than indicated by the position sensors by 12.1 mm^3 per bar of combustion chamber pressure. The total correction applied to calculate combustion chamber volume, accounting for both pistons, was thus 31.4 mm^3 per bar of combustion chamber pressure. For a motoring cycle with 30:1 compression ratio and 1.25 bar at port closure, this correction amounts to about 6% of the volume at TDC.

3.2. System Pressures

Combustion chamber pressure was measured by two redundant Kistler 6052CU20 piezoelectric transducers with 300 bar measuring range, conditioned with Kistler 5010 charge amplifiers. The measurement was referenced to absolute pressure in post-processing using the mean of the intake and exhaust plenum pressures during the time when both ports are open.

Bounce chamber pressures were measured with Kistler 6123 piezoelectric transducers with 250 bar measuring range, conditioned with Kistler 5004 charge amplifiers. These measurements were referenced to absolute pressure in post-processing during the time the vent ports were open using the Omega PX61C1-050GV flush diaphragm full bridge pressure transducers in each bounce chamber vent manifold.

Transducers and cables were cleaned with isopropyl alcohol and placed in an oven at 150°C for several hours to improve insulation resistance. For each piezoelectric transducer, the complete measurement chain (transducer, cable, charge amplifier, and data acquisition module) was calibrated at eight points within the operating pressure range using a Pressurements hydraulic deadweight tester.

Pressures were measured at several points in the pneumatic drive system using Teledyne Taber full bridge transducers with Dataforth SCM5B38-02 strain gage input modules for signal conditioning. Measurements were made upstream of the electronic regulator, in the high pressure accumulators, in each of the bounce chamber heads, and in the vent system accumulators.

3.3. Gas Flow Rates

Intake air flow was measured using a 15-250 scfm Omega FTB-939 turbine flowmeter with FLSC-61 signal conditioner. The flowmeter was positioned at the inlet of the intake blower to avoid the pulsing flow occurring closer to the engine, and installed with the recommended straight lengths upstream and downstream. Pressure and temperature were measured at the inlet of the flowmeter to obtain mass flow rate.

Fuel flow rate was measured using a Sierra Instruments Smart-Trak2 Model 100 thermal mass flow meter with 0.695 g/s hydrogen range. The meter was positioned upstream of a 2.25 L buffer volume supplying the injectors. Total response time of the plumbing and flowmeter to a step change in fueling rate was approximately 5 seconds.

3.4. Exhaust Gas Analysis

A sample stream of exhaust gas was pumped from the engine exhaust plenum to a set of emission analyzers using a Baldwin sample conditioning system with thermoelectric cooler for water removal. The gas analyzers and conditioning system are shown in their rackmount configuration on the right side in Figure 50. Span and zero gases were plumbed to the rack from bottles shown on the left side in Figure 50.

Prior to each test, flow rates to each analyzer were adjusted using metering valves to obtain the same values used in calibration. Exhaust oxygen content was measured with a Rosemount Analytical model 755R paramagnetic oxygen analyzer calibrated with a 21.0% span gas at 250 sccm. Exhaust NOx was measured using a Rosemount Analytical model 951A chemiluminescent detector calibrated with a 72.6 ppm span gas. Gas flow was adjusted to obtain 2.4 SLPM bypass flow with the sample backpressure regulator set to 4 psig. Vehicle emission zero air was supplied at 10 psig to the ozone generator. Exhaust CO and CO2 were monitored with two Rosemount Analytical model 880A non-dispersive infrared analyzers to ensure lubricating oil was not contributing to the combustion energy obtained. These were calibrated with 800 ppm CO and 4.5% CO2 span gases at 500 sccm.

For all emission analyzers, the zero point was calibrated using vehicle emission zero grade nitrogen at the same flow rates listed above. Response time for the emissions analysis equipment, primarily influenced by sample plumbing length, was around 30 seconds. Because of this substantial delay, it was difficult to obtain meaningful emissions measurements for tests that lasted less than 30 seconds.

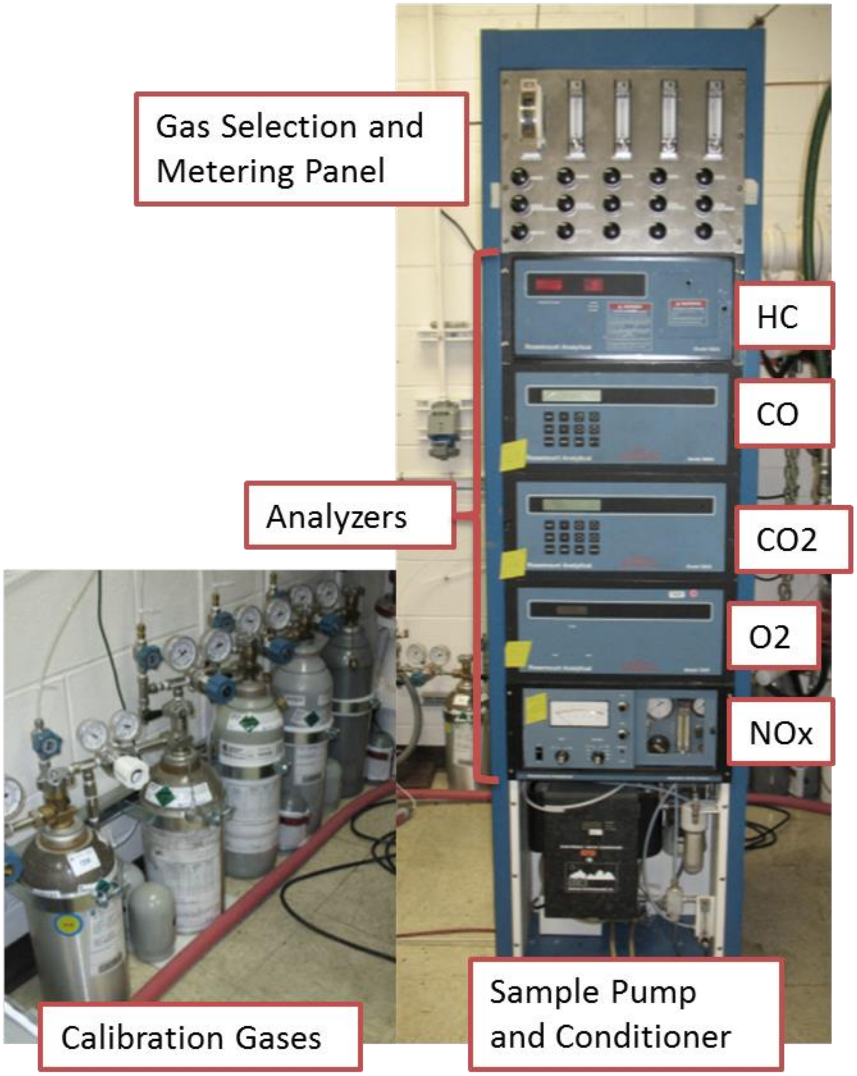

Figure 50: Exhaust gas analysis system

3.5. Electrical Output

Electrical current output from the linear alternators was measured at each load resistor using a LEM HAL 100-S instantaneous output Hall effect current transducer with ±300 A measuring range. Electrical current measurements were made on eight of the individual coils using LEM HAL 50-S instantaneous output Hall effect current transducers with ±150 A measuring range.

3.6. System Temperatures

Type K thermocouples were used to measure combustion chamber intake and exhaust temperatures, as well as temperatures in the pneumatic drive system supply and vent tanks. Exergen µIRt/c-K-240F/120C self-powered infrared temperature sensors were used to measure piston temperature near the permanent magnets, as permanent flux loss begins at around 80°C. On each side of the engine, two sensors were placed between the bounce chamber cylinder and the linear alternator, and two were placed between the linear alternator and the combustion chamber cylinder. The sensors see a midsection of each anodized aluminum piston end running beneath them.

3.7. Data Acquisition Hardware

Data acquisition was split into three categories based on required sampling rate. Slow changing data was taken at 10Hz using Data Translation USB data acquisition modules. Thermocouples and infrared temperature sensors were read on two DT9805 16-bit thermocouple modules. Voltage level signals including emissions measurements, drive pressure feedback, and vent pressure feedback were read on a DT9804 16-bit multifunction data acquisition module.

To capture the fast pressure rise rate associated with HCCI combustion, in-cylinder pressures were recorded at 225 kHz using a DT9836 16-bit simultaneous data acquisition module. Piston position measurements were made on this device to ensure simultaneity with pressure measurements for cycle work calculations. Individual coil currents were also measured on this device, the high speed allowing instantaneous current measurements to look at the phasing between alternators due to differences in piston dynamics. Remaining measurements were made at 25 kHz on three synchronized IOtech 6230 24-bit simultaneous voltage input modules.

3.8. Data Analysis

Data analysis was performed in Matlab using a script written to read in voltage measurements, scale to engineering units, and perform calculations. In order to perform thermodynamic cycle calculations, code was written to detect BDC, TDC, and port opening and closing from the piston position data. Digital low pass filtering with a cutoff around 1 kHz was applied to the piston position data for better noise rejection while finding these events. Operating frequency is calculated based on the time between successive BDC positions.

Bounce chamber pressures were adjusted cycle by cycle to compensate for the slight long term drift encountered. Based on experimental data, a piston position with the bounce chamber vent ports open was chosen at which the bounce chamber pressure typically has equilibrated with the vent manifold pressure. At this point, the piezoelectric transducer is referenced to a flush diaphragm strain gage pressure transducer in each manifold. Data for the preceding cycle was adjusted assuming a linear drift rate such that piezoelectric transducer reading matched the strain gage transducer at the reference point. A similar procedure was used for the combustion chamber pressure transducers, using the mean of intake and exhaust plenum pressures at BDC as the reference.

Cylinder volumes were calculated using the previously described adjustments for deflection of the piston and sensor core. Volumetric compression ratio is calculated as the volume at port closure (1.97L) divided by the volume at TDC. Note that this parameter is mainly a measure of how far the pistons travel toward TDC. The point at which autoignition occurs would have more bearing on the potential efficiency of the cycle. For this reason, the compression ratio at autoignition is also estimated from the data. This was accomplished by first performing a net heat release rate analysis. An ideal gas model with air as the working fluid was used. The specific heat ratio was obtained from REFPROP fluid property database as a function of the cylinder pressure assuming isentropic compression and expansion. With the net heat release rate calculated, a threshold value was chosen to distinguish the combustion event from noise in the data. The first point in each cycle with a heat release rate above this threshold was designated as the start of combustion, and the compression ratio at this point was calculated for reference. Ideally, autoignition corresponds with TDC, and in cases with compression beyond the point of ignition, additional energy is lost on account of the higher temperatures and increased blowby.

The steady state fuel energy input in Joules per cycle is calculated based on the lower heating value of hydrogen (120.0 MJ/kg), the mean fuel flow meter reading in g/s during each cycle, and the cycle duration. The mass flow rate of air is calculated using the volumetric flow meter along with the pressure and temperature measurements immediately upstream of it. The fuel/air ratio is calculated using the flow rate from the fuel mass flow meter and this calculated air mass flow rate. Note that this calculation does not account for any short-circuiting during the scavenging process. A throttling valve on the inlet of the intake blower was adjusted to match the blower flow rate to the estimated air consumption based on engine frequency, cylinder volume, and assumed fill density. In practice, some amount of air may flow through to the exhaust during scavenging. The fuel injection was intentionally delayed until about 1.5 ms after intake port opening to avoid losing fuel in this manner.

Instantaneous electrical power is calculated from the load resistance (assumed constant) and measured load currents. Simultaneous measurements of resistor current and voltage drop during motoring and combustion experiments verified that the resistance did not change significantly over the course of a test. The instantaneous power is integrated on a cycle by cycle basis to compare electrical energy produced with mechanical energy input. Indicated work is calculated as the pressure-volume integral over each cycle. This calculation is made for the combustion chamber as well as both bounce chambers. The sum of these three work calculations is taken as the total mechanical energy transferred to the pistons. The fuel conversion efficiency, or indicated thermal efficiency, is calculated as the indicated work per cycle divided by the fuel energy delivered per cycle.

4. CONTROL AND SAFETY SYSTEMS

Control systems for the engine are implemented in hardware and/or software depending on factors such as response time, user adjustability, and simplicity.

4.1. Start-up Control

Section 2.9 described the start-up system hardware and procedure. This section describes the electronic hardware-controlled starting sequence that is used to execute the start-up procedure. A diagram of the starting sequence is shown in Figure 51. Prior to each test, the buffer tanks are filled with the air compressor to its maximum output of 900 psig. The nitrogen supply is then turned on, and an electronically controlled pressure regulator is used to adjust the buffer tank pressure to the desired level. The pistons are manually pulled to the outermost position, which is limited by the point at which the shoulder screws contact the valve plate. To start a test, a switch is manually actuated which closes the bounce chamber bleed valves and initiates several other operations. A logic-level voltage is controlled by a second pole on the same switch, which provides triggering for the IOtech data acquisition as well as reset signals for various control circuits. Once this switch is thrown, a delayed interval timer waits an adjustable duration of time (set around 200 ms) to allow the bleed valves to close, then generates a pulse of adjustable width (set around 40ms) to control solid state relays which fire the helium start system solenoids. In addition, the pneumatically operated ball valve in the vent system is triggered to open. Its actuation time of around 250 ms provides sufficient time delay to maintain vacuum until the first cycle of helium has vented. At the same time, a pilot valve opens, providing compressed air to open the pneumatically actuated fuel shutoff valve and to start the engine oil metering system. The fuel shutoff valve opens and closes in 30 to 60 ms, so the 200 ms delay before firing the helium start valves gives the fuel line sufficient time to pressurize.

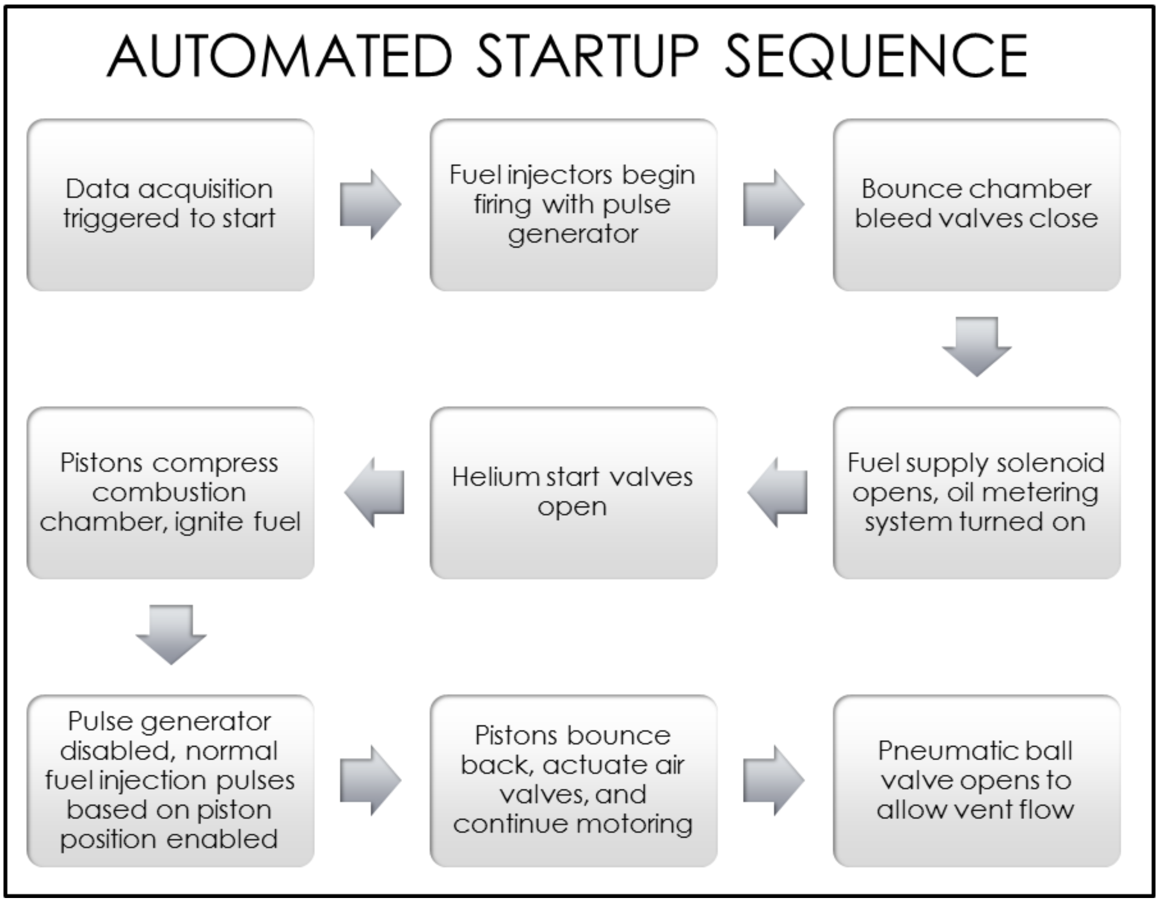

Figure 51: Automated piston starting sequence

4.2. Motoring Control

As discussed in Section 2.7, control for motoring the pistons, with or without combustion energy, is accomplished by way of the air injection pressure and the bounce chamber vent pressure. Air injection pressure is primarily used to control the compression ratio for the combustion chamber. This pressure determines the expansion work of the bounce chamber cylinders which drives the pistons to TDC while providing electromagnetic energy and compressing the combustion chamber gas, losing some energy to frictional losses. Since the intake and exhaust pressures of the combustion chamber and the electromagnetic energy generated are not adjusted, the air injection pressure is used to adjust compression ratio.

In the opposite direction, the vent pressure of the bounce chambers can be adjusted to affect the extent of piston travel (BDC location). The expansion work of the combustion chamber drives the two pistons outward generating electromagnetic energy, compressing the bounce chamber gas, and fighting frictional losses. The pressure in the bounce chambers at the start of compression, the vent pressure, determines the amount of energy absorbed and therefore, the extent of travel. During combustion, fueling rate will also affect outward piston travel. This will be discussed in the next section.

A Tescom 44-1316-2122A002 air loaded regulator with ER3000FV-4 electronic pressure controller (Figure 52) is used to control air injection pressure of the pneumatic drive system. Feedback to the controller is provided by a Teledyne Taber full bridge pressure transducer with Dataforth SCM5B38-02 strain gage input module. The controller communicates through RS-485 interface to the engine control computer, allowing the pressure to be set manually or adjusted automatically with engine control code. Typical PID tuning was carried out to obtain appropriate pressure response with the expected flow rate. At the beginning of a test, the step change from no flow to full flow tended to cause a drop in the drive system pressure due to limitations in regulator response time. To compensate, the controller tuning was adjusted to maintain a minimum control pressure on the air loaded regulator.

Figure 52: Tescom pressure regulator used to control the pneumatic drive supply pressure

A Bray series 20 1-1/2” butterfly valve with series 70 electric actuator was used to adjust the bounce chamber vent system pressure. The valve is controlled with a 0 – 10 V signal from the DT9814 module and supplies a position feedback signal to the DT9804 module. Both signals represent valve position as a fraction of fully open. Basic tests of pressure drop versus valve position were made with the valve installed in the system to get a sense for its response and useful range. Data from one of these tests is shown in Figure 53 below. Air flow was provided at ~250 scfm while the butterfly valve was set at several different positions from 99% open to 46% open. The vent manifold and vent tank steady-state pressures were recorded for each position. The results show that the valve must be closed to less than about 81% before a backpressure is produced. Between 81% open and 46% open, a back pressure of ~10 psia can be produced at this flow rate. These results indicated that a good dynamic range was capable of being produced using the butterfly valve.

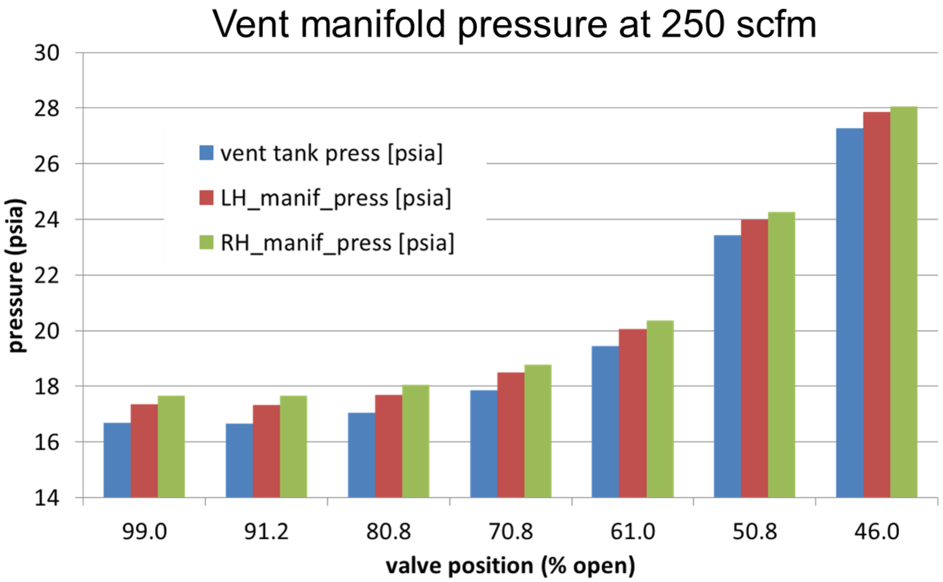

Figure 53: Bounce chamber vent manifold pressure as a function of butterfly valve position with 250 scfm flow rate

4.3. Combustion Control

The combustion system components, including the hydrogen fuel injectors, were described in Section 2.3. Operation of the fuel injection system uses a combination of hardware and software controls to allow full adjustment of the fuel injection duration and timing within the engine cycle. A schematic of the fuel injector control system is shown in Figure 54. Inputs are shown in blue, electronic hardware in white, and outputs to the injector driver in red. An analog voltage comparator was used to trigger the injectors. Signal filtering and hysteresis ensured that noise and signal glitches would not produce unwanted injection triggers. The comparator reference voltage is set by the data acquisition software for easy adjustment of injection timing. The comparator output triggers two counter/timer outputs which generate the fuel injection pulses. The injectors are driven by an AEM peak and hold injector driver module configured with one injection pulse driving a single injector and one driving a bank of four injectors for a wide dynamic range of fueling.

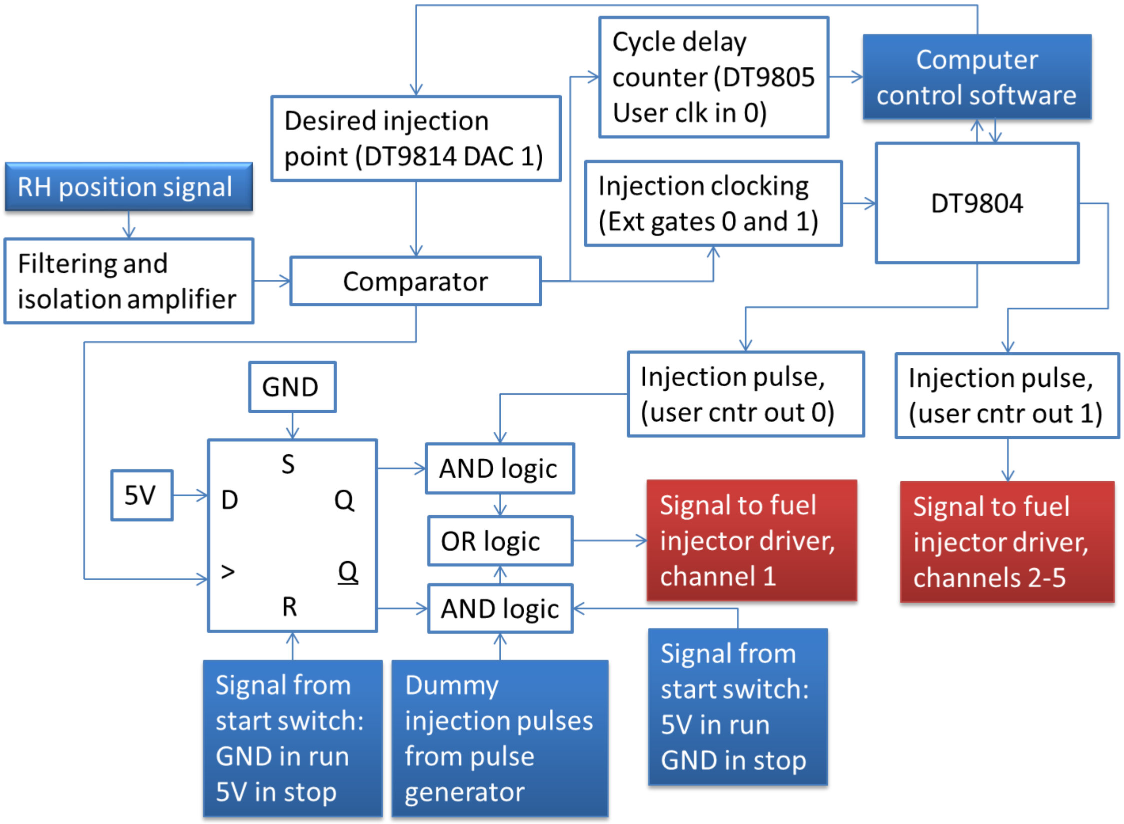

Figure 54: Schematic of the fuel injector control system

4.3.1. Manual control

The combination of pulsewidths and number of fuel injectors used to control the amount of hydrogen injected per cycle is determined in software. In manual control mode, the user interface of the control computer allows the user to select a desired fueling rate in milligrams of hydrogen per cycle. A lookup table of pulsewidth vs. milligrams per pulse and constraints on minimum and maximum fuel injector pulsewidths are used to then determine the pulsewidth and number of fuel injectors (either 1 or 5) used. Combinations of these two variables enabled fuel injection rates from 1 to 20 milligrams of hydrogen per cycle which corresponds to a fuel energy of 120 to 2400 Joules per cycle. At an operating frequency of 35 Hz, that represents a fuel load of up to 84 kW. Control of fueling rate is active during operation so that the user can manually change the value during a test.

As described in Section 2.11, the hydrogen start system utilizes only the single injector and is used just to provide energy for the first piston cycle. Control logic for this system is shown in Figure 54. Dummy injection pulses from a pulse generator are enabled at the start of each test. As the pistons move inward, the injection timing comparator goes high, clocking a flip flop to disable the dummy injection pulses and enable the normal injection pulses. On the second cycle, helium no longer enters the bounce chamber and is quickly exchanged with air or N2 from the pneumatic drive system. Because of the difference in compressibility of these gases, and because the bounce chambers are venting to a lower pressure than they will at steady-state, the pistons are prone to over-travel into the bounce chambers for the next several cycles. For this reason, a software delay is set up to wait a chosen number of cycles, typically between 5 and 10, before beginning normal fuel injection. This parameter is manually entered in the user interface, and is implemented as follows. As seen in Figure 54, the fuel injection timing comparator output is wired into a clock input channel on one of the DT9805 modules. Until the desired number of cycles has been reached, the DT9804 is programmed to ignore the injection timing comparator. After the delay period, it operates in repetitive one-shot mode, firing on the falling edge for injection on the outward stroke (typical) or on the rising edge for injection on the inward stroke.

4.3.2. Automated Control

As testing progressed, one issue that arose was overcoming transients. The fuel injection delay mitigated the potential for overtravel due to the use of vacuum at startup, but the fueling rate still needed to be increased gradually along with the vent pressure to keep piston motion within limits. Because the bounce chamber vent pressure takes time to build up to steady state, starting the engine at a high fueling rate and an appropriate steady state butterfly valve position would result in piston overtravel. The approach taken in initial testing was to set the butterfly valve in a partially closed position prior to a test, and start with a moderately low fueling rate. As the bounce chamber vent system pressure increased, the fueling rate was increased to maintain sufficient actuation of the air injection valves. Initially this was done manually with the computer user interface. However, that method proved difficult due to the rate at which the system dynamics changed. So, an automated control methodology was developed for fuel injector control.

A PID control algorithm was programmed in the control software for this purpose. In the PID controller, a target piston travel into the bounce chamber is defined. The maximum piston position signal is detected for each block of data coming from the data acquisition module. If the detected maximum voltage is less than the target voltage, the fueling rate is increased to increase the piston travel into the bounce chambers. If the detected maximum voltage is greater than the target voltage, the fueling rate is decreased. Being able to update the fueling rate every three to four engine cycles, this control was sufficiently fast to track the rising vent pressure and increase the fueling rate to maintain adequate actuation of the air injection valves as will be shown later in the Results sections.

4.4. Safety Systems

4.4.1. Shutdown triggers

When the engine is running, any number of reasons may exist that require it to be stopped including safety related reasons. For this purpose, a shutdown sequence was designed and implemented to stop the piston motion within a few cycles when desired. In addition, several methods were put in place to trigger the shutdown sequence. To allow an operator to stop the engine, whether for safety or another reason, the engine shutdown sequence may be initiated manually by pressing a large red emergency stop button or a stop button in the software graphical user interface.

For an automated trigger of the shutdown sequence, it may also be initiated by software or hardware generated shutdown triggers designed for safety and prevention of mechanical damage to the engine. Two main events were identified as triggers for engine shutdown. One is loss of piston synchronization. There is a limit to the restoring force provided by the linear alternators being wired in parallel, beyond which stability can be lost. Without synchronized motion, it is possible in this design for a piston to move past the centerline so far that the magnets attempt to enter the combustion chamber and the bounce chamber piston comes out of its cylinder. To avoid the mechanical damage likely in these scenarios, the engine is triggered to shut down if the pistons get out of synchronization by a certain threshold. The primary means of doing this is through analog hardware for speed and reliability. An overall block diagram of the shutdown triggering hardware is shown in Figure 55. Inputs to the circuit are shown in blue, which include user activated switches, threshold adjustments, and sensor measurements. Electronic components are shown in white. Piston position signals are filtered and isolated, and the voltage difference between the signals is calculated. The absolute value of this difference is then calculated, and a voltage comparator triggers if the difference gets above an adjustable threshold.

Another event which triggers engine shutdown is overtravel of the pistons into the bounce chamber cylinders, which indicates that too much energy is being added to the system. This condition can cause the bounce piston to bottom out in the cylinder. Again, the primary means of detecting this event is with analog hardware. Voltage comparators trigger if either piston position voltage gets above an adjustable limit. The piston synchronization trigger and the two piston position triggers feed into an OR gate, whose output is fed to the set pin of an RS latch. The reset pin is kept low while the engine is in operation, so the output latches high if any shutdown trigger is received. As the start switch is flipped back to the stop position at the end of a test, the reset pin goes high to clear the shutdown trigger. As a backup to the analog hardware, these same shutdown triggers are programmed into the engine control software; though the time required to generate a trigger is around 100 ms, compared with < 1 ms in the hardware. The software trigger is brought into the electronic hardware at the enable pin of the latch, such that the latch output is pulled high unless it is receiving an enable signal from the control software. Finally, OR logic allows either the latch output or the emergency stop button to trigger engine shutdown.

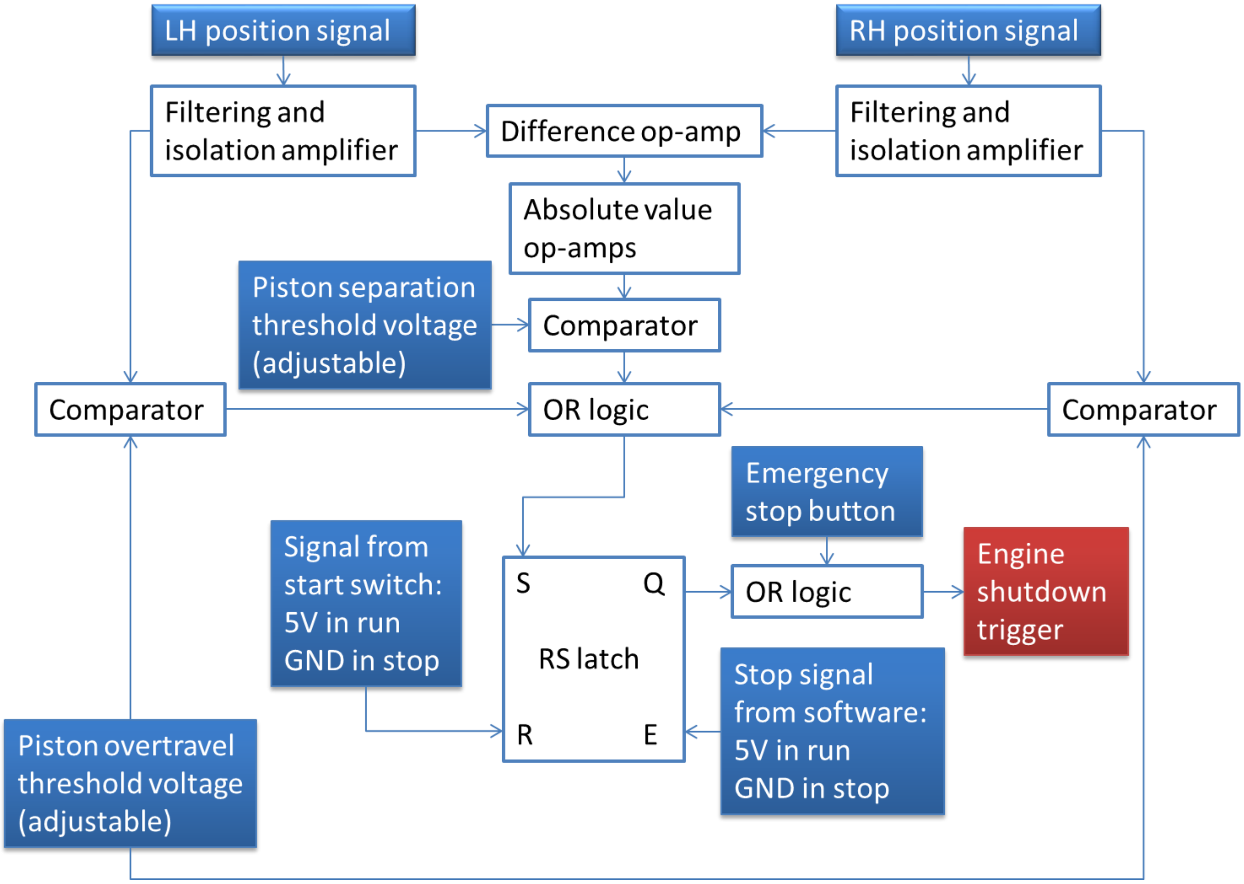

Figure 55: Block diagram of the shutdown triggering hardware

4.4.2. Shutdown sequence

To shut down the engine, energy inputs need to be disabled, and the electromagnetic and friction forces will bring the pistons to a stop within a few cycles. Combustion energy is easily shut off by cutting power to the fuel injectors. For this purpose, an Omron G8P-1A2T-F-DC24 SPST-NO mechanical relay is placed in series with the fuel injectors. As an added layer of safety, this relay is operated using the same power supply as the engine shutdown system. Thus, fuel injection will not occur if the shutdown system is disabled. When a shutdown trigger is received, power is removed from the relay. This relay opens in less than 10ms, so fuel is shut off in less than one-third of a cycle.

Since direct control over the annular air injection valves is not possible, removing this energy source is more complicated. Shutting off the high pressure gas supply would be an option, but to accomplish it quickly would require positioning the valves between the buffer tanks and the bounce chamber heads. In this location, four valves rated to 1500 psig with large flow coefficients and fast actuation would be required. We chose instead to prevent the annular air injection valves from being actuated by the pistons. To do this, the bounce chamber pressure is rapidly increased by shutting off flow out of the vent manifolds. Though this requires eight valves, the required pressure rating drops to 100 psig, which enables the use of inexpensive diaphragm valves with very large flow area. Sizto Tech Corporation model 2WO400-1 1/2-1-D normally open direct acting diaphragm valves were used. The diaphragms were modified for a quicker and more positive shutoff. In addition, a power supply with automatic switching between constant voltage and constant current was used, with a capacitor in parallel to provide the initial high voltage. The supply was set to its maximum of 32 VDC, with the constant current limit set to achieve the continuous duty rating of the valves. With the vent flow shut off in this manner, the vent manifolds fill to higher pressure with each cycle, reducing the net energy input to the bounce chambers.

With the fuel injectors disabled and the bounce chamber vent valves closed, all energy input is removed within a few cycles. As the vent manifold pressure builds during these few cycles, the extent of piston motion into the bounce chambers is gradually reduced. When they reach a point where the annular air injection valves are no longer actuated by the pistons, all energy inputs have been removed, and the system quickly equilibrates. During this transition, if piston synchronization is poor, it becomes possible that one piston travels back far enough to open the air injection valve while the other does not. The piston that opens the valve will travel faster toward the center, most likely going past the engine center plane before turning around. In this particular engine, this means that the piston rings may travel over the access ports in the cylinder, where they can be damaged. In extreme cases, the magnets can enter the combustion chamber cylinder and the bounce piston can come out of its cylinder. To reduce the likelihood of these events, it was desirable to stop the pistons more immediately. Gas injection systems were therefore added to the bounce chamber vent manifolds to bring the pressure up immediately after the vent shutoff valves have closed. To pressurize the manifold quickly, like the He start system, a small volume of high pressure He connected to the manifolds with solenoid valves was used. The vent pressure added is high enough that the bounce cylinder pressure, once compressed to the point of valve actuation, will be at or above the head pressure. This means that, even if a piston travels back far enough to open the air injection valve, the bounce chamber pressure will not change, so no imbalance is introduced.

A final action taken is to isolate the fuel supply from the experiment using an Asco 8290A791 normally closed angle body pilot operated valve, its straight-through design causing minimal flow restriction. This valve is actuated with compressed air using an Asco 8327G041 high flow direct acting pilot valve. An overall summary of the shutdown sequence described above is shown in Figure 56.

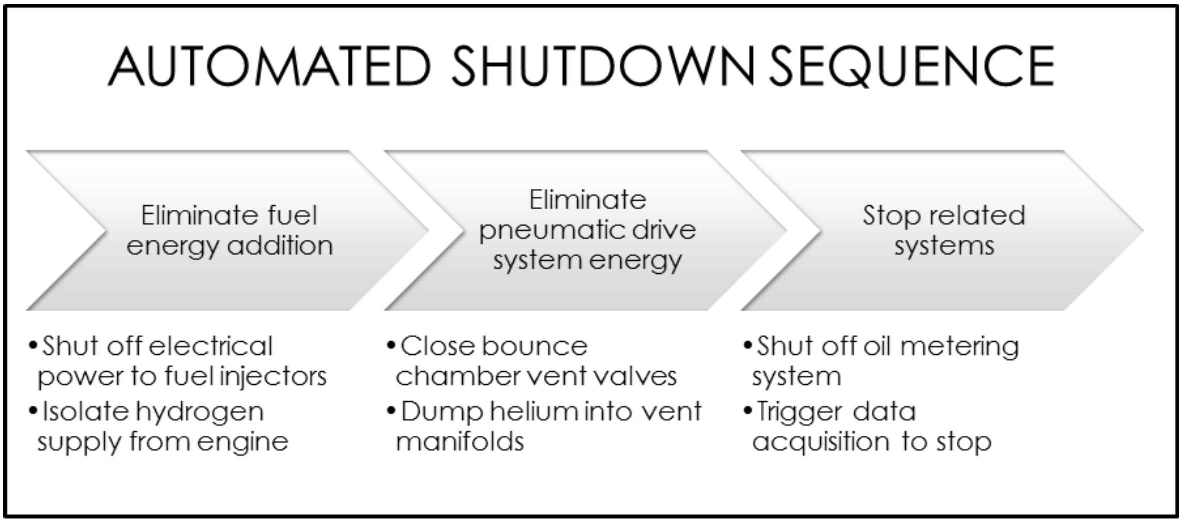

Figure 56: Automated shutdown sequence

A typical engine shutdown event is shown in Figure 57. The plot includes the bounce chamber pressure (solid green curve), the vent manifold pressure (dashed green curve), the piston position (solid blue curve), and the shutdown trigger (dashed blue curve). In this case, the piston travel limit was exceeded at approximately 0.56 seconds and the analog hardware generated a shutdown trigger. As the vent manifold pressure shows, within less than half of an engine cycle, the vent shutoff valves are closed and helium is flowing into the manifolds.

Consider now the bounce chamber log P vs log V plot in Figure 58. The blue curves show the cycle in which the piston travel triggers the shutdown event. Looking at the expansion stroke, as the pistons move toward TDC and the bounce chamber vent ports open, gas initially flows out of the bounce chamber cylinders into the manifolds. Shown in the subsequent compression stroke (green curve), this flow is quickly reversed as the injected gas brings up the manifold pressure. As the vent ports close, the bounce chamber cylinders contain essentially the same charge of gas they did during the prior expansion stroke. Thus, the compression stroke with the stop system enabled closely follows the previous expansion stroke, and even though the travel is far enough to actuate the annular valve, there is no energy addition because the pressure is about the same as the supply pressure. In subsequent cycles, referring back to Figure 57, the piston travel decays until the electromagnetic and friction forces quickly bring the pistons to rest.

Thus, no net energy is transferred to the pistons from the pneumatic drive system once the stop system is enabled. Also, if the pistons contain enough kinetic energy to fully compress the bounce chamber cylinders to the point of actuating the annular valves, the bounce chamber pressures will already be near the head pressure. Therefore, differences in valve actuation between the two sides will not drastically change the amount of energy one piston gets compared with the other, and the pistons are able to maintain synchronization as they come to rest.

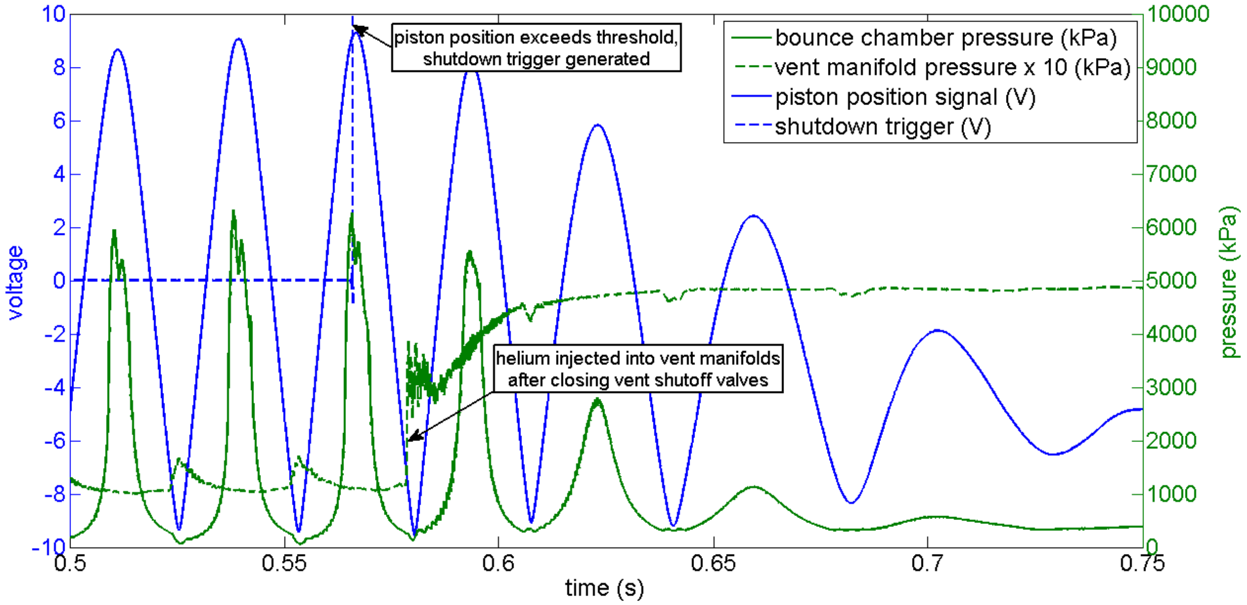

Figure 57: Typical shutdown event

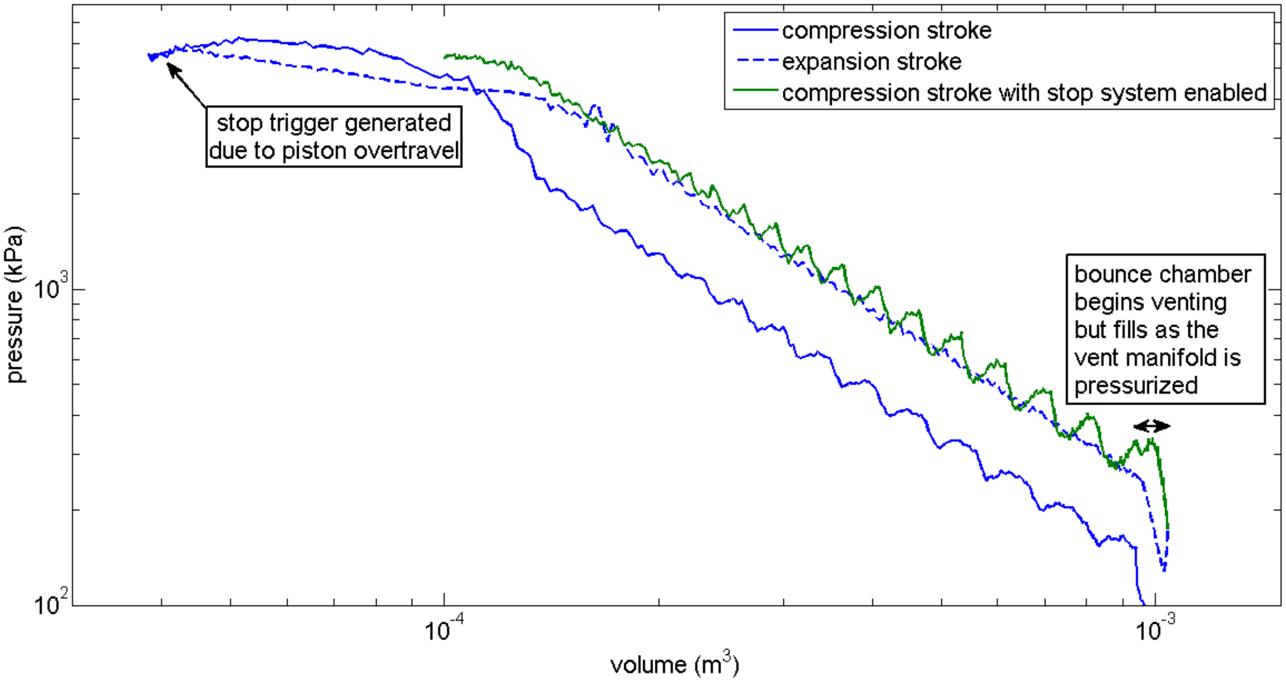

Figure 58: Bounce chamber logP-logV during shutdown

4.4.3. Pressure Safety

Standard practices were followed for ensuring pressure safety for the experiment. All gas bottle manifolds were fitted with appropriate relief devices based on the regulator flow coefficients. Bounce chamber cylinders, piston ends, and pneumatic drive components were designed for 1,500 psig MAWP, while a relief valve downstream of the electronically controlled regulator limits this pressure to 1,300 psig. The combustion chamber cylinder and piston ends were designed for 5,000 psig MAWP. All design modifications to pressure components were modeled and simulated prior to implementation to maintain these ratings. A relief valve in the bounce chamber vent system plumbing is set at 50 psig to protect the reinforced rubber tubing used there. As part of the engine shutdown system, the solenoid valves attached to the vent manifolds close to prevent venting and bring up the pressure in the bounce chambers. This action isolates the vent manifolds from the 50 psig relief valve which is downstream. Thus, the vent manifolds are protected with their own relief devices set at 100 psig. These relief valves proved to be an important safety feature since on several occasions the custom bounce chamber valves failed open, subjecting the manifolds and solenoid valves to N_2 pressures up to ~1200 psig.

4.4.4. Gas Detection

Additional precautions were taken due to the use of combustible gases and the large volume of stored nitrogen. The hydrogen bottle is stored outside the building and plumbed into the lab, with a solenoid valve near the bottle controlled from inside the lab. This solenoid valve is interlocked with the room ventilation fan, such that the valve cannot be opened unless the ventilation fan is on. A hydrogen detector is installed in the lab to provide a local alarm to alert the operators as well as an alarm to the Sandia Central Alarm Station in the event of a release. The 16-pack of nitrogen for the pneumatic drive system is also stored outside and plumbed into the lab. A manual shutoff valve located near the engine control computer in the lab can be quickly shut off in the event of a downstream component failure. In addition, an excess flow valve installed at the manifold connection to the 16-pack limits the maximum flow into the lab. Finally, an oxygen sensor is installed in the lab due to the potential asphyxiation hazard associated with the 4,800 scf nitrogen supply. If the oxygen level falls below the setpoint, a local alarm sounds to alert the operators.

5. EXPERIMENTAL RESULTS

5.1. Start-up Experiments

The first set of tests performed involved starting the pistons moving with the helium injection system, and allowing the motion to decay without further energy addition. The bounce chamber heads were pressurized to keep the air injection valves closed and allow the bounce chambers to pressurize, but low start pressures were used so the pistons did not bounce back far enough to actuate the air injection valves. Tests were performed with the coils disconnected (open circuit) to assess piston friction and synchronization in the absence of an electromagnetic restoring force. Similar tests with the coils connected gave initial data on the electrical energy generated and the restoring force provided by connecting mirror image linear alternator coils in parallel.

Empirical friction models were developed based on the open circuit helium start data. The purpose of this effort was to provide the engine models a friction equation representative of the system, not to fully model the physics involved. An example of piston velocity for an open-circuit start test is shown in Figure 59. Here, the measured piston velocity is compared with the system model results using the friction equation listed in the figure. This model contains a constant term plus pressure dependent ring friction terms for the combustion chamber and both bounce chambers. The ring friction is calculated based on the area at the inner diameter of the ring, the cylinder pressure, and an assumed coefficient of friction. Here, the coefficient of friction is assumed constant, though in reality, it will change based on piston speed and lubrication conditions. Near the turnaround points, cylinder pressure is high and velocity is low, making boundary friction and a higher coefficient more likely. During the high velocity portion of the cycle, it is more likely hydrodynamic friction with a lower coefficient. Within the hydrodynamic region, an increasing coefficient with increasing speed would be expected.

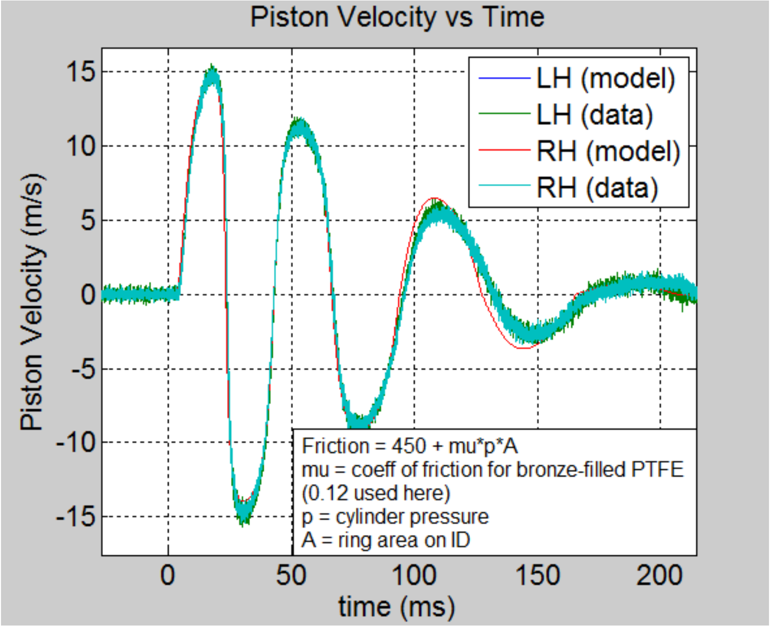

Figure 59: Measured piston velocity compared to model prediction with friction

With the previously described friction equation, a large constant term was required to match the decay rate seen in the data. In general, the observed friction was much larger than anticipated, which led to higher pressure and flow requirements from the pneumatic drive system. Several factors could be contributing to the high friction. The use of axially wide bronze-filled PTFE rings as opposed to thin metal rings is likely to increase friction. This idea is supported by the iteration in ring design described in Section 2.2. With the use of bounce chambers, a set of piston rings sees pressure at both ends of the stroke, amplifying the effect. Though the bounce chambers are not subject to the large pressure spikes seen in the combustion chamber, they do see relatively high pressure.

Operating at high compression ratio and low equivalence ratio also amplifies the effect of increased ring friction. Under these conditions, the indicated work output is small relative to the compression work. Frictional losses increase with the higher cylinder pressure, and become a larger fraction of the indicated work output. Another factor is that a 25 to 30% increase in friction was seen in open-circuit start tests after installing the magnets. Part of this is due to eddy current losses in the stator teeth and backiron, which are accounted for in the apparent piston friction observed. The remainder may be caused by side-loading of the pistons due to radial pull between the magnets and stator teeth which becomes substantial if the two are not kept sufficiently concentric. With perfect centering of the magnets within the stators, this would not be an issue. In this particular engine, the magnets are held concentric by the piston ends, so piston runout tolerances and piston-to-cylinder clearances meant that the magnets were allowed to shift off axis.

Figure 60 shows typical pressure traces for an open circuit test. In this particular test, the helium start reservoirs are filled to around 76 bar. Shortly after 160ms, the injection solenoid valves begin to open. For a few milliseconds, a slow drop in reservoir pressure and rise in bounce chamber pressure is seen as pressure above the main poppet drains through a bleed orifice. As the main poppet opens, the reservoir quickly dumps into the bounce chamber. Note that the pressure rise in each bounce chamber is nearly identical, which was typically the case. The solenoid valves showed excellent repeatability in opening simultaneously throughout the course of testing. Discontinuities in the slope of the reservoir and bounce chamber pressures can be seen as the check valve bounces closed and back open. Also note that the helium reservoir pressure remains elevated as the bounce chamber vents since its flow area is small compared with the cylinder vent ports, and the pressure differential to drive the flow is rather low. In motoring tests, this excess helium reduces piston travel on the first few outward strokes, and was the motivation for evacuating the bounce chamber vent system at the start of each test. The added pressure differential helped to pull the reservoir down closer to atmosphere during the first bounce chamber venting.

Cylinder volume data for the same test is shown in Figure 61, along with data from a test with the coils connected. The pistons remained together reasonably well in the open circuit case, indicating that there were no major frictional differences between the two sides of the engine. With the coils connected to the load resistors, the piston motion is damped out more quickly as electrical energy is being generated. The pistons do appear to stay together slightly better than in the open circuit case, though it is difficult to draw any conclusion from these tests.

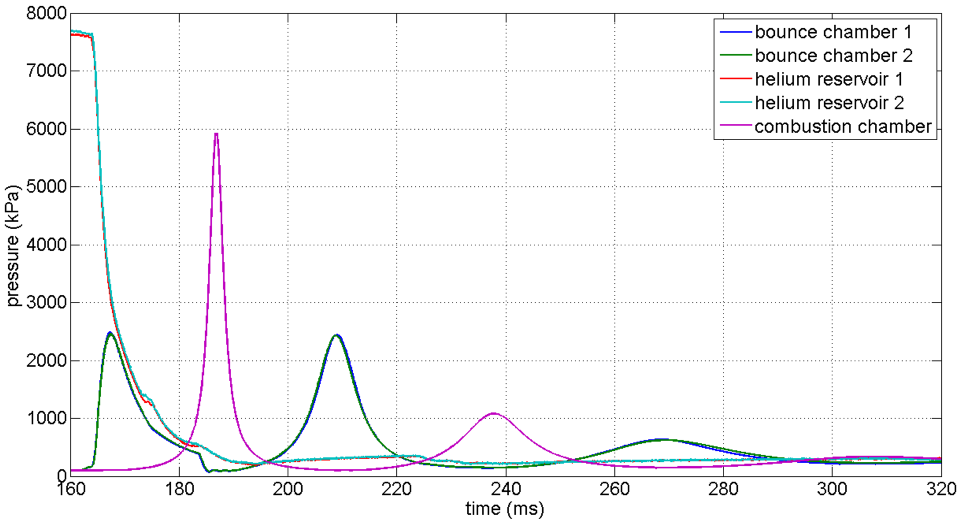

Figure 60: Typical system pressures for an open circuit test

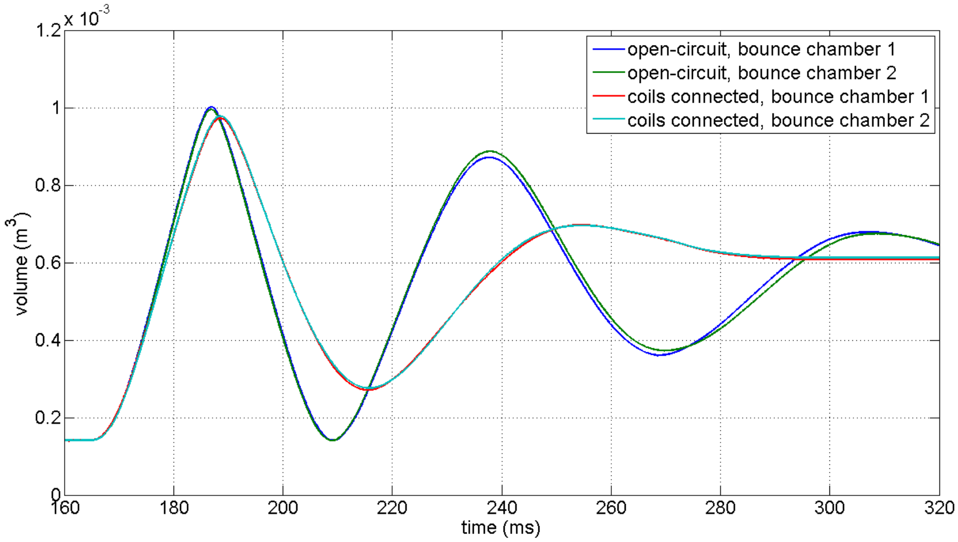

Figure 61: Comparison of bounce chamber volume between open and closed circuit tests

5.2. Motoring Experiments

The first set of motoring tests was run with the buffer tanks supplying the air injection valves filled and the compressor shut off. With limited energy supply, the engine would run for a short duration and die out, allowing initial assessment of the air injection valve operation before attempting more continuous operation. Data with a relatively low drive pressure of 815 psig is shown in Figure 62. The pistons are started moving with the helium injection system, compress the combustion chamber gas, and bounce outward to the point where the air injection valves are opened. Due to the amount of helium remaining, the cylinder pressure at valve actuation on the first cycle is near the supply pressure, so relatively little pressure rise is seen. As the reservoir vents down more completely over the next few cycles, the gas addition becomes more significant. This is most evident in the bounce chamber pressure-volume diagram, shown in the bottom plot . Note that, although the pistons did open the valves after the third cycle, the valve actuation was small, so the flow area was restricted. The time duration when the valves were open was small as well, so the cylinders did not fill to the supply pressure. With less expansion work from the gas, the pistons fail to open the air injection valve on the following cycle. Without energy addition, the pistons stop quickly thereafter. The supply pressure in this test is simply too low to sustain piston motion.

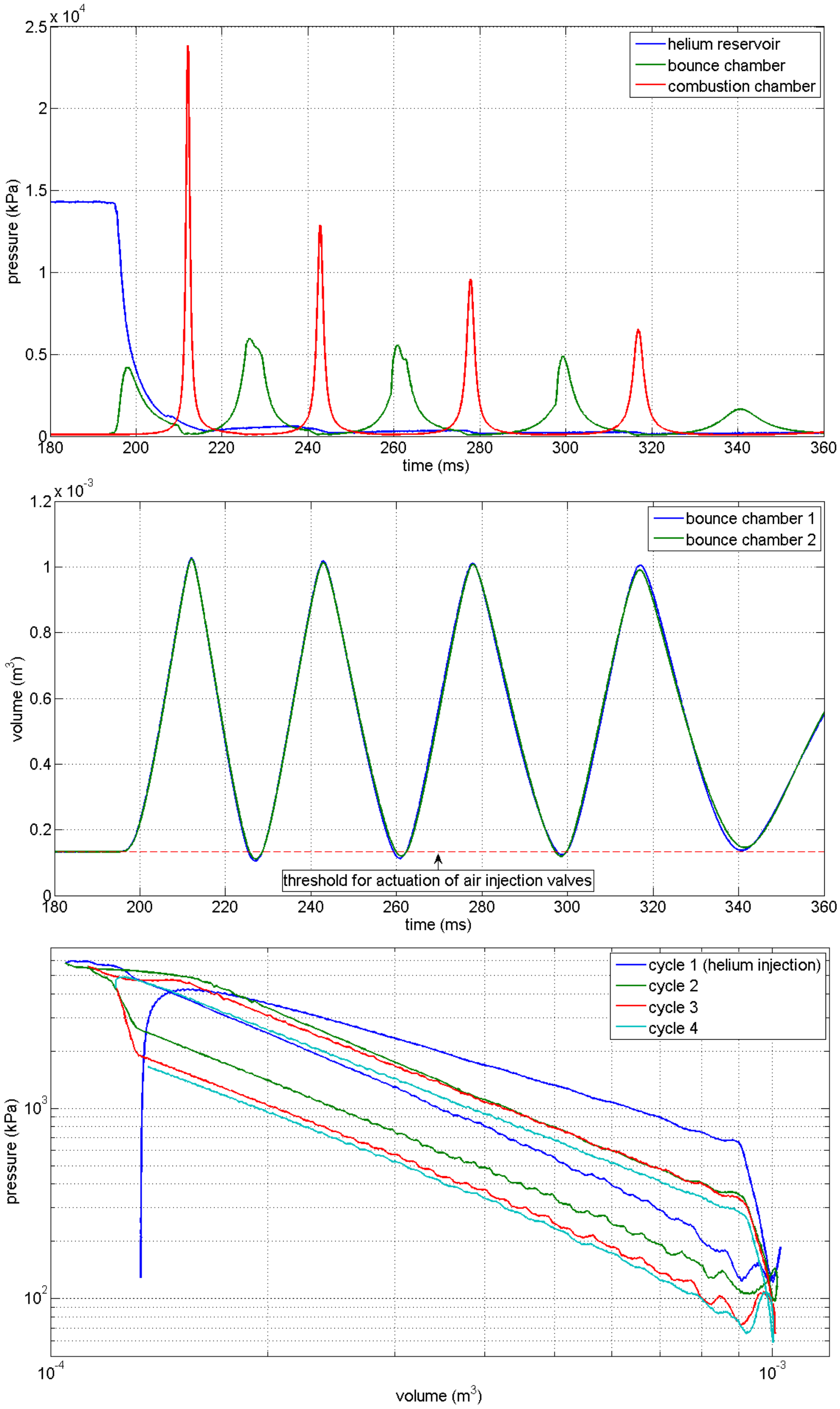

Figure 62: Data from an early motoring test. System pressures (top), bounce chamber volumes (middle), and bounce chamber logP-logV (bottom)

One issue that was discovered during the early motoring tests was that as the piston motion dies out as in the data shown above, if the pistons are not well synchronized it becomes possible for one piston to actuate the air injection valve while the other does not. This results in an energy imbalance that is far too great for the passive synchronization to correct, and the piston motion becomes completely asynchronous. The piston which opens the valve travels much more quickly toward the combustion chamber, going past the center plane before enough compression work is performed to turn it around. An example of this behavior is shown in Figure 63. Here, piston 1 actuates the air injection valve at around 367 ms while piston 2 does not. Bounce chamber 1 fills with air, causing piston 1 to travel much faster into the combustion chamber. At around 385 ms, a discontinuity in the combustion chamber pressure appears as piston 1 travels past the pressure transducer located at the engine center plane. The pressure transducer ports were carefully de-burred to avoid scratching the piston rings in these circumstances, but the potential for ring damage still remains, particularly when crossing the ports under higher pressures. In extreme cases, the piston can come completely out of the bounce chamber cylinder and damage the bounce piston top when it tries to go back in. At the same time, the magnets can travel into the combustion chamber cylinder. Being a close fit, this can damage the magnets and score the cylinder wall. Thus, operating the engine with piston travel near the threshold of valve actuation is undesirable.

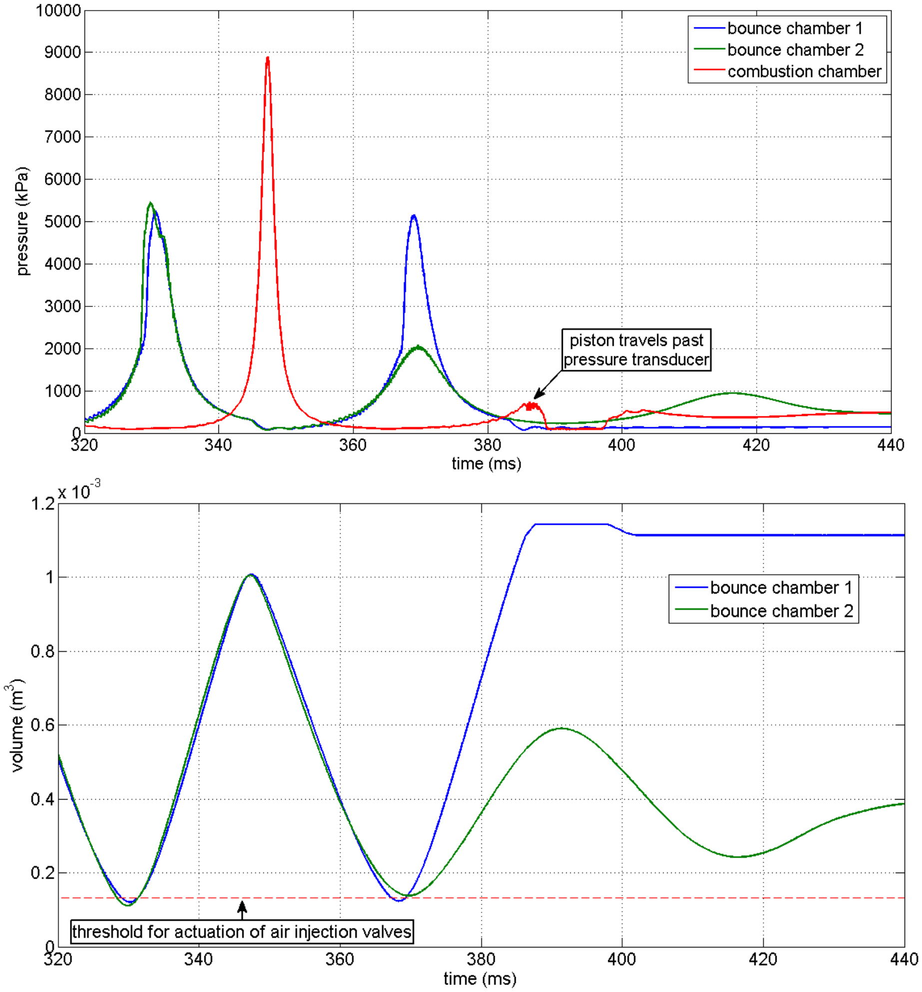

Figure 63: Example piston synchronization issue. System pressures (top) and bounce chamber volumes (bottom)

Engine motoring progressed to the point of several seconds of run time per test as issues were found and addressed. Several minor modifications were made to improve high pressure gas flow into the bounce chamber cylinders and expanded gas flow out of the cylinders. Lengths of 1” OD tubing were added in the gas supply lines where they connect to the bounce chamber heads, and a volume constructed of 1” OD tubing was connected to the third port on each head. These modifications increased the volume of gas contained in close proximity to the heads, addressing a pressure drop during the air injection event which limited the bounce chamber fill pressure. The four large buffer tanks downstream of the electronic regulator were too far away to be effective on the timescale of the air injection event, though they were useful in maintaining a steady supply pressure. The 1,000 psig supply regulator was replaced with a 1,500 psig regulator to achieve higher energy input per cycle, and the 16-pack nitrogen supply system described in Section 2.9 was installed to provide the high flow rate required for continuous operation.

Several modifications were made to reduce part damage and system down time. The shutdown system described in Sections 4.4.1 and 4.4.2 was added as a means of bringing the system to a more controlled and quicker stop for improved safety and reduced likelihood of piston overtravel. Delrin rider rings which had been positioned on the combustion side of the alternator section were removed due to repeated damage. The rings interfered with the magnet/backiron assemblies during piston overtravel, and were difficult to remove due to becoming wedged between their mounting plate and the magnets. All further tests relied on the piston ends to center the magnets within the stator. Careful de-burring and rounding of the combustion chamber pressure ports was performed to reduce the likelihood of ring damage during piston overtravel, and the position sensor guide rods described in Section 3.1 were added to prevent damage to the sensor core.

Several design iterations were performed on parts susceptible to failure, particularly the annular air injection valves. Modifications to the valve plate described in Section 2.7 were carried out. A relief cut was made on the mating outer head and valve nose parts to ensure contact at the sealing surfaces, and the sealing surfaces were lapped to tight flatness and surface finish. The valve nose parts were thickened after fatigue cracks developed. A progression of stronger materials was used for the position sensor guide rods, eventually settling on G-10 Garolite. When the Garolite rods began failing, a two-piece Garolite design using a hollow tube and threaded rod was developed.

Bounce chamber pressure-volume data for a typical motoring test are shown in Figure 64. During this test the pneumatic drive system was set to a pressure of approximately 1,000 psig ($6.9\text{x}10^3$ kPa). As the figure shows, the bounce chambers are compressed to the point at which the air injection valves are actuated and the cylinders fill with high pressure gas as the pistons continue to move outward until their kinetic energy has been absorbed. As the pistons move back inward, the air injection valves close, and the injected gas is expanded. Near the end of the inward stroke, vent ports in the bounce chamber cylinders open, allowing the cylinders to vent to near atmospheric pressure before starting the next cycle. Early in the test, pressure in the vent system plumbing has not yet stabilized, leading to higher net energy addition for the first 10 to 15 cycles. Typically, pressure-volume work from the pneumatic drive system was input at a rate of 33 to 41 kW, and an electrical output of 16 to 20 kW was obtained.

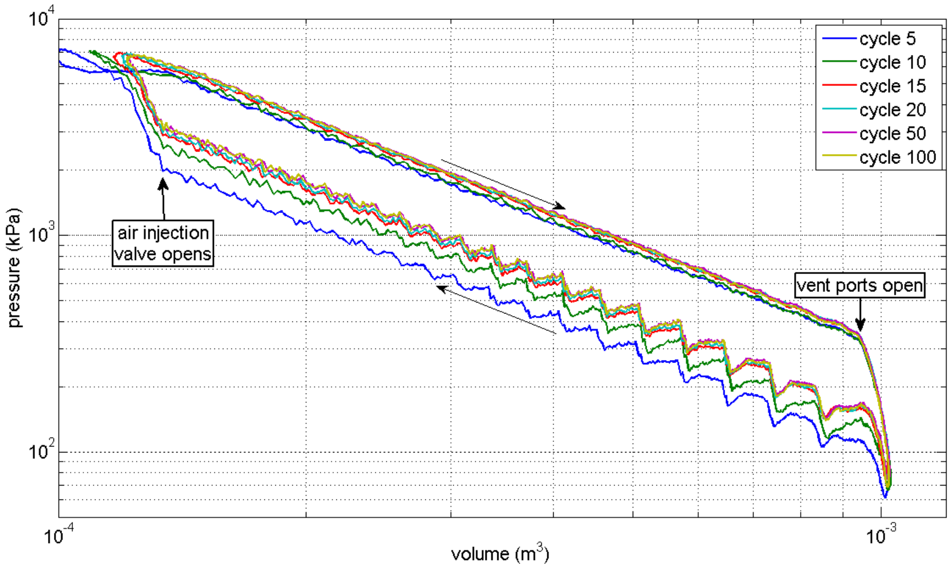

Figure 64: Bounce chamber logP-logV for typical motoring test

A time history of the pneumatic drive system pressure is shown in Figure 65. The supply pressure droops by about 20 psi initially due to the regulator, but the pressure is then maintained within 10 psi by the controller throughout the test. The vent tanks begin evacuated and quickly rise in pressure with incoming flow from the bounce chambers and with ambient air flow once the ball valve is opened to atmosphere. The vent pressure then stabilizes at 3 to 4 psi above atmospheric under full motoring gas flow with the butterfly valve fully open. As a result of this elevated vent pressure, a higher drive pressure was required to obtain the net energy input required for operation, meaning that motoring experiments were limited to higher compression ratios. For combustion experiments, this was not an issue. With part of the energy coming from the fuel, the pneumatic drive pressure could be reduced to obtain the desired compression ratio.

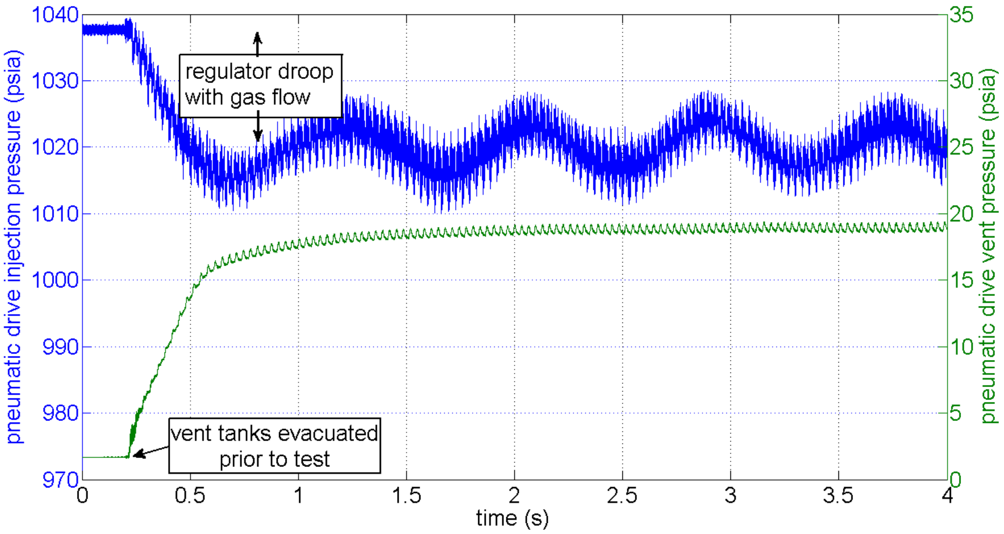

Figure 65: Pneumatic drive system pressures during a typical motoring test

With no combustion energy input, compression ratios of 40:1 or higher were typically required for sustained operation. Engine operating frequency under these conditions was about 32 Hz. Operating frequency and compression ratio for individual motoring cycles are plotted in Figure 66, showing the range of values seen in typical tests.

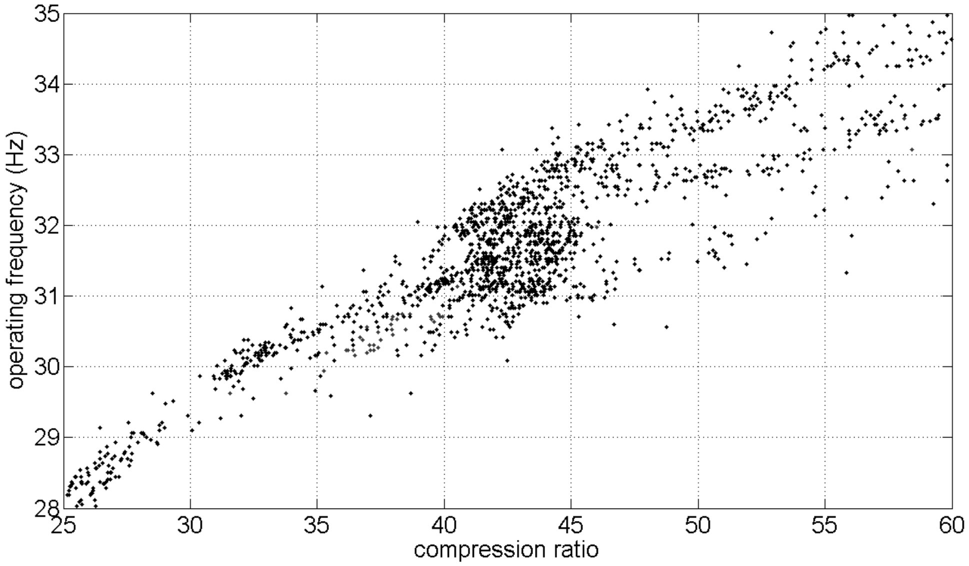

Figure 66: Typical operating frequencies and compression ratios for motoring tests

A typical combustion chamber pressure-volume diagram for motoring operation is shown in Figure 67. In the ideal case, this would be isentropic compression and expansion and the lines would be perfectly straight and directly on top of one another. In reality, the combustion chamber expands on a line slightly below the compression line due to heat and gas losses near TDC.

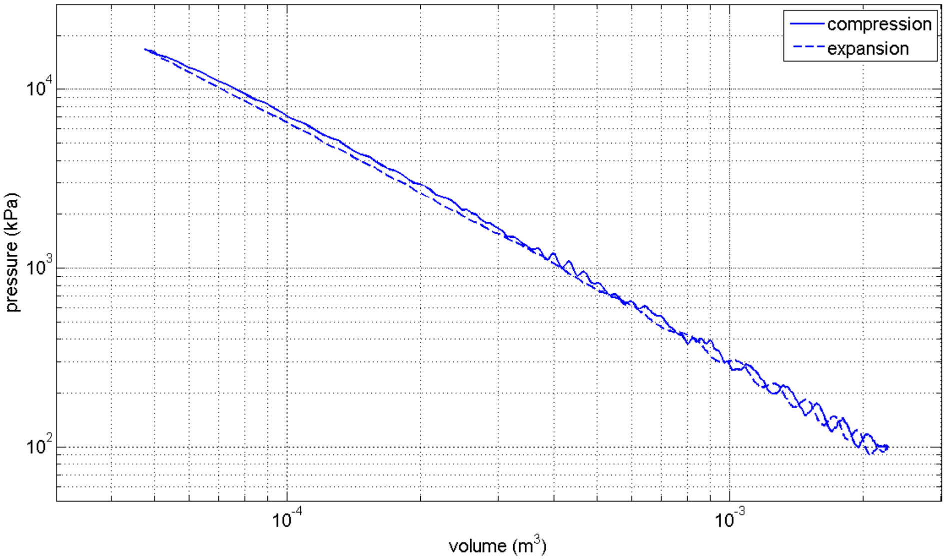

Figure 67: Typical combustion chamber logP-logV during motoring tests

A typical motoring energy balance is shown in Figure 68. The bounce chamber and combustion chamber energy inputs are calculated on a cycle-by-cycle basis from the pressure-volume data. The electrical energy output is calculated from current measurements made at each load resistor, along with the known resistance value. Losses to coil internal resistance are calculated in a similar manner. In this particular test, electrical output to the load was 49% of the work input, coil internal resistance losses were 4%, losses to piston friction and alternator eddy currents were 33% (predominantly piston friction), and combustion chamber heat and gas losses were 14%.

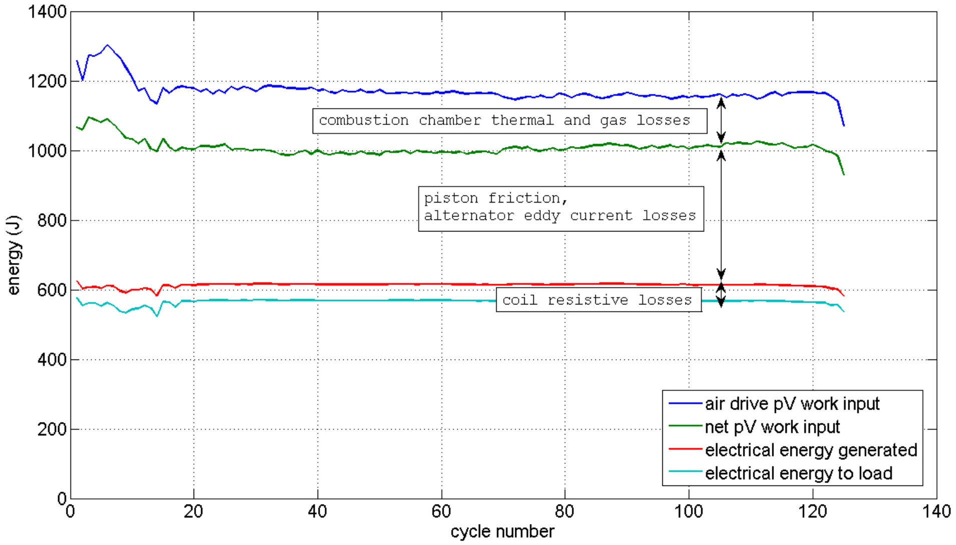

Figure 68: Energy balance for a typical motoring test

Values similar to those in Figure 68 were seen in many of the motoring tests run. For example, Figure 69 shows an energy balance for 16 of the longest duration motoring tests. The results indicate that about 50% of the input energy, which is calculated from the bounce chamber P-V integral, is converted to electrical output which is calculated from measured current and known load resistances. The remaining 50% is split among a number of loss terms, the largest of which is frictional loss. Combustion chamber P-V integrals show losses assumed to be primarily thermal, but potentially due to gas blowby as well. This term is on the order of 10%, but varies test to test. Losses to resistive heating in the linear alternator coils and lead wires are fairly small at a few percent. Eddy current losses in the alternators are not measured, but assumed by bounding the alternator efficiency between 85 and 95%. These bounds give two values for alternator losses; ~9% if efficiency is low or ~2% if efficiency is high. Since friction cannot be measured, it is taken as the remainder of the energy balance. Thus, there are two values shown for friction for each test as well. For low alternator efficiency, friction estimates range from 22 to 32%, for high alternator efficiency, friction losses vary from 29 to 39%. Note that this analysis was performed using the original pistons.

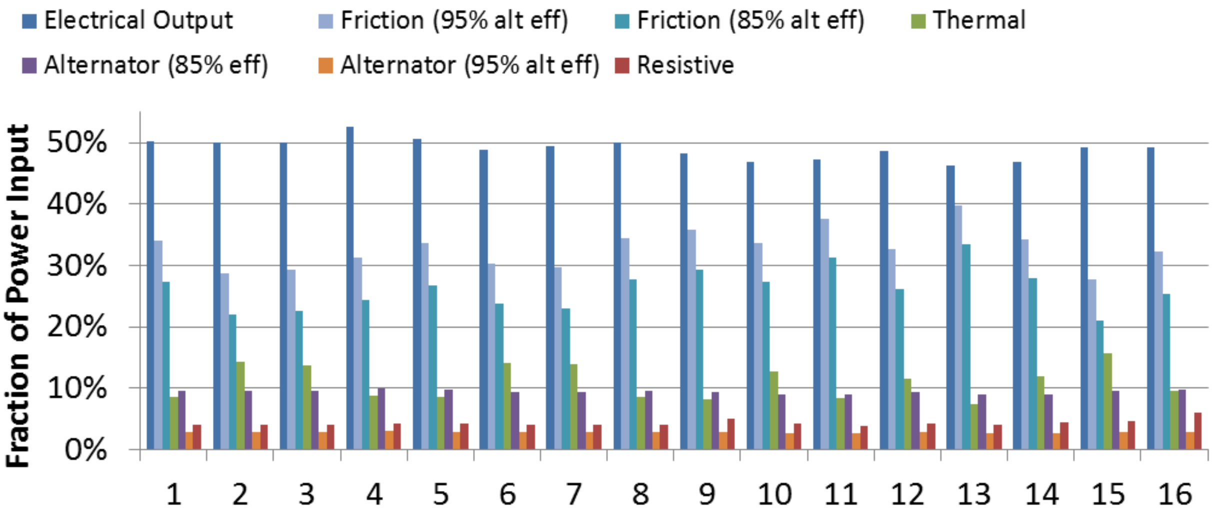

Figure 69: Energy balance for several motoring tests with assumed alternator efficiency of 85% and 95%.

These longer duration motoring tests also demonstrated passive piston synchronization through the linear alternators. The graph in Figure 70 shows piston synchronization error for five of the longest duration tests. This error is the relative difference in the piston positions with respect to the engine centerline. For many tests this error is just a few mm, compared to the 220 mm travel of each piston. Based on simulation results, asynchronous motion is initiated by a difference in friction between the two pistons. However, as the separation grows, the electromagnetic drag on the pistons works to restore synchronous motion. Importantly, this data shows that it is possible to operate the FPLA system without complex active controls to keep piston motion in sync, at least within the limited duration of these tests.

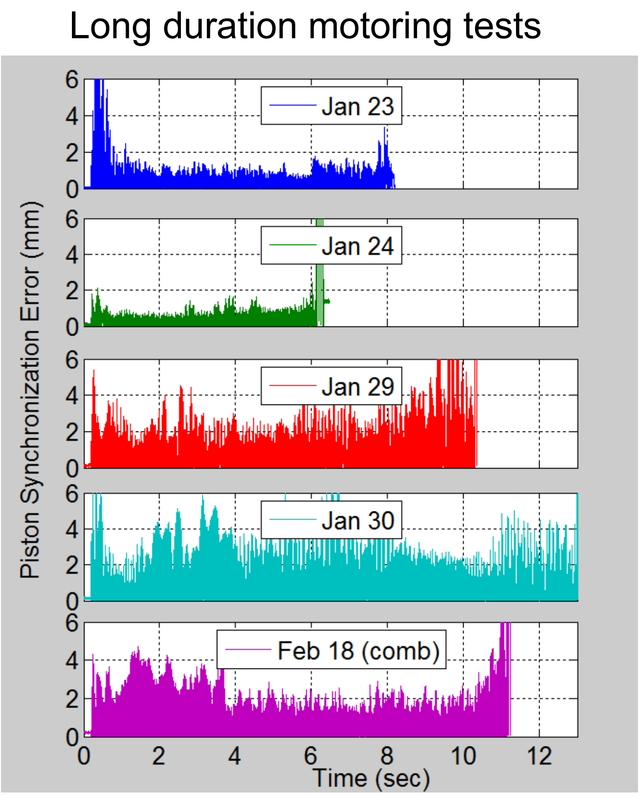

Figure 70: Piston synchronization error during five motoring tests

Another important observation from the motoring tests is that piston synchronization has a significant effect on the electrical output. Figure 71 shows a test with particularly poor piston synchronization. As the piston synchronization error climbs to 11mm during this test, the electrical output drops by 25%. The instantaneous electrical current measurements are shown in Figure 72 and Figure 73, along with piston positions. Figure 72 shows a cycle from the well-synchronized period around cycle 50, while the following figure shows a cycle from the poorly synchronized period around cycle 20. With the two pistons in good synchronization, the instantaneous coil currents for each side of the engine are nearly identical, summing to produce the maximum useful output, shown by the load resistor current. Meanwhile, in Figure 73, piston 1 leads piston 2, causing coils in stator 1 to generate well over half of the overall output. In fact, with the first pulse of current generated, a portion of the current from stator 1 feeds backward through stator 2, resulting in a load current less than what had been generated by stator 1.

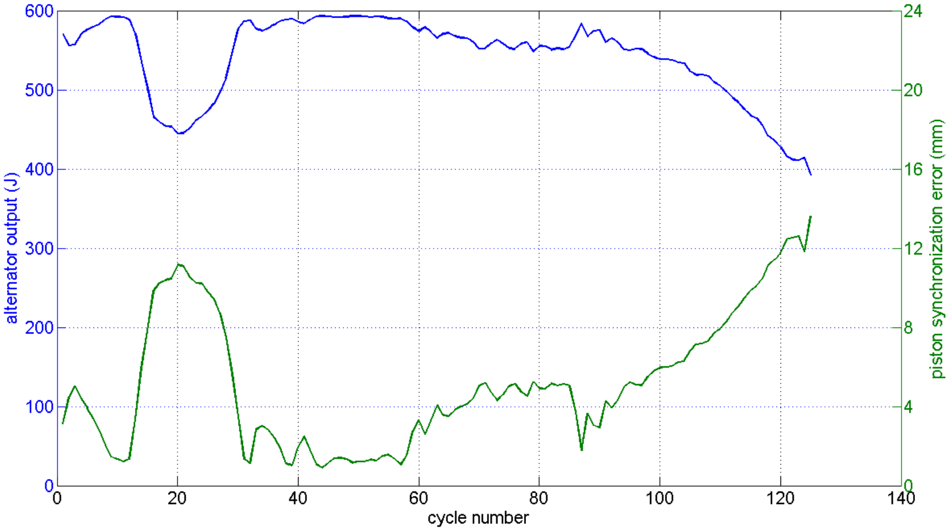

Figure 71: Effect of piston synchronization on electrical output

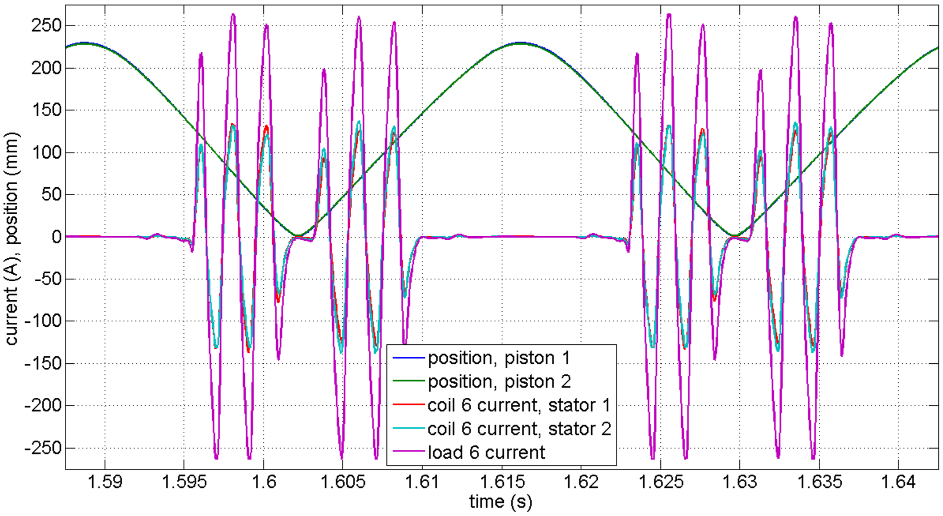

Figure 72: Instantaneous electrical current measurements when pistons are well synchronized

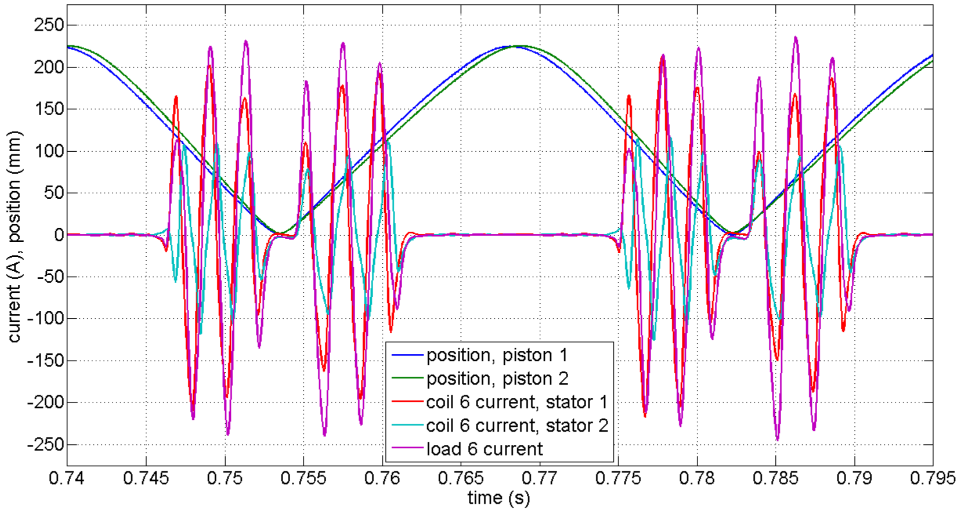

Figure 73: Instantaneous electrical current measurements when pistons are poorly synchronized

5.3. Combustion experiments

5.3.1. Overview

Initially, the intended operating procedure for the free piston engine was to motor the engine until a stable compression ratio and operating frequency were reached before introducing hydrogen. The fuel load would then be increased as the bounce chamber vent pressure was increased so that the increase in energy from the combustion chamber would be offset by a decrease in energy from the bounce chambers. However, in practice this approach proved impractical. Motoring durations had been extended by system improvements, but were still limited to less than about 30 seconds and these longer runs were achieved only intermittently.

So, rather than continue to try to improve motoring stability and repeatability through further design and process modifications, combustion experiments were pursued. A significant effort was required to prepare the system for combustion. This effort included a full safety review for operation with combustible gases, software and hardware modifications to the control and DAQ systems, and hardware modifications to the test system. A Failure Modes Effects and Criticality Analysis (FMECA) was completed and reviewed with site ES&H personnel. Control electronics and software for fuel injector control and safeguards were implemented. Other hardware including a H_2 cylinder, tubing and fittings, pressure relief device, buffer tank, flow meter, pressure gage and hydrogen flow solenoid valve were all installed

It was anticipated that introducing combustion of a low level of hydrogen early in the test could help stabilize motoring by providing a more consistent energy input. Transitioning to combustion early would also provide highly variable energy input that was controllable in contrast to the limited motoring control afforded by the pneumatic drive pressure and butterfly valve. This control authority would help overcome inconsistencies due to friction, variable valve actuation, and other non-idealities.

H_2 combustion experiments were initiated with single shot experiments that were carried out to exercise the H_2 injection system and to verify that compression ignition of low equivalence ratio mixtures would occur at reasonable compression ratios. Following the successful completion of those tests, integrated combustion and motoring experiments were pursued. Initial combustion tests were run with a constant fueling rate. Due to startup transients in the pneumatic drive system, fuel injection was delayed by around 10 cycles. This allowed the bounce chamber vent pressure to rise back to near atmospheric pressure after having been evacuated to start the engine. If fuel injection was started immediately, the pistons would overtravel into the bounce chambers. If fuel injection was delayed too long, the compression ratio would drop too low to ignite the fuel. Early tests were carried out with a very lean fuel/air mixture (equivalence ratio of .024). Several tests were run with this mixture, showing inconsistent combustion and run times of about one second. The fuel load was then increased by 50% to an equivalence ratio of 0.036. A subsequent test ran for significantly longer, ~10 seconds, and showed fairly consistent cycle to cycle values for combustion energy.

These initial hydrogen combustion experiments, although limited, were encouraging and testing was performed with successively more fuel. The amount of fuel which could be used during the initial cycles was limited, however. Higher fueling rates required elevated pressure in the bounce chamber vent system, which took time to build up. To address this problem, the fueling rate was started at a low level and manually ramped up during the tests. Later, automated fuel injector control was implemented using a PID feedback control loop to achieve a desired piston travel into the bounce chambers. With this system, the butterfly valve for the bounce chamber vent system could be set to a partially closed position at the start of a test, and the PID control would increase the fueling rate as the bounce chamber vent pressure increased, maintaining consistent piston travel.

5.3.2. Example Tests

5.3.2.1. Manual Fuel Control

With manual control of fueling rate, a number of longer duration (14 - 27 sec) tests were run with increasingly higher fuel loads with equivalence ratios from 0.036 up to 0.16. In order to accommodate the higher combustion energy, the air drive energy was reduced by increasing the bounce chamber vent pressure using the butterfly valve on the bounce chamber exhaust piping. With the butterfly valve fully open, the bounce chamber vent pressure reaches a steady value of about 120 kPa (17.4 psia). For the highest fuel-air mixtures tested, the vent pressure was brought up as high as 235 kPa (34.1 psia).

Figure 74 shows an example of the data from one of these longer duration combustion tests. The plot shows calculated energy values for each cycle of the ~900 cycle test (27 sec.). Combustion chamber and bounce chamber energy is calculated using P-V integrals while alternator energy is calculated based on measured currents. This test was initiated with the fuel injectors set to deliver 5 mg of H_2 per cycle. This value was then increased to 6 mg/cycle and then stepped up to 9 mg/cycle in 1 mg steps. Each fuel load was maintained for about five seconds between steps. Initially, the bounce chamber vents to vacuum to enable start-up which results in high bounce chamber energy. The pneumatic drive system pressures in Figure 75 illustrate this start-up transient. Another factor, albeit smaller in magnitude, is that the air injection pressure begins a bit higher than its steady state pressure. The bounce chamber energy input drops quickly to less than 600 J/cycle as the vent pressure increases to a steady value of about 235 kPa by cycle 100. The steps in fuel can be seen in the combustion chamber energy which increases from about 300 J/cycle to almost 600 J/cycle. Alternator energy output stays fairly constant over the duration of the test at about 470 J/cycle. This is about 10% below full capacity because the resistor for coil pair number 9 had failed and was at high impedance. In addition to the energy values, compression ratio and operating frequency are shown on the same axis by scaling them by a factor of 10. Compression ratio is initially very high at over 80:1 but drops with bounce chamber energy to between 35:1 and 38:1 for most of the test. Operating frequency is nearly constant over the test duration at about 34 Hz.

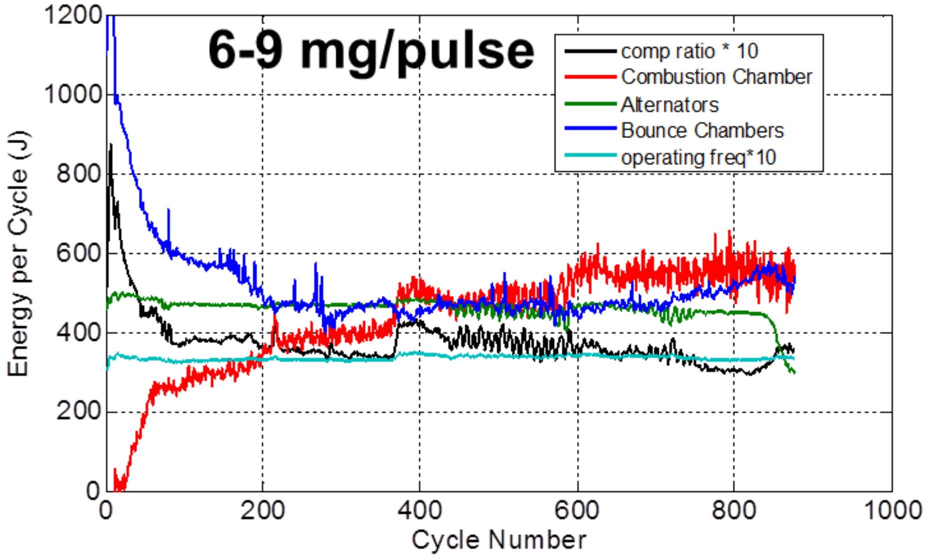

Figure 74: Energy per cycle, operating frequency, and compression ratio for an example combustion test with manual fuel control

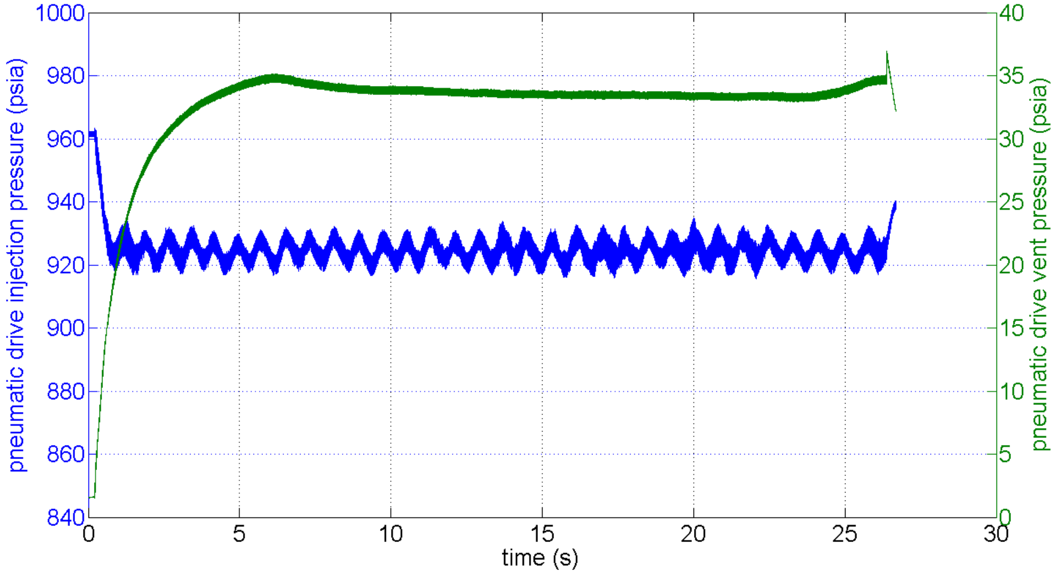

Figure 75: Pneumatic drive supply and vent pressures for the example test shown above

A second set of data obtained by manually increasing the fueling rate is shown in Figure 76-Figure 78. Bounce chamber pressures are shown in Figure 76. A lower drive pressure is used here compared with air motoring tests. In those tests, the higher pressure was necessary to achieve sustained operation. Here, with part of the energy coming from combustion, the pressure is reduced to keep the compression ratio lower. The butterfly valve was set at 45% open to introduce a pressure drop in the bounce chamber vent system and allow higher combustion chamber fueling. As seen in the figure, the vent system pressure stabilizes slightly above 30 psia.

The compression ratio, equivalence ratio, and indicated thermal efficiency are shown in Figure 77. The equivalence ratio is calculated from the fuel mass flow rate and air flow rate, so it is subject to the response times of these instruments, and lags behind the in-cylinder pressure measurements. The indicated thermal efficiency shown is calculated as the combustion chamber pressure-volume integral over each cycle divided by the fuel chemical energy delivered, based on fuel mass flow rate and lower heating value. Again, due to lag time in the fuel mass flow meter, this indicator is only valid when the fueling rate is approximately constant. For example, the jumps in indicated thermal efficiency around cycles 35, 65, and 130 are artifacts of step changes in fueling rate. For the stable period between cycles 250 and 350, an indicated efficiency approaching 54% is seen. During this time, the compression ratio at autoignition was approximately 29:1, and the equivalence ratio was around 0.15. Fuel-air cycle analysis using a hydrogen-air mixture at these conditions gives the ideal Otto cycle efficiency as 67%. At such a low equivalence ratio, the motoring losses discussed in section 5.3.3 are a significant fraction of the fuel energy input and account for much of the discrepancy between the measured and ideal efficiencies. A few cycle measurements are plotted along with the ideal cycle calculation in Figure 78. The compression strokes follow reasonably well along the isentropic compression line, while the pressure rise at combustion falls short of the ideal cycle. At these conditions, the combustion event takes about 150 μs to complete, occurring with minimal change in cylinder volume.

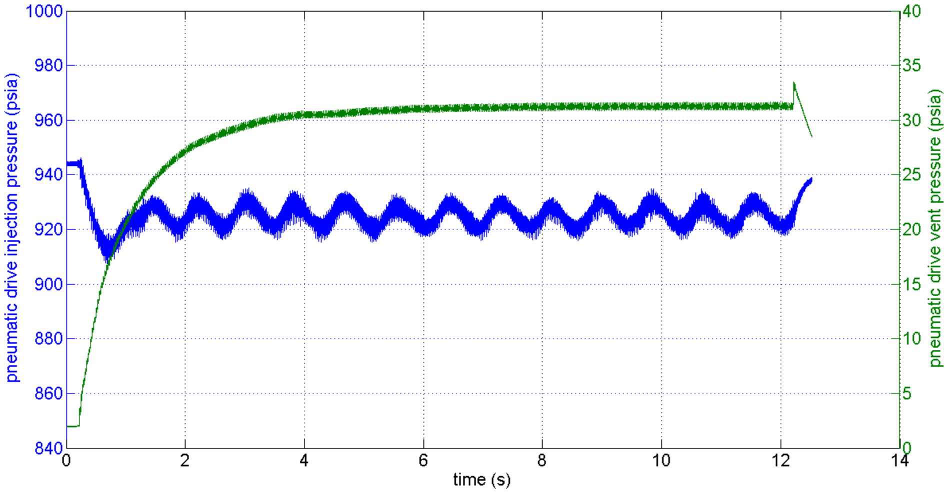

Figure 76: Pneumatic drive supply and vent pressures for second example test

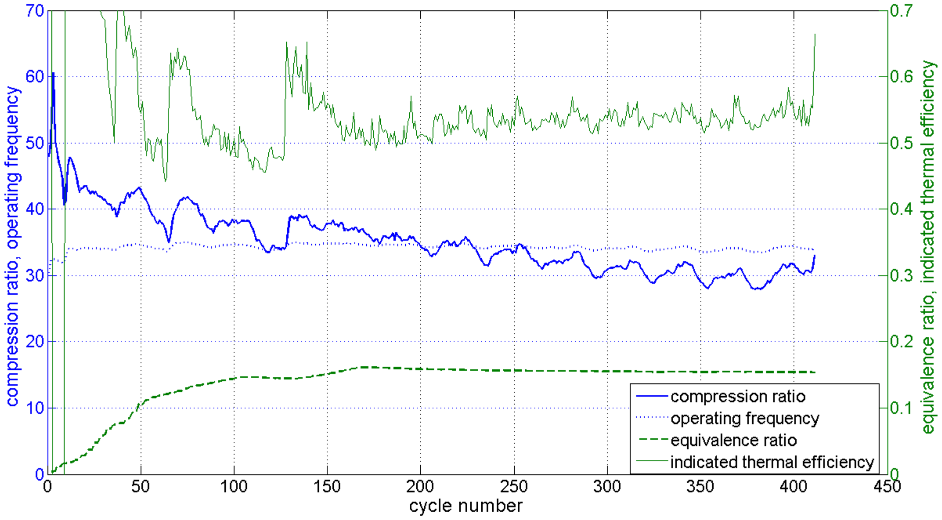

Figure 77: Compression ratio, equivalence ratio, and indicated thermal efficiency for second example test

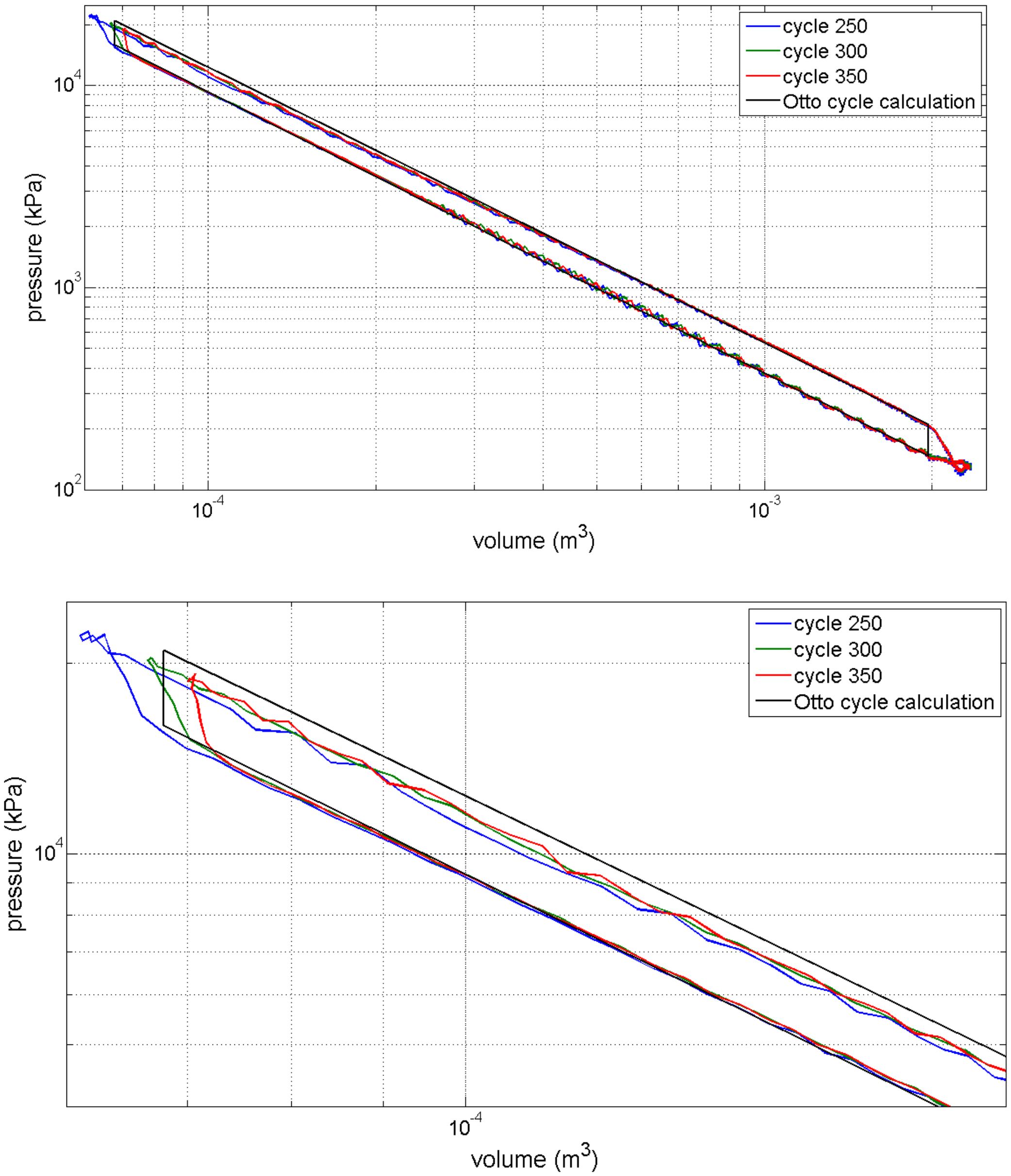

Figure 78: Combustion chamber logP-logV for several cycles of the second example test compared to an ideal Otto cycle calculation

5.3.2.2. Automatic Fuel Control

An example of data obtained with the PID feedback control is shown in Figure 79 to Figure 83. Bounce chamber pressures are shown in Figure 79. Again, a lower drive pressure is used here compared with air motoring tests. The butterfly valve is fully open in this test, so the vent pressure is similar to that of a motoring test (17-18 psia). With the lower drive pressure and consequently lower flow rate, the vent system pressure is actually a bit lower than in motoring tests. Around 15 seconds into the test, the drive pressure started dropping off as the gas supply bottles ran low.

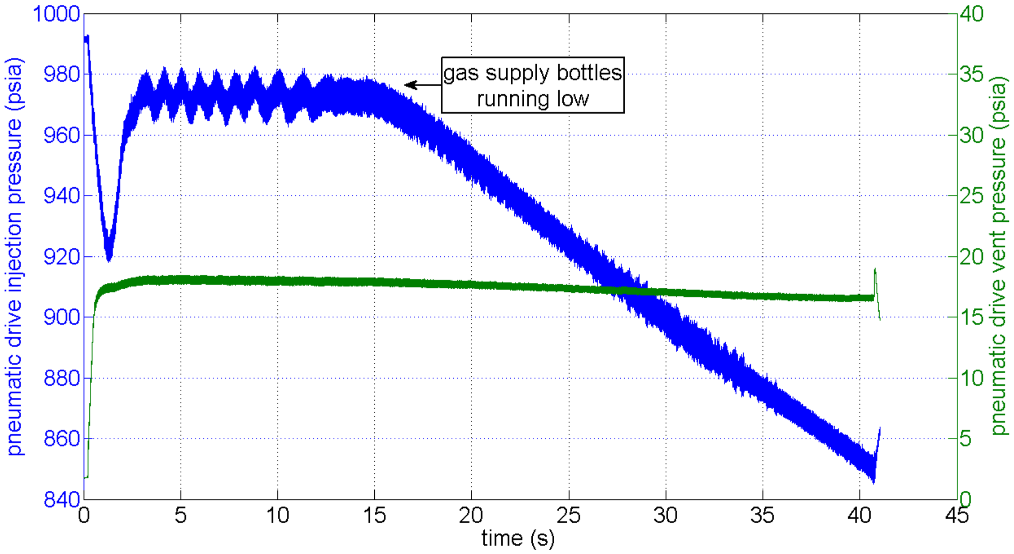

Figure 79: Pneumatic drive supply and vent pressures for automated fueling test

To make up for the reduced energy input from the bounce chambers, the controller increased the fueling rate, maintaining consistent piston travel into the bounce chambers, as shown in Figure 80. The plot shows the extent of piston travel into the bounce chamber, measured as the maximum actuation of the air injection valves. The oscillation seen in piston travel has a period of about 15 engine cycles, and could likely be removed with further controller tuning, but in a broad sense, the controller functions as intended. Compared to a test without the controller, the consistency of piston travel can be seen. Also apparent in this plot, piston 1 consistently travels farther than piston 2 in these particular tests. This behavior was not uncommon, and reflects an imbalance between the pistons, likely due to friction differences. Care was taken to balance the masses of the two piston assemblies, so this is not believed to be a factor.

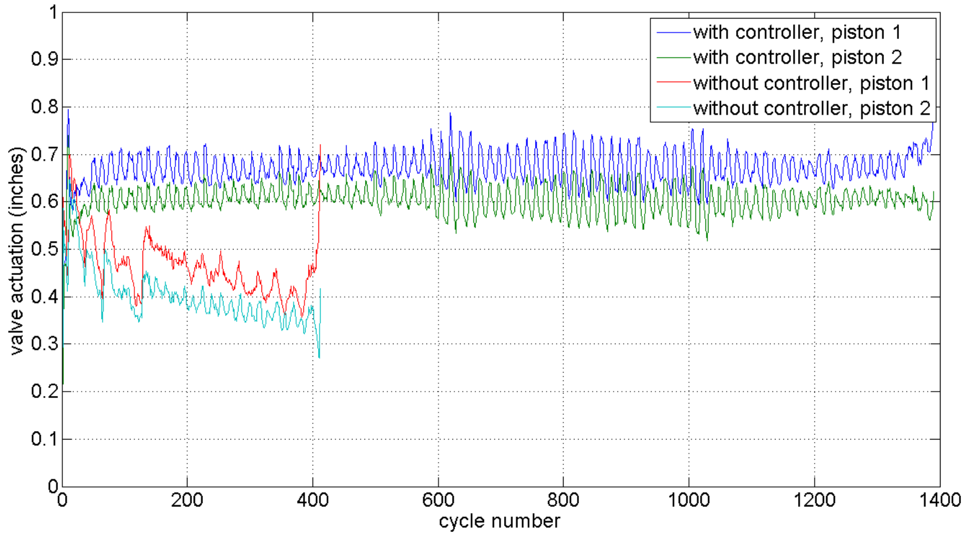

Figure 80: Comparison of the air valve actuation for automated vs. manual fuel control tests

Typical piston velocity profiles, calculated from position measurements, are shown in Figure 81, along with the cylinder pressures. Positive velocities are outward, corresponding to expansion of the combustion chamber, while negative velocities are inward. The sharp transition from negative to positive reflects the high combustion chamber peak pressure, while the more gradual transition from positive to negative reflects the wide peaks of much lower pressure seen with the bounce chamber pneumatic drive system. Closing of the air injection valves involves a mechanical impact between the valve plate and seat, which causes the glitches seen in the velocity and bounce chamber pressure curves.

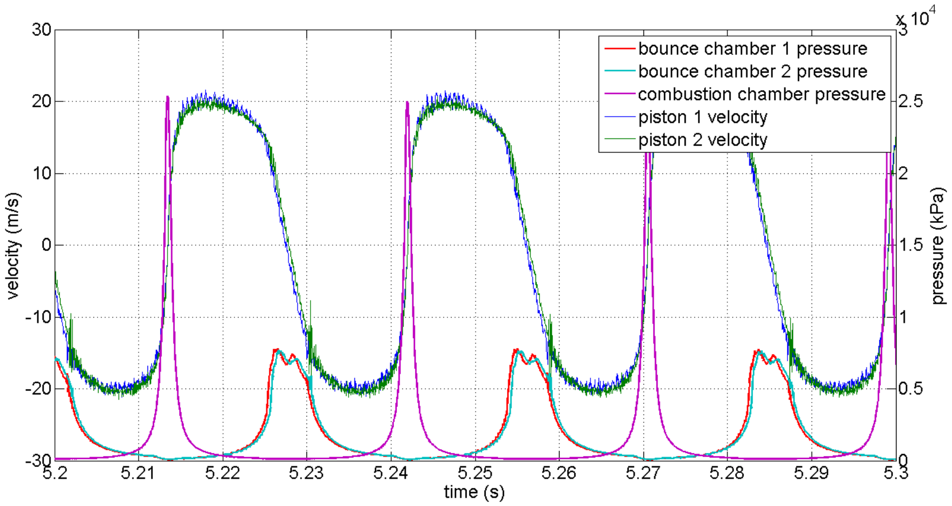

Figure 81: Typical piston velocity profiles for combustion tests

The increase in fueling rate to maintain piston travel is reflected in the equivalence ratio shown in Figure 82. Also shown in this plot, the compression ratio starts dropping off steadily around the same time. In the relatively stable period between cycles 500 and 600, the indicated work versus fuel energy input implies an average indicated thermal efficiency of 45%. Toward the end of the test, as the equivalence ratio is increased, the indicated efficiency rises. Care must be taken in interpreting these results since steady state operation was not achieved, but this is believed to be due to a relatively constant heat and gas loss becoming a smaller fraction of the energy input. This number may also be influenced by the fact that the compression ratio had dropped to a point where it was more closely matched to the autoignition point. Earlier in the test, the mixture had been compressed well beyond the point of autoignition, giving the combusted mixture more time to lose heat to the pistons and cylinder wall. Cycles from different times during the test are shown in Figure 83. Ignition occurs earlier in the compression stroke as the test progresses, which is expected as the system warms up and the fueling rate increases. In this case, the earlier cycles were overdriven even with the higher autoignition threshold.

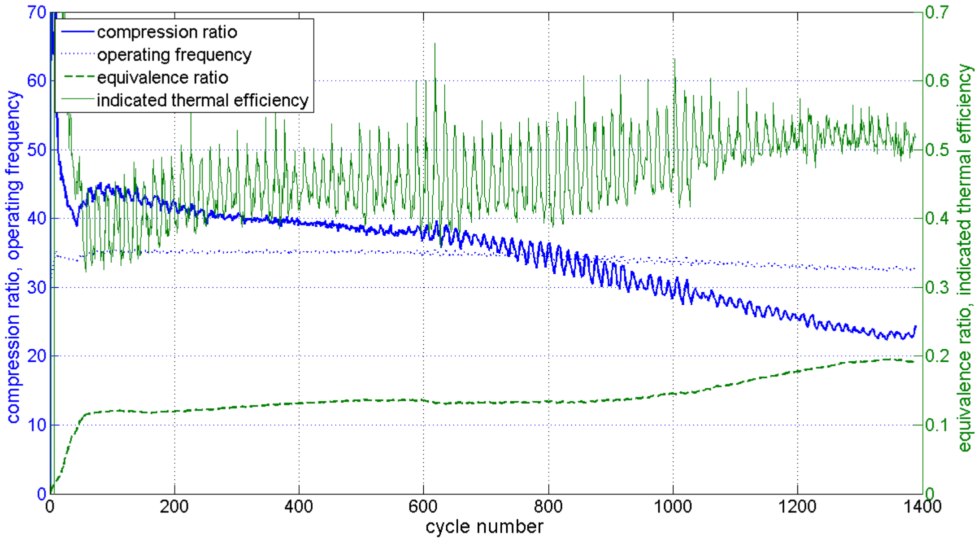

Figure 82: Compression ratio, equivalence ratio, and indicated thermal efficiency for automated fueling test

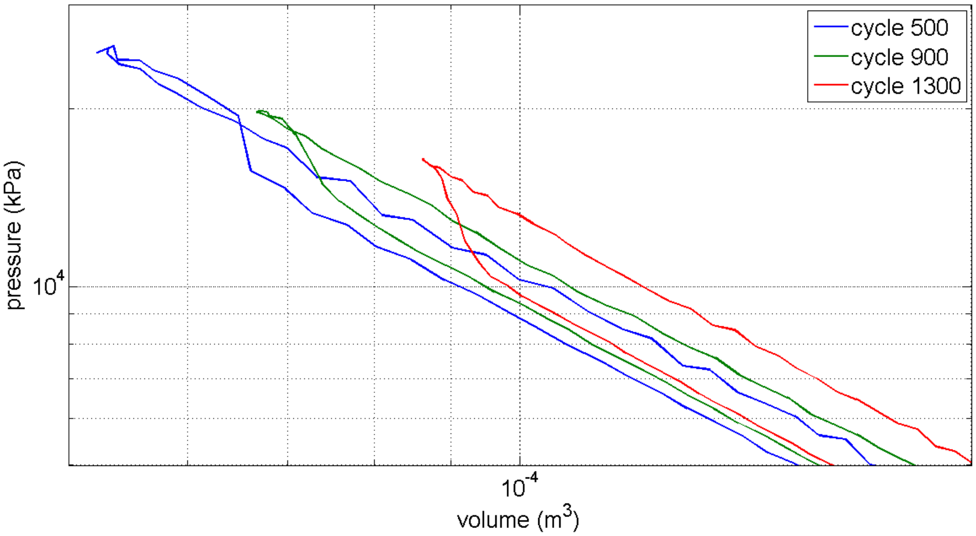

Figure 83: Combustion chamber logP-logV for several cycles of the automated fueling test

A second example of data obtained using automated fuel control is shown in Figure 84 - Figure 87. The drive system pressure was the same as shown above, but it was maintained throughout the test. The butterfly valve was set at 45% open, leading to a vent system pressure slightly above 30 psia. The resulting bounce chamber pressure-volume diagram is shown in Figure 84. In the early cycles before the vent pressure has stabilized, higher net energy input is obtained from the bounce chambers, evident in the area enclosed by the pressure-volume curves. As the pressure develops, this energy input drops and then stabilizes at around 440J total for both bounce chambers. Meanwhile, the net combustion chamber work increases before stabilizing around 820J. Note that during the air injection event, once the bounce chamber pressure has reached the drive system pressure, an approximately constant pressure is seen as gas backflows into the heads. The effect of pressure drop through the valve can be seen in the small loops created in the pressure-volume diagram.

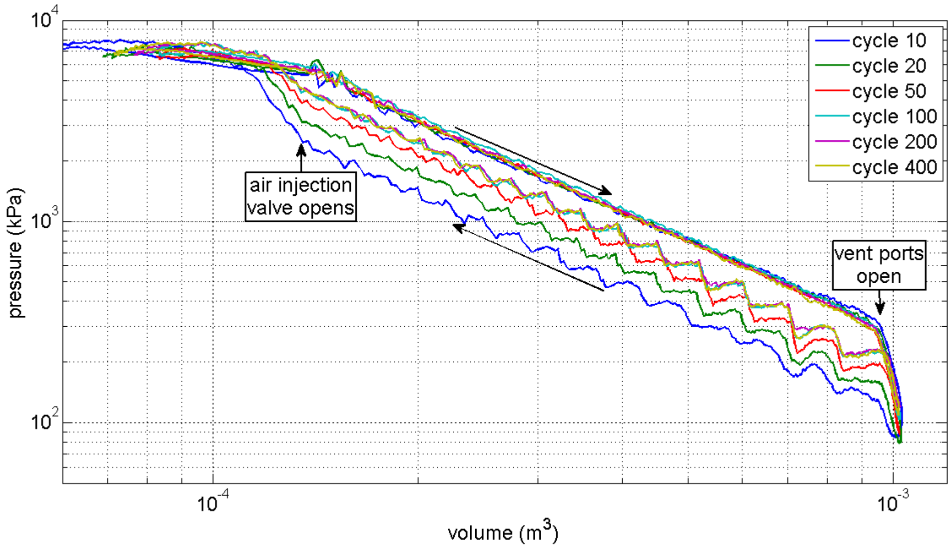

Figure 84: Bounce chamber logP-logV for the second automated fueling test

Combustion chamber pressure-volume diagrams are shown in Figure 85. Note that the earlier cycles reach a higher compression ratio before igniting due to the lower equivalence ratio and lower engine temperature. Indicated thermal efficiency around 50% was seen throughout the test, as seen in Figure 86.

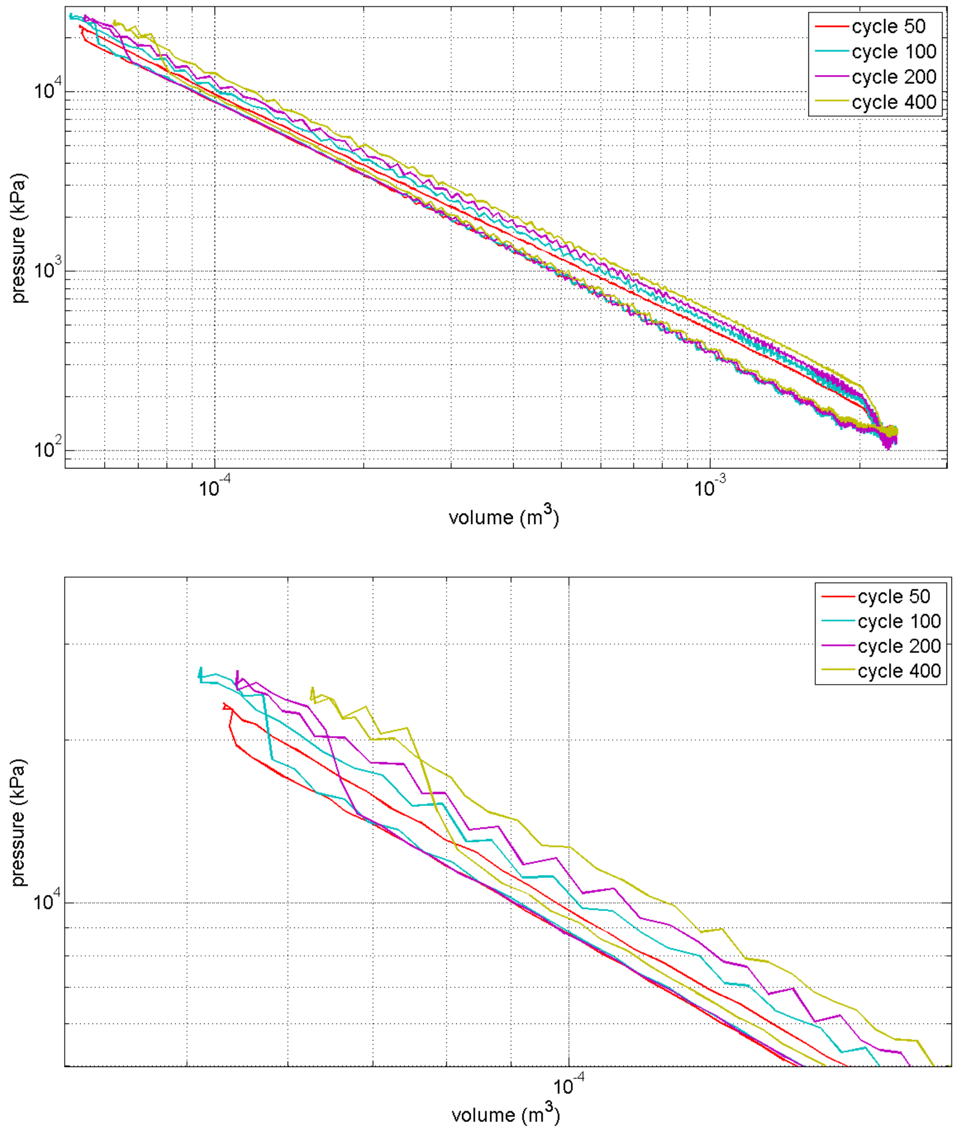

Figure 85: Combustion chamber logP-logV for several cycles of the second automated fueling test

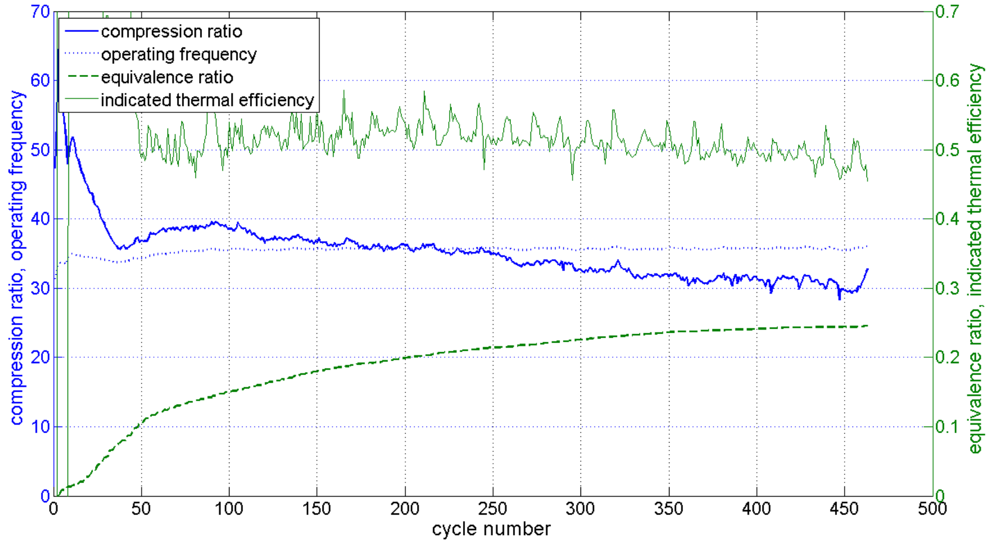

Figure 86: Compression ratio, equivalence ratio, and indicated thermal efficiency for the second automated fueling test

Ultimately, piston synchronization stopped this test from continuing. As shown in Figure 87, what had been a relatively constant piston synchronization error through the bulk of the test began to grow toward the end, triggering the engine shutdown system. This was a common occurrence during the course of testing, indicating that the passive synchronization technique, while functional, was not strong enough for the imbalances seen in this particular engine.

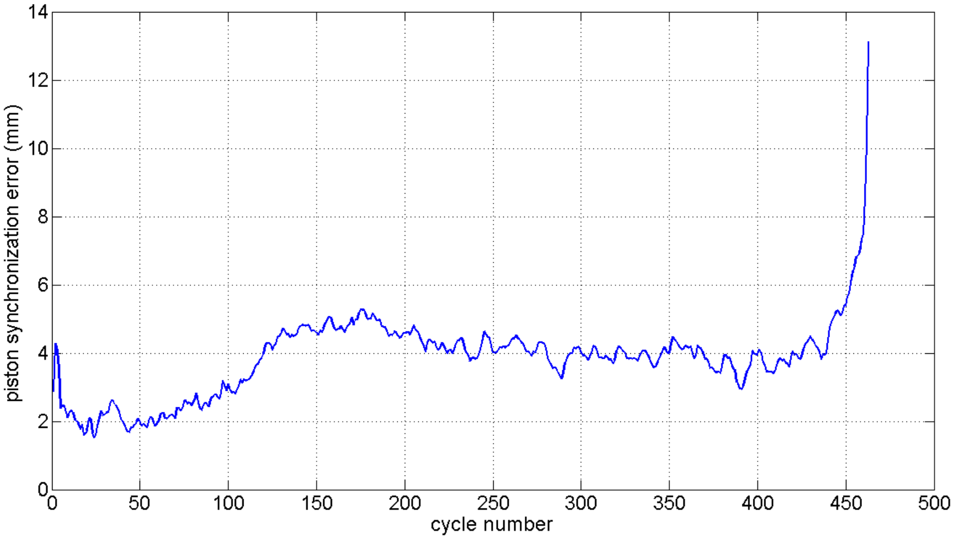

Figure 87: Piston synchronization error for the second automated fuel control test

5.3.3. Overall Combustion Performance

Over the course of combustion testing, a range of conditions and parameters were explored including fueling rate, compression ratio, and net input energy. Figure 88 shows a plot that examines the data sets as a whole. The plot shows how indicated fuel conversion efficiency (ratio of net combustion chamber energy to H_2 chemical energy) varies with fuel load. As more hydrogen is injected per cycle, the thermal and pressure losses become a smaller fraction of the combustion energy which results in a higher indicated efficiency. Note that these results do not necessarily correspond to full thermal equilibrium conditions. As the cylinder wall and piston tops warm up during each test, heat losses are expected to decrease, which could account for some of the spread in the data. Compression ratio is another factor, and is discussed below. Indicated thermal efficiency greater than 60% was measured for some cycles although this was not typical. Many tests, however, consistently reached efficiencies between 50% and 55%. Recent gasoline HCCI research has shown 47-48% gross indicated thermal efficiency for boosted intake conditions, and 42-43% for naturally aspirated conditions with 14:1 compression ratio [2]. Others have shown 56-59% gross indicated thermal efficiency at 18.7:1 compression ratio using reactivity controlled compression ignition [3]. Brake efficiencies for several modern turbocharged diesel engines compiled in [4] are in the 40-45% range, implying indicated efficiencies approaching 50%. Despite failing to reach the intended equivalence ratio of around 0.3, the indicated efficiency measurements of this study are comparable to, or slightly above, modern turbocharged diesel and boosted gasoline HCCI technology.

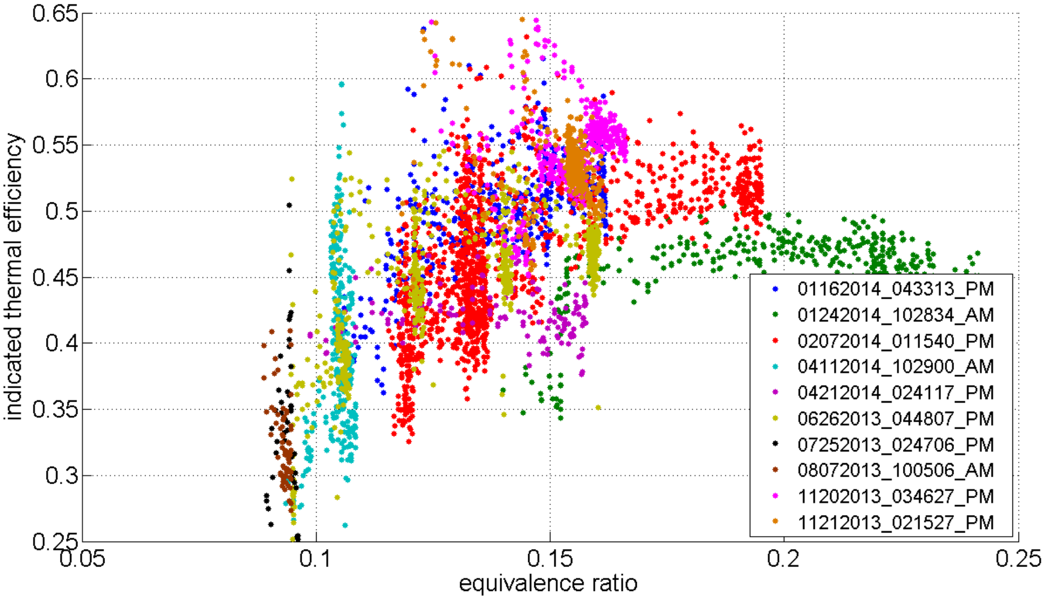

Figure 88: Indicated thermal efficiency as a function of equivalence ratio for a number of combustion tests

Figure 89 shows indicated thermal efficiency versus compression ratio. Efficiency is generally worse at the higher compression ratios. This would not be expected based on the ideal Otto cycle where efficiency increases with compression ratio. However, in a real engine crevice effects become more significant at the higher compression ratios, and thermal losses increase when compressing past the point of autoignition which was the case for many of the higher compression ratio points. Also, as previously noted, these results are not at full thermal equilibrium. In many cases, the compression ratio starts high and tapers off over the course of the test. With higher heat losses expected early in a test, this could have some influence on the results.

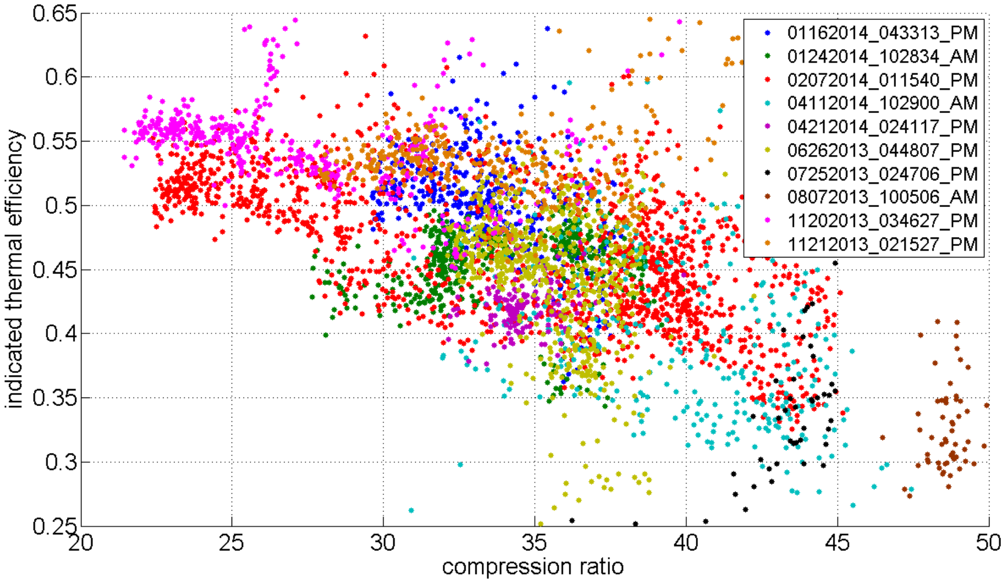

Figure 89: Indicated thermal efficiency as a function of compression ratio for a number of combustion tests

Based on the trends shown in Figure 88 and Figure 89, it would seem that even higher indicated thermal efficiency could be achieved with higher equivalence ratio coupled with a compression ratio matched to the autoignition point. For example, an equivalence ratio near 0.2 with a compression ratio near 20:1 might achieve an efficiency of 0.6 or greater. This would only be true up to the point where efficiency started to drop with lower compression ratio, but that point might be at much lower compression ratios than the low value shown in Figure 89 at about 22:1. This was the goal of a number of the final experiments with the FPLA, however it proved difficult in practice to reach this operating point before the test would end due to piston synchronization, ring failure, or some other issue.

Losses in the combustion chamber were evident during motoring experiments and prior to fuel addition during combustion experiments. Figure 90 shows the indicated work for the combustion chamber during typical motoring tests. With the piston rings in good condition, losses of 100 to 150 J per cycle were typically seen once the engine reached stable operation. As discussed in Section 5.2, this loss accounts for about 10% of the total pressure-volume energy input per cycle. Extrapolated to combustion experiments, this loss significantly reduces the potential fuel conversion efficiency.

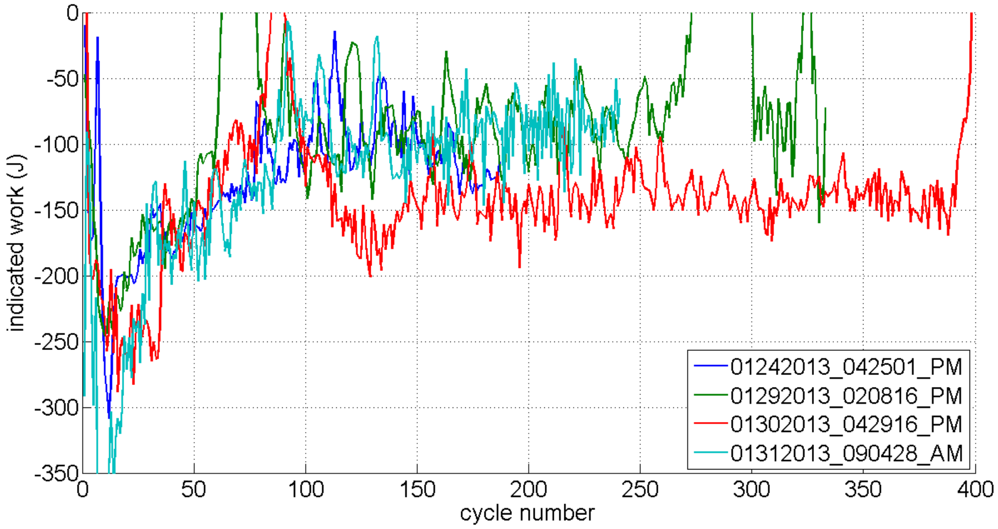

Figure 90: Negative indicated work calculated for the combustion chamber due to thermal and pressure losses

5.3.4. Alternator Performance and Overall Efficiency

The linear alternators were described in Section 2.4 as having 14 coils each with mirror image coils from each side connected in parallel to a single load resistor. An example of the instantaneous load currents for an engine cycle is shown in Figure 91. Coils are numbered 1 through 14 starting with the pair nearest to the center of the engine and moving outward. Note that only six of the 14 coils are active at any point in time. The four outermost coils on either side of the stator (1-4 and 11-14) see progressively fewer magnet poles at slower piston speed, and their contribution to the electricity generated drops off significantly, as shown in Figure 92.

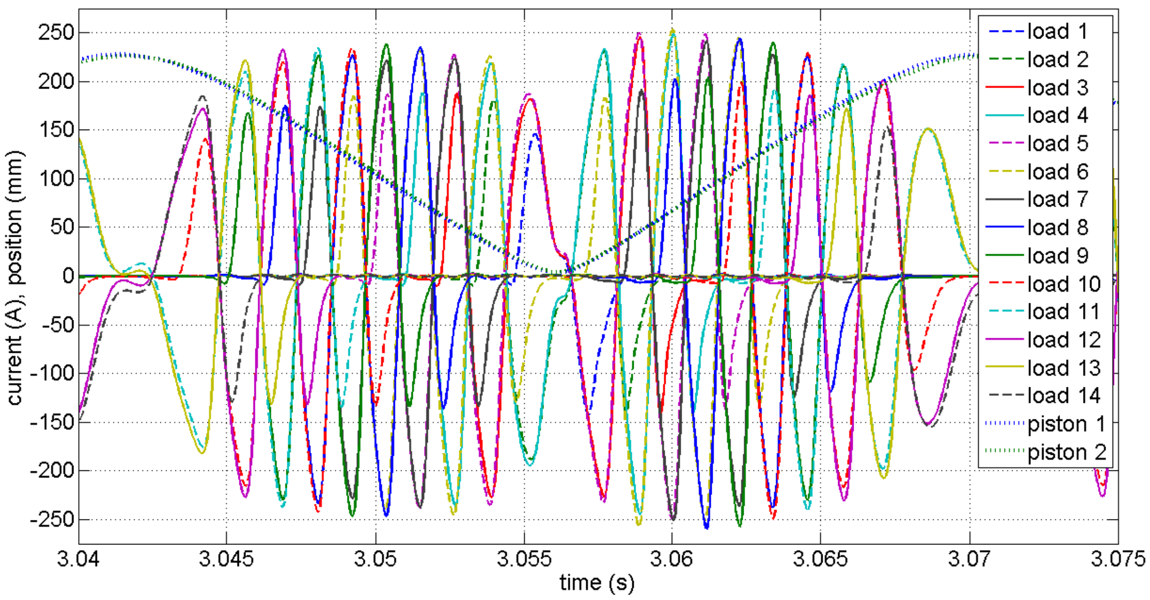

Figure 91: Example of the instantaneous load currents during one engine cycle

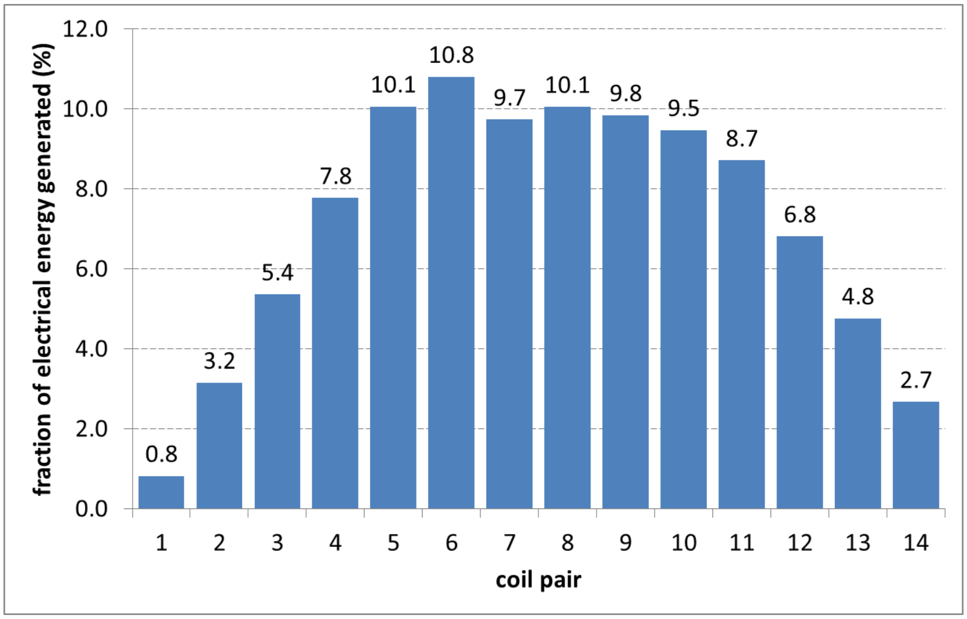

Figure 92: Contribution of each alternator coil pair to the total electrical energy

Figure 93 shows the predicted electrical energy output per cycle of the linear alternators as a function of the piston velocity using the commercial code Flux-2D. Flux-2D models the coupling between the moving permanent magnets on the piston backirons and the alternator stators. The model assumes perfect piston synchronization and a constant piston velocity through the full stroke. The model predicts a decreasing slope in energy output with increasing velocity such that above ~15 m/s, electrical energy generation per engine cycle is practically constant. Once this plateau is reached, higher piston speed will only increase power output, but not energy output. Because friction continues to increase with velocity requiring relatively more input energy, the work-to-electrical efficiency will be degraded at average speeds greater than 15 m/s.

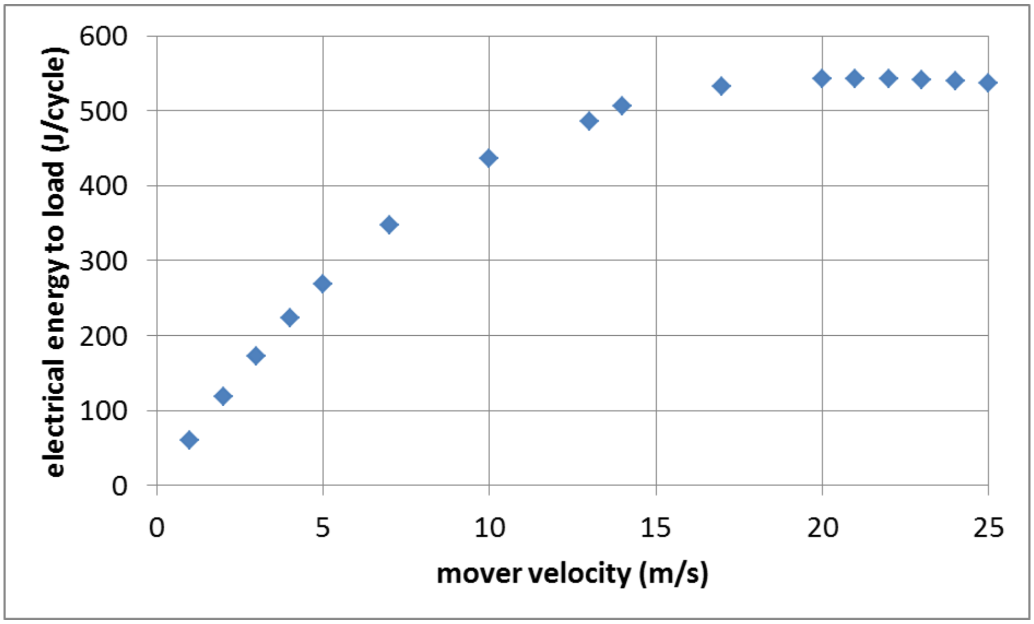

Figure 93: Flux-2D predictions of electrical energy output per cycle of the linear alternators as a function of the piston velocity

Figure 94 shows measured electrical output for several tests versus mean piston speed along with the Flux-2D results described above. Experimental results are plotted on a cycle-by-cycle basis. Electrical energy is calculated by integrating the instantaneous power measurement over each engine cycle, while mean piston speed is calculated as the distance traveled between successive BDC events divided by the time elapsed. The measured electrical output compares well with the model prediction showing a very flat slope in energy output with increasing average speed from 14 to 16 m/s. The slight offset between the measured values and the model is not unexpected since the model uses a constant speed for the full stroke, while the measurements are plotted based on average velocity. A similar plot, showing electrical power generated as a function of piston speed, is shown in Figure 95. Note that power increases much more steeply with average piston velocity. Electrical power dissipated at the load resistors was typically between 16 and 19 kW.

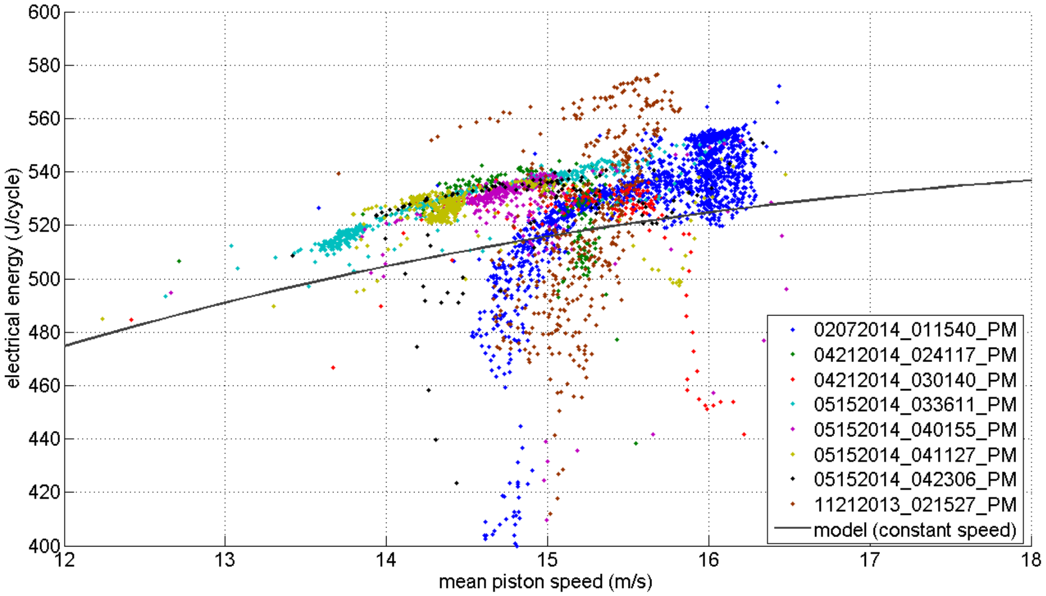

Figure 94: Measured electrical energy per cycle as a function of piston speed compared to model prediction

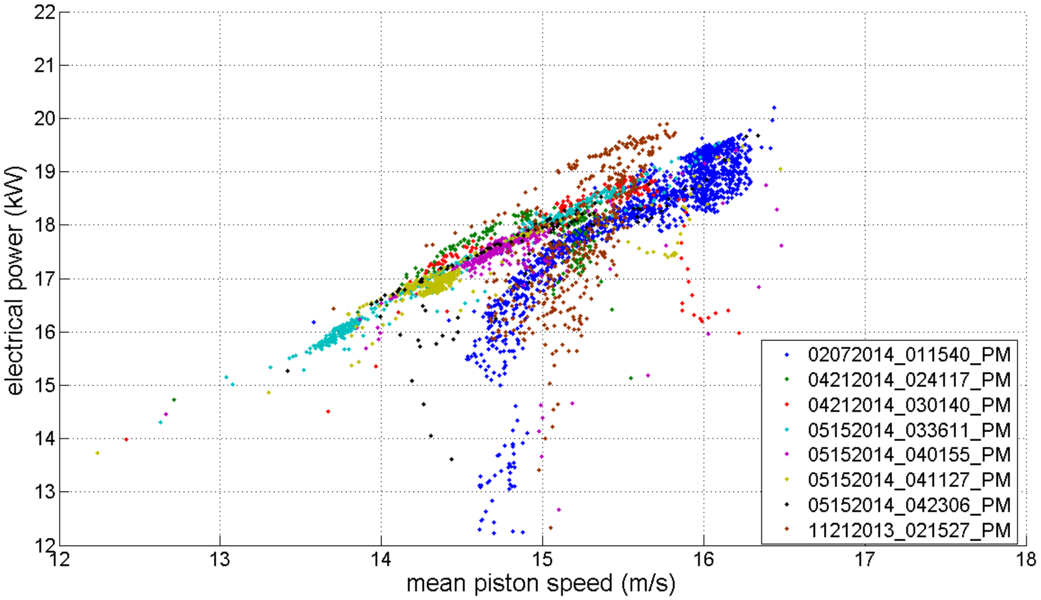

Figure 95: Measured electrical power per cycle as a function of piston speed compared to model prediction

Based on these results, the highest electrical output efficiency would be expected at average piston velocities below the 15 m/s plateau. At a nominal stroke of 220 mm that would correspond to an operating frequency of about 34 Hz. Thus, operating at a frequency higher than 34 Hz would increase energy output per cycle very little and would likely decrease electrical output efficiency.

In addition, observations of the energy required to drive the pistons at increasing speeds shows that this too seems to reach a plateau. Figure 96 shows average piston speed versus net input energy (the sum of the bounce chamber and combustion chamber energies). The figure shows that fairly large increases in input energy only result in modest, if any, increases in average piston velocity. This is likely due to a rapid increase in friction with the higher bounce chamber and combustion chamber pressures that result from the increased input energy. Thus, even if electrical energy output showed a stronger dependence on piston speed above 15 m/s, we would not see an increase in efficiency due to the much greater input energy required to drive the pistons faster.

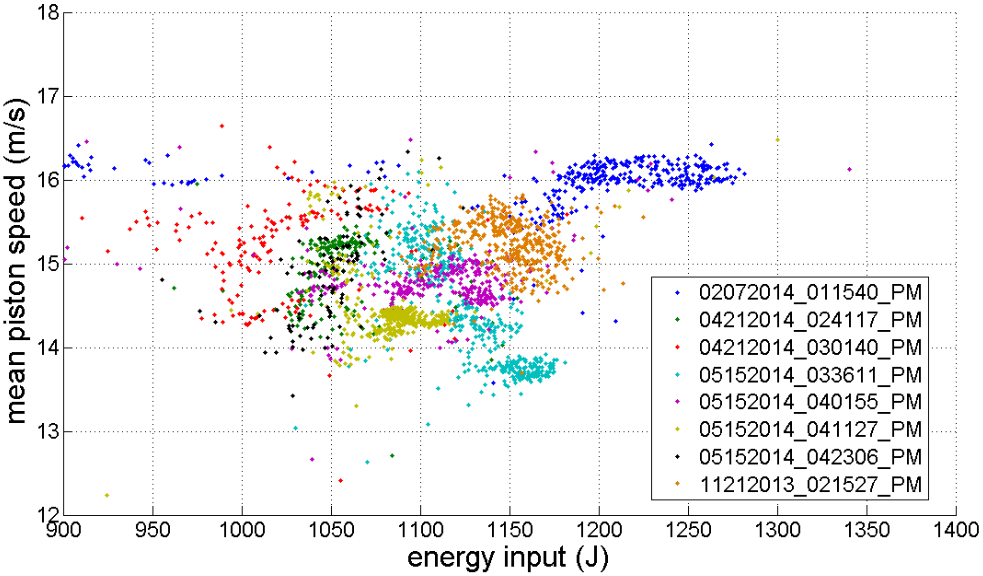

Figure 96: Average piston speed versus net input energy

The result of these two effects, the plateau in electrical energy output with piston speed and the plateau in piston speed with input energy, is reflected in Figure 97 which shows electrical output efficiency as a function of the net input energy for several tests. Work-to-electrical efficiency is the ratio of the alternator energy to the net input energy. For the test data shown, the highest efficiency shown occurs at the lowest input energy (55% at 950 J/cycle). Energy input above 950 J/cycle is primarily dissipated as friction and produces very little increase in piston speed or electrical energy.

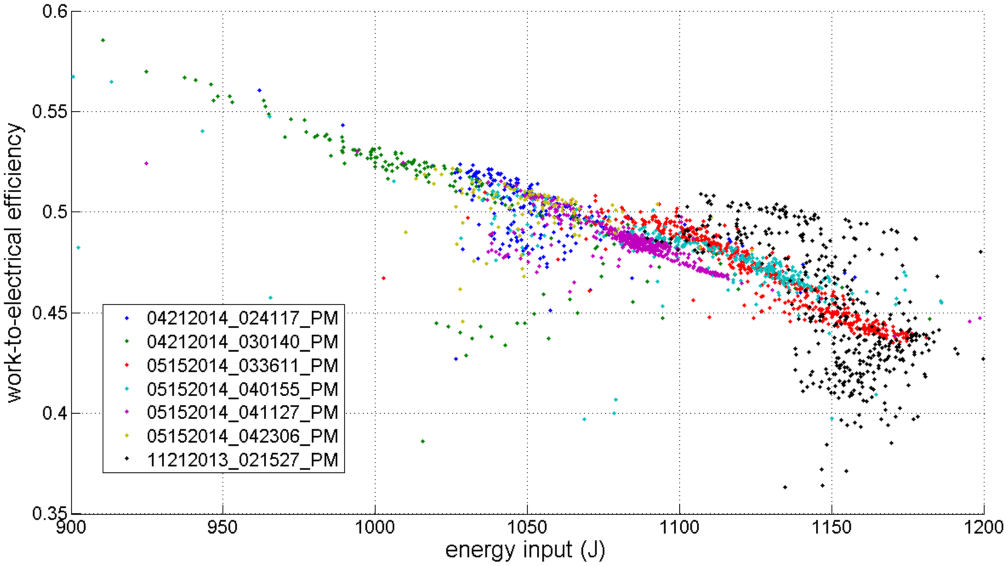

Figure 97: Electrical output efficiency as a function of the net input energy

Thus, for highest efficiency, the FPLA should be operated with input energy below 950 J/cycle. However, as with equivalence ratio and compression ratio, this was difficult to achieve in practice. Enough input energy was needed to provide both a high enough compression ratio for combustion and actuation of the annular valves for the pneumatic drive. It was difficult if not impossible to get the FPLA to achieve the piston travel required to satisfy these two constraints with less than 950 J/cycle of input energy. The system ran more consistently and for longer duration when the input energy was higher. Design modifications would be required to consistently run at lower input energy. For example, using longer actuation pins such that the annular valves were actuated earlier in the piston stroke.

When combined, the indicated thermal efficiency and the work-to-electrical efficiency give the overall efficiency of the FPLA which is the electrical energy output divided by the input fuel energy. However, the FPLA was never operated with 100% of the input energy from combustion, so this value cannot be precisely stated without some assumptions. First, let’s assume that the highest thermal efficiency seen in the data (60%) could be achieved with all of the input energy from combustion. If it is then assumed that the maximum electrical output efficiency seen in the data (~56%) is achieved simultaneously, then the overall efficiency would be 33.6%. Typical values achieved with the FPLA were lower, around 20-25%, due to difficulty in controlling operation at the ideal conditions.

5.3.4.1. Alternator Modeling

To get a better understanding of what to expect experimentally, the Sandia FPLA with Magnequench alternators was modeled with a time-dependent, *Mathematica*-based, numerical simulation code that incorporates: the Newtonian mechanics of the opposed pistons; an ideal gas law representation of the compression-combustion gas cycle; a complete circuit model from alternator induction, through current switching, to load usage; and finally passive relative piston motion stabilization. The prototype FPLA was modeled using the best-available experimental parameters and included shared power sources of gas drive transitioned to combustion, as in the experiment. When set to run at 34 Hz, it showed results similar to those of the experiment: electrical power of ~15 kW, frictional loss of ~10 kW, electrical efficiency 93.7 %, and passive stabilization of relative piston motion that is highly sensitive to differences in friction on the two pistons. This theory-to-model comparison shows no significant surprises and indicates that while passive stabilization does work, the unforeseen large frictional losses do interfere with its efficacy.

This prototype experiment was developed to focus on FPLA operation using a basic resistive load for the test, without going to the expense of developing a corresponding hybrid vehicle-specific charging system. It must be recognized that the switching circuitry needed to optimally charge a battery and support a DC load would present a different impedance to the FPLA than the resistive load used here, and correspondingly it would alter the FPLA performance.

Specifically, when an alternator coil drives a resistive load, the driving EMF is induced by permanent magnets passing through the coil. This voltage is then offset by the back EMF of the current flowing through the resistive load and the internal resistance of the alternator coils themselves. Hence, power is transferred from the moving magnets to the resistive parts of the circuit. Additionally, the time-changing current induces a back EMF in the coils that must also be offset by the moving alternator magnets. The back EMF due to the self-inductance of the coils lags the resistive EMF by 90° in phase. The product of this self-induced voltage in the coils with the coil current creates what is known as reactive power. Although with the 90° phase shift it contributes no net power to the load, reactive power phase shifts the load current away from the phase of the driving voltage, reducing the amount of real power that can be taken from the alternator. Reactive power places a cap on the real power that can be drawn from a given alternator at a specific frequency. A simple analytic model with constant-velocity pistons predicts the maximum attainable power of this machine at 34 Hz to be ~16 kW, far below the design power of 30 kW for the Magnequench alternator. The cause of this limitation is the reactive power.

Putting a capacitor in series with each load resistance can mitigate the effects of reactive power, similar to the way a capacitor is switched into electric motor circuits for power conditioning during startup. The capacitor shifts the phase of reactive power forward, opposite to the self-inductance of the coils. This was modeled for the prototype using the simulations code described above. If a rotary machine is running at a constant electrical frequency of ω (radians/s), then the product of the coil inductance, L, with the capacitance, C, should be $LC = \omega^{-2}$ to achieve the needed resonance. The electrical frequency of an FPLA varies greatly during a single stroke, so the average electrical frequency for an engine running at 34 Hz, 2136 (radians/s), was used to choose a capacitance of 2.66 mF. When this capacitance was modeled in series with each coil-load circuit, the output power for the FPLA was increased to 30 kW. It was correspondingly necessary to reduce the load resistance per circuit to 70% of the 0.182 Ω in the prototype and increase the gas feed and fuel input in the model. The increased power capability of the engine would raise the current in the coils, reducing the electrical efficiency to 91.2 % in this case.

In an actual FPLA application, one would expect to connect all of the coil pairs into a single load circuit rather than have 14 separate loads. This has been modeled for the Magnequench alternator using the same code as before. When it is assumed that all 14 coils are connected in series, there can be a single load with just one power conditioning capacitor. The two coils in each coil pair are connected in parallel, then that pair is in series with the next pair etc. This simplifies the power conditioning and loading, but it routes all of the current through all of the coils simultaneously. That means all of the coils are carrying current at once, while only 5 or 6 are actively driving current. The net effect is to reduce the electrical efficiency to ~75%, an unacceptably low value. Connecting a low-resistance AC switch across each coil pair, then bypassing that pair when it is not actively producing power can mitigate this reduced efficiency. Such compensation could bring the electrical efficiency back up to ~90%.

An electrical efficiency of ~90% is not as good as one would like to see for a machine like this. If the prototype could be run at its original design frequency of 44 Hz, modeling predicts that it would be ~97.5% electrically efficient, a good value. Unfortunately, the unforeseen high friction in the existing machine keeps it from operating with sufficient mechanical efficiency at that frequency. If one expected to run this type of alternator at the lower frequency, the efficiency issue could be mitigated by designing more conductor into each alternator coil.

The outcome from this relatively optimized model has useful predictive value. Power conditioning with capacitors does work in the model and allows the design power of 30 kW to be achieved. This reduces some of the reactive power effects that help keep the experimentally observed prototype power in the range of 16 to 19 kW. The reason for the discrepancy between the peak power of 15 to 16 kW seen in both the simple and advanced models versus the 16 to 19 kW measured in the experiment remain unclear.

Regarding stability, if the Magnequench model is up to speed, running only on combustion and at the significantly lower friction originally anticipated, it will typically run passively stable for thousands of cycles. One can watch as the pistons drift slightly out of phase and are pulled back together in a regular sinusoidal motion, as intended. Of course, if the frictional loading is sufficiently imbalanced, synchrony is lost. One can only conclude that passive stabilization is not a viable option without a very well balanced engine operating at lower friction than seen in the present prototype.

Early on in the Sandia FPLA effort a different linear alternator was designed by the Sandia team and modeled with a modified version of the advanced code discussed above. That was a single-mover concept with combustion chambers at each end. There were 25 coils, and the mover had three sets of permanent magnets on it. The end magnets spanned two coils each and the central magnet covered four. The magnetic flux coupling to each coil is far more complex than the nearly sinusoidal function of mover position seen in the Magnequench model. A flux function table was created using the Flux-2D code and input to *Mathematica* for the simulation modeling. This model also included a computer-controlled switching circuit to simulate the charging of a Saft battery pack. Since there was only one mover, there was no stability issue as before; however, it was necessary to include a governor in the model to keep the running frequency stably constant. Since the waveforms on the different coils are not easily correlated, it was necessary to have a separate switching circuit for each coil to connect into the load, as in the more efficient versions of the Magnequench system. When the Sandia alternator model was run at 44 Hz to send 30 kW to the load, its electrical efficiency was typically 95 to 96%.

In conclusion, the simulation effort covered a wide range of models from simple time-averaged electrodynamics to advanced system-wide numerical integrations of coupled component equations. The advanced two-mover model predicted passive stabilization of the synchronized movers, as was seen to a limited degree in the experiment. Both models gave lower power predictions than the values measured in the experiment. Both models also clearly emphasize the importance of compensating for reactive power in the Magnaquench alternator if one were to strive to get the design power of 30 kW from the machine.

5.3.5. Exhaust Gas Analysis

NOx emissions measurements were made in these early tests (second set of automatic fueling tests discussed in Section 5.3.2) to get initial data, though engine run time was not long enough to obtain steady readings due to the sample plumbing delay. A peak reading of 9 ppm was obtained in this test. Oxygen analyzer results using the same sample pump lend some credibility to this initial reading. The equivalence ratio calculated based on exhaust oxygen content peaked at 0.24, while the equivalence ratio calculated from fuel and air flow rates reached 0.25. An illustration of this is shown in Figure 98. Here, the exhaust oxygen is calculated from measured air and hydrogen flow rates assuming complete combustion. The calculations also assume that water is removed to saturation at 5°C based on specifications of the sample gas conditioner. Sample plumbing and analyzer response time cause a delay of 20 to 25 seconds in the exhaust gas measurements. Here, the calculated oxygen has been shifted in time to line up with the measurement. The measured and calculated oxygen reach nearly the same minimum value, indicating that a representative exhaust sample did reach the analyzers during the test, and that the injected fuel was almost fully trapped and converted.

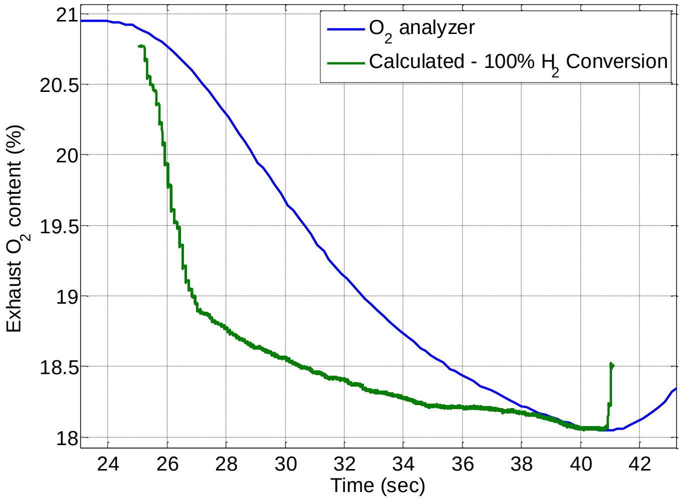

Figure 98: Comparison of O2 content in exhaust gas between O2 analyzer and calculation based on 100% conversion efficiency

6. CONCLUSIONS AND RECOMMENDATIONS

6.1. Conclusions

A prototype free piston engine – linear alternator system has been developed at Sandia National Laboratories. The opposed piston design was developed to investigate its potential for use in hybrid electric vehicles. The twin, dual-ended pistons were driven from a central combustion chamber while bounce chambers were used as a means of energy storage to provide compression work for the next cycle. The opposed piston configuration eliminates the problem of momentum balance and vibration that a single piston design would cause in a vehicle application. The system is mechanically simple with two-stroke uniflow scavenging for gas exchange and timed port fuel injection for fuel delivery, i.e. no complex valving. Electrical power was extracted from piston motion through linear alternators which also provided a means for passive piston synchronization through electromagnetic coupling.

For the purpose of laboratory evaluation a pneumatic drive system was implemented to start and maintain piston motion while transitioning to combustion. This system proved challenging to implement in practice. Gas flow and pressure requirements for motoring were higher than anticipated requiring the design and installation of the high pressure nitrogen system as well as modifications to many of the pneumatic drive and vent system components. These modifications included the piping to the bounce chamber heads, the heads themselves, numerous valve plate designs, spring and spring retainers, and vent manifolds and tubing. Starting the piston motion pneumatically worked tenuously and was unreliable. This also required the addition of the vacuum system on the vent manifolds. Due to this difficulty, a combustion based start was developed.

Passive synchronization of the pistons was successfully demonstrated through continuous motoring tests. However, robust operation was limited by the somewhat weak restoring force of the passive synchronization. Ultimately, synchronization limited the duration of the tests that could be run with the FPLA system to less than a minute. A design more perfectly balanced between the two sides in terms of friction, electromagnetic, and pressure forces would be needed for passive synchronization to be viable. This could perhaps be achieved, but it is likely that active control through the linear alternators would be a more robust solution and one that has been demonstrated by other groups.

Durability was an issue for several aspects of the proof-of-concept design. The piston rings used for this project were not meant for a commercial system, but were also insufficient for the experimental evaluation. Ring wear and damage occurred too quickly to get consistent results and replacing the rings was tedious and time consuming. Magnet damage was another issue. Some of the damage was certainly due to off-normal events such as piston over-travel. However, some damage was suspected to have been due to the rapid acceleration and deceleration of the pistons. Durability of the valve plates was improved to the point that it didn’t interfere with testing, but occasional repair or replacement was needed. However, this may be of little importance since a commercial system would not use a pneumatic drive system.

Low equivalence ratio HCCI combustion with hydrogen was successfully demonstrated. Hydrogen/air mixtures with phi = 0.04 to 0.25 were compression ignited with compression ratios ranging from 20:1 up to 70:1. Indicated thermal efficiencies between 50% and 55% were common and some results were higher. However, it proved difficult to control engine parameters to achieve optimized combinations of phi and compression ratio to achieve high thermal efficiency and high power output given the short test durations. A few extended duration (~30 sec.) combustion tests have shown a path to greater than 55% indicated thermal efficiency through higher equivalence ratio coupled with a compression ratio that produces autoignition at TDC.

Work-to-electrical efficiency was determined based on the electrical energy output of the linear alternators. This energy was found to be limited by two related effects. The first effect is a saturation of the electrical energy output as a function of piston speed. This effect was predicted by a Flux-2D model of the coupling between the moving permanent magnets on the piston backirons and the alternator stators. The model predicted a decreasing slope in energy output with increasing velocity such that above an average piston speed of about 15 m/s, electrical energy generation per engine cycle is practically constant. This prediction was confirmed by measurements of electrical output and piston velocity. Based on these results, the highest electrical output efficiency would be expected at average piston velocities below the 15 m/s plateau. At a nominal stroke of 220 mm that would correspond to an operating frequency of about 34 Hz. Thus, operating at a frequency higher than 34 Hz does not increase energy output per cycle and decreases electrical output efficiency.

The second effect, found experimentally, was that above a certain average piston speed, fairly large increases in input energy only result in modest, if any, speed increases. This is likely due to a rapid increase in friction with the higher bounce chamber and combustion chamber pressures that result from the increased input energy.

The result of these two effects, the plateau in electrical energy output with piston speed and the plateau in piston speed with input energy, is that the highest work-to-electrical efficiency seen in the data occurs at the lowest input energy (55% at 950 J/cycle). Energy input above 950 J/cycle is primarily dissipated as friction and produces very little increase in piston speed or electrical energy. Operating at lower than 950 J/cycle would likely result in greater than 55% efficiency, but this operating point was not achieved in practice.

Although the FPLA was never operated with 100% of the input energy from combustion, a value for total efficiency can be calculated if it is assumed that the highest thermal efficiency seen in the data (60%) could be achieved with all of the input energy from combustion. If it is then assumed that the maximum electrical output efficiency seen in the data (~56%) is achieved simultaneously, then the overall efficiency would be 33.6%. Typical values achieved with the FPLA were lower, around 20-25%, due to difficulty in controlling operation at the ideal conditions.

Typical power output measured from the alternators was 16 to 19 kW, far below the design power of 30 kW for the Magnequench alternator. A simple analytic model with constant-velocity pistons provides an explanation for this discrepancy. The reactive power with a simple resistive load limits the power output. Putting a capacitor in series with each load resistance can mitigate the effects of reactive power, similar to the way a capacitor is switched into electric motor circuits for power conditioning during startup. When an appropriate capacitance was modeled in series with each coil-load circuit, the output power for the FPLA was able to be increased to 30 kW by reducing the load resistance and increasing the input power in the model. However, the increased power raises the current in the coils, reducing the electrical efficiency to 91.2 % in this case. Additionally, if the prototype could be run at its original design frequency of 44 Hz, modeling predicts that it would be ~97.5% electrically efficient, a good value. Unfortunately, higher than expected friction prevents the current FPLA from achieving that speed. At 34 Hz, the efficiency issue could be mitigated by designing more conducting material into each alternator coil.

6.2. Recommendations

Based on the conclusion discussed in the previous section, several recommendations can be made for future development of the FPLA system. Firstly, to enable longer runtime and more robust operation, start-up and active control through the linear alternators should be implemented. This might be possible without redesigning the alternators, but just reconfiguring the coil connections such that a three-phase system is achieved. Power electronics would then be needed to drive the alternators as motors for start-up. An active control algorithm would be required to switch from generator to motor to maintain piston synchronization.

A second recommendation would be a detailed friction analysis and new ring design. The bronze impregnated Teflon rings used during this project were not robust enough to enable longer duration operation of the engine. In addition, frictional energy dissipation significantly reduced the overall efficiency of the FPLA system. A low friction, high durability ring design should be a priority for future development.

Damage to the permanent magnets was an issue for the current system. Future designs should prevent the magnets from contacting any surface during normal operation and abnormal events. In addition, a study should be carried out.to understand whether inertial forces due to high G-loads cause fatigue failures in the magnets. If so, a new magnet array design would be required.

In order to achieve higher overall efficiency, the FPLA system must run at the optimum operating point. For the current system, this means running at a lower speed than 34 Hz with less than 950 J/cycle input energy. Design modifications informed by modeling would be needed to enable this operating point.

For emissions measurements, longer runtimes are needed. Active control and new ring designs should enable much more consistent and robust operation that leads to extended test durations.

7. REFERENCES

1. Goldsborough, S. and Van Blarigan, P., "Optimizing the Scavenging System for a Two-Stroke Cycle, Free Piston Engine for High Efficiency and Low Emissions: A Computational Approach," SAE Technical Paper 2003-01-0001, 2003, doi:10.4271/2003-01-0001.
2. Dec, J., Yang, Y. and Dronniou, N., "Improving Efficiency and Using E10 for Higher Loads in Boosted HCCI Engines," SAE Int. J. Engines 5(3):2012, doi:10.4271/2012-01-1107.
3. Splitter, D., Wissink, D., DelVescovo, D., and Reitz, R., "RCCI Engine Operation Towards 60% Thermal Efficiency," SAE Technical Paper 2013-01-0279, 2013, doi: 10.4271/2013-01-0279.
4. Miller, S., Svrcek, M., Teh, K-Y., and Edwards, C., "Assessing the feasibility of increasing engine efficiency through extreme compression," Int. J. Engine Research, 2011, 12, 293-307, doi: 10.1177/1468087411404299.
5. Das, L. M., "Hydrogen Engines: A View of the Past and a Look Into the Future," Int. J. Hydrogen Energy, vol. 15, no. 6, pp. 425-443
6. Van Blarigan, P. and Green, R., "NOx Emission Data Verified in a Hydrogen Fueled Engine," CRF News, vol. 17, no. 4, Jan/Feb 1995.
7. Onishi, S., Jo, S. H., Shoda, K., Jo, P. D. and Kato, S., "Active Thermo-Atmospheric Combustion (ATAC) – A New Combustion Process for Internal Combustion Engines," SAE Technical Paper 570032, 1979.
8. Karim, G. A., and Watson, H. C., "Experimental and Computational Considerations of the Compression Ignition of Homogeneous Fuel-Oxidant Mixtures," SAE Technical Paper 710133, 1971.
9. Christensen, M., Johansson, B., and Einewall, P., "Homogeneous Charge Compression Ignition (HCCI) Using Isooctane, Ethanol and Natural Gas - A Comparison with Spark Ignition Operation," SAE Technical Paper 972874, 1997, doi:10.4271/972874.
10. Christensen, M., Johansson, B., Amnéus, P., and Mauss, F., "Supercharged Homogeneous Charge Compression Ignition," SAE Technical Paper 980787, 1998, doi:10.4271/980787.
11. Braun, A. and Schweitzer, P., "The Braun Linear Engine," SAE Technical Paper 730185, 1973, doi:10.4271/730185.
12. Mikalsen, R. and Roskilly, A. P., "A review of free-piston engine history and applications," Applied Thermal Engineering, 27 (2007), pp. 2339-2352
13. Hanipah, M. R., Mikalsen, R., and Roskilly, A. P., "Recent commercial free-piston engine developments for automotive applications," Applied Thermal Engineering, 75 (2015), pp. 493-503.
14. Kosaka, H., Akita, T., Moriya, K., Goto, S. et al., "Development of Free Piston Engine Linear Generator System Part 1 - Investigation of Fundamental Characteristics," SAE Technical Paper 2014-01-1203, 2014, doi:10.4271/2014-01-1203.
15. Goto, S., Moriya, K., Kosaka, H., Akita, T. et al., "Development of Free Piston Engine Linear Generator System Part 2 - Investigation of Control System for Generator," SAE Technical Paper 2014-01-1193, 2014, doi:10.4271/2014-01-1193.
16. Schneider, S., Rinderknecht, F., and Friedrich, H. E., "Design of Future Concepts and Variants of the Free Piston Linear Generator," Ninth International Conference on Ecological Vehicles and Renewable Energies, Monaco, 2014.

17. Haag, J., Kock, F., Chiodi, M., Mack, O. et al., "Development Approach for the Investigation of Homogeneous Charge Compression Ignition in a Free-Piston Engine," SAE Technical Paper 2013-24-0047, 2013, doi:10.4271/2013-24-0047.
18. Kock, F., Haag, J., and Friedrich, H., "The Free Piston Linear Generator - Development of an Innovative, Compact, Highly Efficient Range-Extender Module," SAE Technical Paper 2013-01-1727, 2013, doi:10.4271/2013-01-1727.
19. Van Blarigan, P., Paradiso, N., and Goldsborough, S., "Homogeneous Charge Compression Ignition with a Free Piston: A New Approach to Ideal Otto Cycle Performance," SAE Technical Paper 982484, 1998, doi:10.4271/982484.
20. Goldsborough, S. and Van Blarigan, P., "A Numerical Study of a Free Piston IC Engine Operating on Homogeneous Charge Compression Ignition Combustion," SAE Technical Paper 1999-01-0619, 1999, doi:10.4271/1999-01-0619.
21. Goldsborough, S. and Van Blarigan, P., "Optimizing the Scavenging System for a Two-Stroke Cycle, Free Piston Engine for High Efficiency and Low Emissions: A Computational Approach," SAE Technical Paper 2003-01-0001, 2003, doi:10.4271/2003-01-0001.
22. Aichlmayr, H. T., Van Blarigan, P., "MODELING AND EXPERIMENTAL CHARACTERIZATION OF A PERMANENT MAGNET LINEAR ALTERNATOR FOR FREE-PISTON ENGINE APPLICATIONS," Proceedings of the ASME 3rd International Conference on Energy Sustainability, 2009, San Francisco, CA.
23. Shah, T., "Fuel Injector Flow Testing: Free Piston Linear Alternator," Sandia National Laboratories memorandum to Terry Johnson, July 6, 2012.

APPENDIX A: KEY FPLA DIMENSIONS

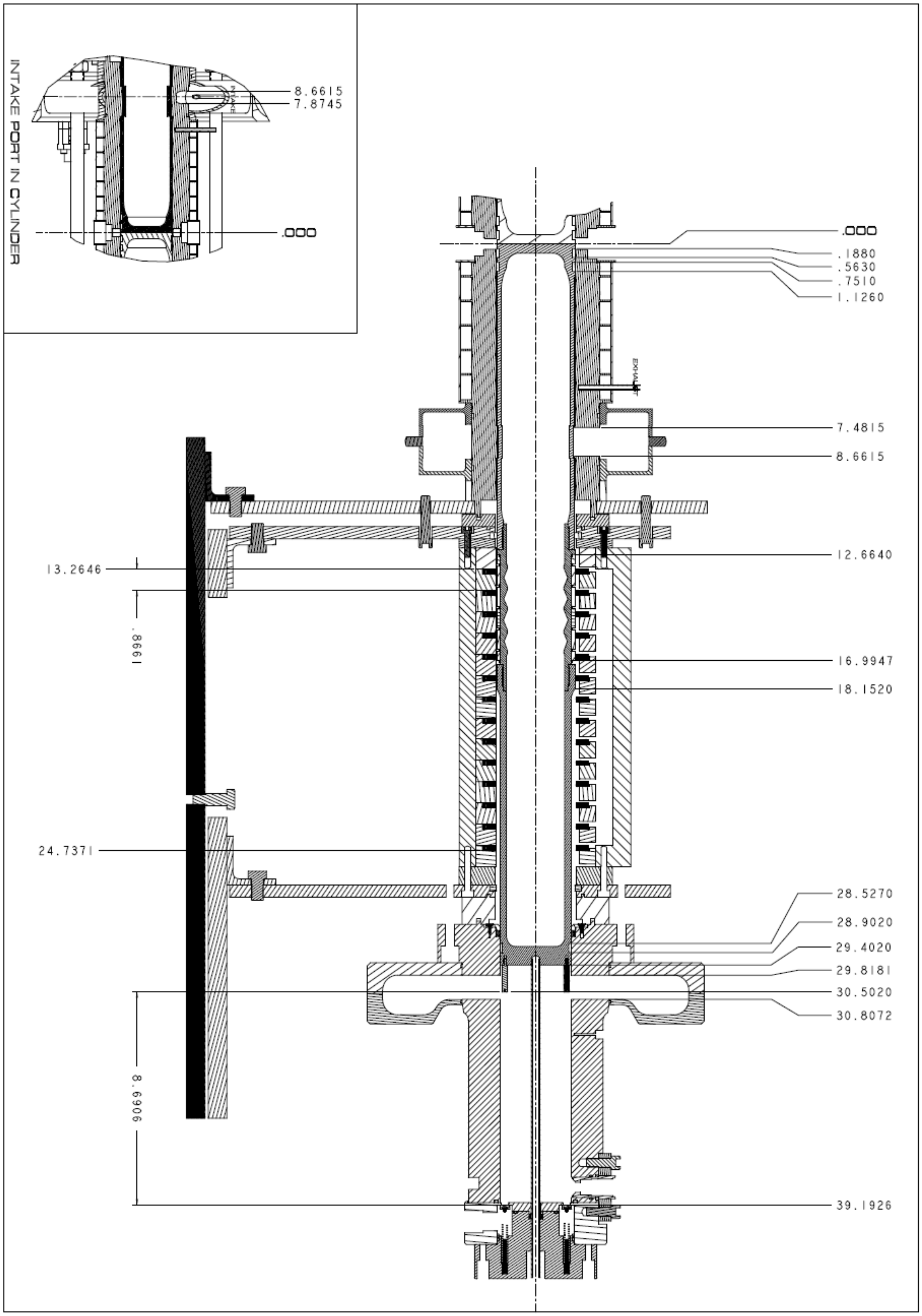

DISTRIBUTION

1	MS0899	Technical Library	9536 (electronic copy)

Sandia National Laboratories